

Exploring the applications of dissipative coupling in microwave frequencies

by

Yutong Zhao

A Thesis submitted to the Faculty of Graduate Studies of
The University of Manitoba
in partial fulfillment of the requirements of the degree of

MASTER OF SCIENCE

Department of Physics and Astronomy

University of Manitoba

Winnipeg

Copyright ©2020 by Yutong Zhao

Abstract

The discovery of dissipative coupling leads to level attraction. It opens a new avenue to study light-matter interaction, enabling novel applications in quantum information and spintronics technologies based on its exotic features. The polaritons raised from spin-photon hybridization display coherence for the exchange of energy. The coherent and dissipative coupling between two resonances have been modeled by two oscillators with different coupling components, with different behaviors in eigenspace. We briefly introduced numerical methods to obtain the field distribution of resonant modes from Maxwell's equations and the time-domain analysis on the coherent and dissipative coupled system. These numerical results help us to enhance our understanding from another perspective and may benefit the future cavity magnonics research in the nonlinear regime. The level attraction is demonstrated on a planar structure by using a cross-shaped microstrip resonator and split-ring resonators. The dissipatively coupled metamaterial has been achieved by compensating the electric and magnetic coupling. Furthermore, the zero dampings in the hybridized system have been proven to be singularities. This system preserves an infinity quality factor and a sharp transition from rigorous zero to unity transmission, which displays promising applications on sensing and switch devices. Based on previous research, the interference between the coherent and dissipative coupling displays a giant nonreciprocity in cavity magnonics. Since the bandwidth of nonreciprocity is limited by the magnon, there remains a challenge of designing broadband nonreciprocal devices for practical applications. By locally control the radiation of magnon, an effective broadband nonreciprocity has been demonstrated with a few hundreds of times of magnon bandwidth. This thesis work improves the understanding of coherent and dissipative coupled systems. Moreover, it explores the approaches to implementing dissipative coupling for practical applications in quantum information technologies and cavity spintronics.

Acknowledgements

First, I would like to thank my supervisor Dr. Can-Ming Hu, for the guidance he provided me throughout my Master's studies. His attitude towards academic research moves me and motivates thinking. His insight, intuition, and pursuit of excellence are admirable and worth learning. I appreciate the direction he pointed out. I also want to express my appreciation to Dr. Yongsheng Gui, who has offered a great time, effort, and patience during my Master's study. Together we have achieved a lot of research programs without whose guidance I would never have the opportunity to finish these kinds of tasks.

Dynamic Spintronics Group members together created a very friendly, fast-paced, and optimistic environment. It is my luck to have these colleagues during my Master's program, with whom I had the opportunity to discuss new ideas and learning from each other. In particular, I have to thank Jinwei Rao, who has taught me most of the experimental and computer simulation skills in the past four years. His idea and the courage to overcome experimental difficulties always inspire me to try something new. However, life is sometimes like a journey. Although you escort a good friend thousands of miles, yet the time to say good-bye must come at last. Here, I hope this brother-like friend will have great expectations. Another person I would like to give a special thank is Ying Yang as a team member, who has accompanied me for two years and four months at the time of writing this thesis. During this time, and I learned a lot from her, such as focus, rigorous, meticulous, and, most importantly, the attitude towards academic research. In a sense, these personalities will influence me for the rest of my life. Science research is a long journey in which not all travelers can end up with academic careers. However, by applying the science philosophy and method definitely will benefit the next adventure in a new field.

Finally, I would like to express a special thanks to my family and family-to-be, my mother Liwei Liu, my father Haidong Zhao, and my girlfriend Ying Yang, who support me with their love and encouragement. Especially, my father, as a mechanical engineer, fabricated the critical components for the first level attraction experiment in cavity magnonics. In this research his contribution shall

never be forgotten. I always respect this selfless, positive, motivated unsung hero from the bottom of my heart, and it is a great fortune to be his son. My mother always shares her life experience and treated me not only as her son but also as a friend in a respectful environment, which is exceptionally meritorious among traditional Chinese parents. My significant other and I bravely pictured the future, which gives me the courage to face the forthcoming new-stage life. Also, thank the beautiful memory and the sweet smiles she left for me. This section has limited space and cannot express all my gratitude. I wish they all deserve happiness and longevity.

“It is strange that only extraordinary men make the discoveries, which later appear so easy and simple.”

Georg C. Lichtenberg

Contents

Abstract	ii
Acknowledgements	iii
Table of Contents	viii
List of Figures	xvi
1 Introduction	1
1.1 Magnon-Photon Hybridization and Polaritons	1
1.2 Discovery of dissipatively coupled cavity-magnon-polaritons	3
1.3 Thesis Outline	5
2 Theoretical Background	7
2.1 Lagrangian formalism of coupled systems	7
2.1.1 Coherent coupled pendulums	8
2.1.2 Dissipative coupled pendulums	12
2.2 Numerical methods in cavity magnonics	15
2.2.1 Field Simulation using finite element analysis	15
2.2.2 Time domain analysis using an ODE solver	18
3 Dissipatively coupled metamaterials for sensitive detection	25
3.1 Background	25
3.2 Theoretical model	27

3.2.1	General formula of a coupled <i>RLC</i> circuit	27
3.2.2	Resonance frequency and zero-damping condition in a coupled <i>RLC</i> circuit .	31
3.2.3	Complex analysis on transmission	35
3.3	Experiment results	39
3.3.1	Ultra-narrow-band microwave invisibility	40
3.3.2	Observation of level attraction	42
3.3.3	Control of the Zero damping condition	44
3.3.4	Voltage controlled level attraction	45
3.4	Summary	47
4	Dissipatively coupled magnon-photon system for broadband nonreciprocal devices	48
4.1	Introduction	48
4.2	Theory	49
4.2.1	Effective Hamiltonian of our cavity magnonic device	49
4.2.2	Transmission spectrum of dissipative magnonic device	51
4.2.3	Reflection spectrum measured from the loop antenna	53
4.2.4	The classical microwave circuit model for dissipative coupling	54
4.3	Experiment	56
4.3.1	Locally control of the magnon damping by inducing a loop antenna	57
4.3.2	Enhancement of effective bandwidth	60
4.4	Summary	61
5	Conclusion	62
A	Mathematics of dissipatively coupled system	65
A.1	Transmission coefficient derivation for dissipatively coupled system	65
A.2	Zero damping conditions (ZDCs) and its simplification	67

B Numerical results on microwave resonators	70
B.1 Excitations of split-ring resonators	70
Bibliography	73

List of Figures

2.1 The coherent coupled pendulums system. (a) The schematic of the mechanical system connected by a spring. The oscillator in red (left) represent the cavity mode resonance, and the blue (right) is the magnon mode resonance. We assume the effective mass of each mode are same. (b) The real part of the eigenvalues (resonant frequencies) of the hybridization as a function of detuning gives the dispersion relation. (c) The imaginary part of hybridized eigenvalues (damping rates) exchange with each other due to coupling effect. The evolution of normalized eigenvector characterize a out-of-phase oscillation for higher frequency mode (d) and in-phase oscillation for lower frequency mode (e). All calculation is based on parameters $\omega_1/2\pi = 1$ GHz, $\lambda_1/2\pi = 9$ MHz, $\omega_2/2\pi \sim 0.5 - 1.5$ GHz, $\lambda_2/2\pi = 1$ MHz and coherent coupling strength as $\kappa/2\pi = 50$ MHz	9
2.2 The dissipatively coupled pendulums system. (a) The schematic of the mechanical system connected by a dashpot. (b) The real part of the eigenvalues (resonant frequencies) of the hybridization as a function of detuning gives the dispersion relation. (c) The imaginary part of hybridized eigenvalues (damping rates) repels each other due to coupling effect. The evolution of normalized eigenvectors characterize a out-of-phase oscillation for cavity-like mode (c) and in-phase oscillation for magnon-like mode (d). All calculation is based on parameters $\omega_1/2\pi = 1$ GHz, $\lambda_1/2\pi = 9$ MHz, $\omega_2/2\pi \sim 0.5 - 1.5$ GHz, $\lambda_2/2\pi = 1$ MHz and coherent coupling strength as $\kappa/2\pi = 50$ MHz	13

2.3 Examples of finite element analysis of microstrip line structures by using CST microwave studio software. (a) The mesh view of the cross cavity with a length of 60 mm with the ports setup shown on the graph. The microwave input was excreted on port 1 and the frequency was set to 3.08 GHz to match the resonance. (b) Simulated magnetic field distribution of the cavity. (c) Simulated electric field distribution of the cavity. (d) The mesh view of a split-ring resonator excited by a microstrip transmission line. he microwave input was excreted on port 1 and the frequency was set to 1.97 GHz to match the resonance. (e) Simulated magnetic field distribution of split-ring resonator. (f) Simulated electric field distribution of split-ring resonator. All the field distribution shows the maximum absolute value on plane 1 mm above the microstrip.	17
2.4 The simulated scattering parameters of the system shown in Fig.2.3 (a) with amplitude (a) and phase (b).	18
2.5 (a) At zero detuning, the Rabi-oscillation of system showing the photon resonator in red and magnon resonator in blue as a function of time. (b) The eigenvalues of the coherently coupled systems which preserve the anticrossing behavior. (c) Envelop as a function of time at various detunings with the cavity in red curve and magnon in blue. (d) The time-domain mapping of cavity resonator with detuning as and Y-axis and time as X-axis. The amplitude of the oscillation as the color-axis. (e) The time-domain mapping of magnon resonator. The colormap is on a linear scale. (f) The frequency spectrum acquired from the time-domain signal by using Fast Fourier Transformation. (g) Frequency spectrum mapping for oscillator 2 by FFT. (h) Frequency spectrum mapping for oscillator 1 by FFT. The parameters we used for calculation are given by $\omega_1/2\pi = 10$ Hz, $\omega_2/2\pi = 10$ Hz, $\lambda_1/2\pi = 0.01$ Hz, $\lambda_2/2\pi = 0.01$ Hz and coupling strength $J/2\pi = 0.1$ Hz.	23

2.6 (a) The synchronization-like oscillation in which photon resonator in red and magnon resonator in blue as a function of time at $\Delta = 0$. (b) The eigenvalues of the dissipatively coupled systems. (c) Envelop as a function of time at various detuning with the cavity in red curve and magnon in blue. (d) The time-domain mapping of the cavity with detuning as and Y-axis and time as X-axis. The amplitude of the oscillation as the color-axis. (e) The time-domain mapping of magnon. The colormap is on a linear scale. (f) The frequency spectrum acquired from the time-domain signal by using Fast Fourier Transformation. (g) Frequency spectrum mapping for oscillator 2 by FFT. (h) Frequency spectrum mapping for oscillator 1 by FFT. The parameters we used for calculation are given by $\omega_1/2\pi = 10$ Hz, $\omega_2/2\pi = 10$ Hz, $\lambda_1/2\pi = 0.01$ Hz, $\lambda_2/2\pi = 0.01$ Hz and coupling strength $\Gamma/2\pi = 0.1$ Hz.	24
3.1 Equivalent RLC-circuit for coherent coupling.	29
3.2 Schematic of two coupled resonator in a two-port system, which is side-coupled with a transmission line.	32
3.3 The real and imaginary contributions of the complex frequencies ω_{\pm} of the hybridized modes, calculated as a function of ω_2 according to Eq. (3.9) showing distinguished hybridization and linewidth evolution signatures for (a, b) $J/2\pi=0.07$ GHz and $\Gamma=0$, (c, d) $J=0$ and $\Gamma/2\pi=0.07$ GHz, and (e, f) $J/2\pi = \Gamma/2\pi=0.03$ GHz, respectively. Here we use $\omega_1/2\pi=2.5$ GHz, $\gamma_1/2\pi=0.01$ GHz and $(\gamma_2 + \kappa_2)/2\pi=0.02$ GHz. The vertical and diagonal dotted lines in (a,c,e) indicate the uncoupled dispersions for two <i>RLC</i> oscillators respectively. The vertical dotted lines in (d,f) correspond to zero damping rate and the arrows indicate the zero damping condition.	33
3.4 Calculated transmission amplitude (a) and phase (b) and The I/Q diagrams (c) for positive damping (in green curves), zero damping (in red curves) and negative damping (in blue curves). Parameters we used are $\omega_1 = 2$ GHz, $\gamma = 0, \pm 50$ MHz, and $\kappa = 0.99$ GHz.	35

3.5 The I-Q analysis for coherent coupling. (a) The calculated level repulsion dispersion. (b) The calculated linewidth exchange evolution. (c) Waterfall plot of $ S_{21} $ amplitude in dB scale as a function of detuning. (d) Waterfall plot of S_{21} phase in radian. Shifts have been applied to different spectrums for clarification. (e) The I/Q diagrams under various detunings. The parameter we used for calculation is $\omega_1 = 2$ GHz, $\kappa_1 = 0.99$ GHz, $\gamma_1 = 10$ MHz, $\omega_2 = 1 \sim$ GHz, $\kappa_2 = 0$ MHz, $\gamma_2 = 6.5$ MHz, $J = 60$ MHz and $\Gamma = 0$ MHz.	37
3.6 The I-Q analysis for dissipative coupling. (a) The calculated level repulsion disper- sion. (b) The calculated linewidth exchange evolution. (c) Waterfall plot of $ S_{21} $ amplitude in dB scale under various detunings. (d) Waterfall plot of S_{21} phase in radian. Shifts have been applied to different spectrums for clarification. (e) The I/Q diagrams under various detunings. The parameter we used for calculation is $\omega_1 = 2$ GHz, $\kappa_1 = 0.99$ GHz, $\gamma_1 = 10$ MHz, $\omega_2 = 1.3$ GHz, $\kappa_2 = 3.6$ MHz, $\gamma_2 = 6.5$ MHz, $J = 0$ MHz and $\Gamma = \sqrt{\kappa_1 \kappa_2} = 60$ MHz.	39
3.7 (a) Measured S_{21} spectrum (circles) of the bare cross-cavity and the line shape calcu- lation (solid lines). (b) Measured S_{21} spectrum (circles) of an SRR with a radius of 8.5 mm excited through a standard 50Ω transmission line and the line shape calcula- tion (solid lines). (c) Schematic picture of the coupled metamaterial structure, where a split-ring resonator (SRR) is strongly coupled with the cross-cavity. The arms in x direction of the cavity have been shorted to ground. (d) S_{21} spectrum of the coupled system by placing the SRR (face-up) on the top of the cavity as schematically shown in (b). Circles are the experimental data, and the solid line is the calculation using Eq. (3.8).	40

3.8 (a) Waterfall plot of S_{21} spectra of the coupled metamaterial structure with different SRR radius. Green circles and solid red lines represent the measured and fitted results using Eq. (3.8), respectively. (b) plots the frequencies of the hybridized modes as a function of ω_2 , where blue and purple circles represent the SRR-like and cavity-like hybrid modes. The solid line is the calculated real part of $\tilde{\omega}_\pm$ with an effective coupling constant $G/2\pi = 76i$ MHz for simplicity. (c) The deduced coupling constant J and Γ as a function of ω_2	42
3.9 (a) Schematic diagram of the experimental set-up. The separation, d , between the planes of the SRR and cross-cavity was continuously tuned from 1.5 to 4.5 mm. (b) Three typical S_{21} spectra measured at $d = 1.5$, $d = 1.8$ mm and $d = 4.0$ mm. (c) The deduced coupling constant J and Γ as a function of d . (d) The deduced linewidth of the SRR-like mode as a function of the dimensionless quantity Γ/Δ . Dotted line indicates the linewidth of the uncoupled SRR.	44
3.10 (a) The design of a frequency tunable SRR by integrating a varactor biased by a dc voltage. Two RF chokers were used to isolate the microwave signal. (b) The microwave transmission mapping for the tunable SRR excited by a standard 50Ω transmission line. The white dashed line represents the frequency of the uncoupled cross-cavity mode, $\omega/2\pi = 2.25$ GHz. (c) Experimental S_{21} spectra mapping as a function of ω and ω_2 . Black dashed lines are the calculated dispersion using the complex coupling constant $G/2\pi = 69i$ MHz. (d) The linewidth of the cavity-like hybridized mode is plotted as a function of ω_2 . The solid red line indicates the calculation result. Dotted line indicates the linewidth of the bare cavity.	46

4.1	(a) Schematic diagram of the interactions between a magnon mode and a cavity mode. A loop antenna is placed close to the magnon mode to control its radiation damping. (b) Schematic picture of our device. A YIG sphere is placed on the intersection of the cross cavity. The separation distance D between it and the loop antenna is tunable. (c) Comparison of the forward and backward transmission spectra ($ S_{21} $ and $ S_{12} $) measured at the side ZDC. Black dashed line indicates the measured transmission spectrum of the empty cavity, which is shifted by -10 dB for the sake of clarity.	52
4.2	The schematic of classical circuit model.	55
4.3	(a) Three reflection spectra measured from the loop antenna at the separations of 0.58, 1.3 and 5.5 mm. Reflection spectra measured at 1.3 and 5 mm have been downwards shifted by 0.2 and 0.4, respectively. The solid black line is the calculation result by using Eq. (4.8). (b) Damping rates of the magnon mode fitted from (a), which exhibits an inverse square dependence on the separation (D). The solid black line is a D^{-2} curve to guide the eyes.	57

B.1 (a) Three different way to excite a SRR with electric coupling (*i*) and magnetic coupling (*ii*) to magnetic resonance and electric coupling (*iii*) to electric resonance by different setup of plane wave. (b) The response of the SRR as a function of frequency of excitation signal. (c) Maximum electric and magnetic field distribution of the magnetic and electric resonance. (d) Analog of the magnetic resonance with a magnetic dipole and electric resonance with electric dipole. The light blue arrows represent the induced current and the black arrow penetrate the paper represent the magnetic field.

Chapter 1

Introduction

1.1 Magnon-Photon Hybridization and Polaritons

The hybridization between collectively excited spin waves and cavity microwave photons was firstly predicted in 2010 [1] which was motivated by the coherent transfer of quantum information between two systems. By placing a magnetic resonance material such as ferromagnetic materials close to a microwave cavity, the energy will flow back-and-forth through photon-magnon interaction and therefore forms a coupling effect. The strong interactions between the spin waves and photons generate a kind of quasi-particle, which is named as cavity-magnon-polariton (CMP). This polariton preserves the spin-photon duality, which offers a new field to study light-matter interaction. CMP has now been developed to a branch of spintronics, a field of studying the solid-state based spin-dependent electron transportation device. Spintronics differs from the electronics by inducing electron spin as an additional degree of freedom has shown a positive effect on data storage and transfer [2] which may benefit quantum computing [3]. The development of spintronics since the 1980s [4] has emerged many useful subfields with practical applications. Superconducting spintronics combines spintronics and superconductivity can enhance the central effects of magnetoresistance [5]. Graphene spintronics displayed a promising future on making spin transistors and spin logic devices [6]. Cavity spintronics [7] that studies the spintronics in photon cavities, especially CMP, for example, can manipulate spin current over a long distance [8]. The advantage of CMP is that

the system can be flexible tuned in multiple degree of freedoms, and preserve long coherence time [1, 9–14]. Spin-photon hybridized systems can also serve as a host of other exotic phenomena such as slow light [15], quantum memory [13], and exceptional point [16].

The coherent coupling in CMP was firstly achieved at low temperature by placing a Yttrium-Iron-Garnet sample in a planar superconducting resonator [10]. The strong coupling of CMP mode that displays avoided crossing dispersion was firstly observed with high cooperativity. This motivates the following explorations, and soon after, the CMP systems were realized at room temperature in closed microwave cavities [12]. Besides the strong coupling regime in the CMP system, the damping effect plays an important role. For example, the Purcell regime enhances the decay of the microwave cavity photon when the magnon damping becomes dominant. Also, the electromagnetic-induced-transparency (EIT) regime has a transparency window passing the board cavity spectrum if the cavity decay is significant. The anticrossing dispersion becomes blurry in Purcell and EIT regimes providing various possible applications. These research that explore practical applications carry CMP studies forward, leads the recent upsurge discoveries in the past six years, and generates many practical applications. For example, remote control of the spin current that not limited by spin diffusion length [8], characterizing the complex permittivity and permeability of nanoparticles [17], and designing a Hall-like logical device [18].

From an experimental perspective, high spin density and low-loss ferromagnetic materials, such as yttrium-iron-garnet (YIG), are commonly proposed for cavity spintronic research and devices to achieve a relatively high cooperativity in the spin-photon coupling. Moreover, high-quality microwave cavities with extremely low losses are always desirable for many practical reasons, which include filters that remove a single mode from the continuous electromagnetic spectrum and hence provide a clean environment needed for experiments [19]. Classically, coherently coupling mechanisms can be interpreted as the field overlapping [12] and results in the energy exchange between two oscillators. In the quantum picture, the polaritons are generated as the quantized spin waves interact with second quantized electromagnetic waves [20]. Since both theories can describe the CMP systems, it can also serve as an experiment object to explore the boundary between classical

and quantum effects.

The development of CMP studies has been expanding to the metamaterials area, in which the magnon has been replaced by a split-ring-resonator (SRR) [21] as the metamaterial analog. In general, metamaterials are engineered structures that have exotic behavior than naturally occurred materials that usually involve magnetic resonance. This so-called pseudo magnon utilizes the magnetic resonance mode [22] of SRRs and produce an effective magnetic dipole through induced current without magnetic materials. The SRR can be excited by both electric and magnetic coupling [23] and does not require a bias magnetic field which can miniaturize the spintronic cavity devices. The magnetic response of the SRRs can be used to achieve the negative permittivity and permeability in various frequency ranges [24, 25]. Metamaterials bring a great advantage to design on-chip microwave components. For instance, voltage-controlled electromagnetic induced transparency has been demonstrated, allowing the propagation of microwave photon to be manipulated on-chip [26]. The electric and magnetic coupling within meta-structures has been discussed in the proposed stereometamaterials concept [27] and tremendously enhances the versatility of metamaterial structures. By introducing the concept of metamaterial structures into CMP studies, we will have a powerful tool to explore the practical applications in cavity spintronics, especially for on-chip microwave devices.

1.2 Discovery of dissipatively coupled cavity-magnon-polaritons

The avoided crossing dispersion is also known as level repulsion [28], if we take the eigenfrequencies of the system as the energy level. Apart from coherent coupling, there is another type of coupling that shows an exotic behavior named level attraction. Instead of having avoided crossing behavior, the dispersion curve shows eigenmodes attraction and possible collapse. The level attraction dispersion was demonstrated in microwave optomechanical circuits by using negative energy in 2018 [29]. Soon after, the dissipative coupling in the CMP system has been demonstrated in 2019 [30], which was achieved by using a YIG sphere and one-dimensional waveguide cavity. Several months later, another

work displayed the so-called abnormal anticrossing effect (equivalent to level attraction) in reversed SRRs [31] independently. Furthermore, theoretical predication of using a intermediary mode with high dissipation can achieve level attraction [32]. Since then, the dissipative coupling has grown into a rapidly developing branch of cavity spintronics, and many following pieces of research confirm its ubiquitous nature. For example, level attraction dispersion has been discovered in planar structures and able to make on-chip devices [33], in a cylindrical microwave cavity that couples with a cavity antiresonance [34] and cavity mediated level attraction [35]. The fascinating properties of dissipative coupling include not only the attractive dispersion but also its linewidth repulsion. For example, the hybridized mode with lower damping has been observed with zero linewidth and the system condition at that point is named as the zero damping condition[36]. Theoretically, the linewidth can even become negative and this may have some potential applications. This phenomenon generates practical applications such as unidirectional invisibility that can make nonreciprocal devices [36]. Exploration of the topological properties such as the exceptional point and parity-time symmetry [37] is also fascinating since the properties would have fundamental difference due to non-Hermitian physics [38]. Meanwhile, the mystery remains in the dissipative coupling, especially the physical origin of zero and negative damping inspired different works researching the mechanisms [39, 40].

Following the discovery of level attraction, the exploration of the application of dissipative coupling has just been unfolding. Inspired by the research of dissipative coupling on planar structures [33] and pseudo-magnon modes [21], we would like to propose the research on level attraction in metamaterials. The level repulsion in metamaterials has been discovered [27] almost the same time as the development CMP. There remains a question in this overlapping field: Can level attraction exist in metamaterial structures, and what does it look like? Realizing the dissipative coupling in metamaterial is one of the goals of this thesis works. Another challenge that remains in the following research [36] is that the nonreciprocal device proposed has a relatively narrow bandwidth and is related to magnon bandwidth. Finding an approach to enhance its operation bandwidth will lead to broader applications such as unidirectional microwave transmission. We propose to use a magnetic loop antenna to control the radiation damping of magnon [41] to expand the bandwidth

of nonreciprocity. This work may offered a new degree of freedom to manipulate dissipative coupled CMP systems for unidirectional microwave transmission.

1.3 Thesis Outline

This thesis's research objectives are to explore the dissipative coupling in metamaterials structures and cavity photon-magnon systems for potential practical applications. In addition to the first chapter, three chapters will present the exploring dissipative coupling studies as follows:

- Chapter 2 introduces the theoretical background of the coupling mechanism for dynamic mechanical systems. The Lagrangian formalism of the classical system for both coherent and dissipative coupled has been derived. The difference in behaviors such as eigenvalue and eigenvectors between these two systems has been discussed. Apart from analytical solutions, we also present a basic introduction to numerical methods, including the finite element method and ordinary differential equation solvers. The results and applications of these numerical methods have been demonstrated, which provides information for field distribution of the experimental structure and time-domain analysis for dissipative coupling. These results offer an additional perspective to study the dissipative spin-photon coupling.
- Chapter 3 focuses on the key experimental signature of dissipative coupling using metamaterial structures (or pseudo-magnon). We first introduce the motivation and background of conducting this research, and theoretical and experimental results have been presented. The zero damping condition has been identified as a singularity in the system with complex analysis. Then we discuss the dispersion and linewidth evolution by using split-ring resonators, which has potential applications for making extremely sensitive detection. Furthermore, a voltage-controlled level attraction has been demonstrated by using an actively tunable split-ring resonator, which makes this technique feasible to integrate into on-chip devices.

- Chapter 4 explores the effective broadband nonreciprocal device by utilizing the interference between the coherent and dissipative coupling in CMP. A magnetic loop antenna was used to control the radiation of the magnon. Theoretically, the infinity isolation rate can be achieved due to the nature of the zero damping condition. Our design demonstrates a method of continuous tuning of the giant nonreciprocity. This work offers a novel approach for making broadband giant nonreciprocal devices in cavity magnonics.
- Chapter 5 concludes the results of the theories and experiments of dissipatively coupled systems. This thesis work confirms the dissipative coupling has a ubiquitous feature in which an open system embedded with two coupled resonance. This chapter also summaries the potential applications we explored by utilizing dissipative coupling. The outlook on this research project and some future works are proposed.

Chapter 2

Theoretical Background

In this chapter, we review the theoretical descriptions of coupled systems such as pendulum and RLC circuits in both Lagrangian formalism. In general, these methods simplify the complicated physical structures into damped harmonic oscillators and also preserve the fundamental physical properties. By using this way, the complex eigenfrequencies of the coupled system can be calculated to know the dispersion relation and the linewidth evolution of the hybridized system. These properties are critical to understand the energy flow between two oscillators and have potential applications on next-generation information procession.

2.1 Lagrangian formalism of coupled systems

The Lagrangian is a mathematical description of a dynamic system in Lagrangian mechanics, which involves the generalized coordinates and conservative force. Instead of defining forces in the system, the Lagrangian is defined by the difference between kinetic energy T and the potential energy U :

$$\mathcal{L} = T - U. \quad (2.1)$$

For the systems that involve non-conservative forces, we can define a Rayleigh's dissipation function \mathcal{F} that is proportional to the velocity of the motion [42], and lead to a generalized Euler-Lagrangian

equation:

$$\frac{d}{dt} \frac{\partial \mathcal{L}}{\partial \dot{\varphi}_i} - \frac{\partial \mathcal{L}}{\partial \varphi_i} + \frac{\partial \mathcal{F}}{\partial \dot{\varphi}_i} = 0. \quad (2.2)$$

Where $i = 1, 2, \dots, N$ is the index indicating which generalized coordinate is being used. Where N characterize the total number of degrees of freedom in the system. φ_i is the generalized coordinates for each degree of freedom. Notice here the non-conservative forces are equivalent to dissipative forces. According to the second law of thermodynamics, these forces irreversibly transfer mechanical energy into other energy forms such as thermal energy. The generalization of Euler-Lagrangian allows us to use the Lagrangian formalism for cases that involve friction such as damped oscillations.

In general, there are two different coupling mechanisms in coupled oscillation systems. One is coherent coupling, which can be represented by a spring which depends on both pendulums' relative position. Since the coupling force as a linear function of position which is a conservative force, the interaction process conserves energy. The other is dissipative coupling, which can be represented by a mechanical damper, which depends on each pendulum's velocity difference. In this coupling mechanics, each pendulum's velocity determines the coupling force which introduces a friction-like non-conservative force. Therefore, the coupling process would dissipate system energy.

2.1.1 Coherent coupled pendulums

For coupled harmonic pendulums (see Fig.2.1 (a)), the kinetic energy of the system is given by the summation of two individual pendulums:

$$T = \frac{1}{2}ml_1^2\dot{\varphi}_1^2 + \frac{1}{2}ml_2^2\dot{\varphi}_2^2, \quad (2.3)$$

where $m_{1,2}$ are the mass of oscillators, $l_{1,2}$ are the length of the pendulums. And the potential energy:

$$U = mgl_1(1 - \cos \varphi_1) + mgl_2(1 - \cos \varphi_2) + \frac{1}{2}\kappa(l \sin \varphi_1 - l \sin \varphi_2)^2, \quad (2.4)$$

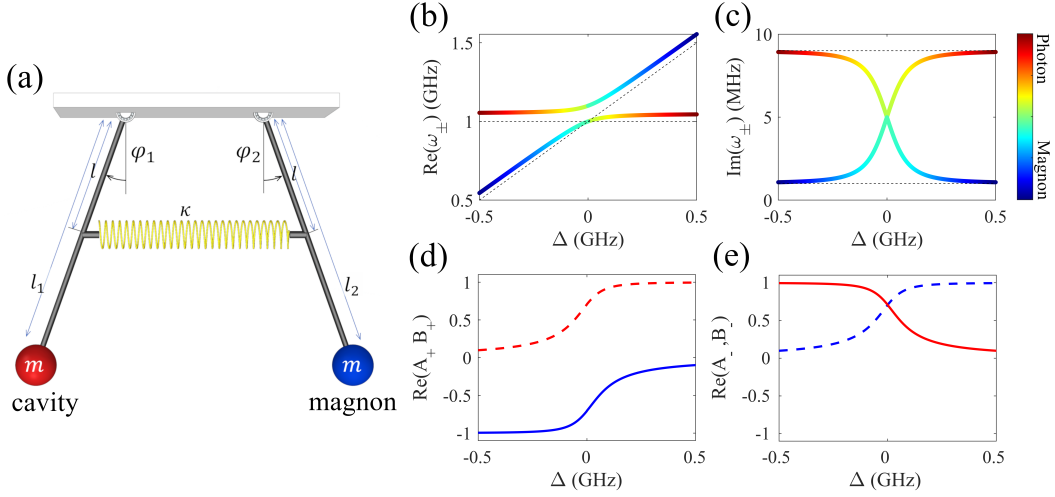


FIGURE 2.1: The coherent coupled pendulums system. (a) The schematic of the mechanical system connected by a spring. The oscillator in red (left) represent the cavity mode resonance, and the blue (right) is the magnon mode resonance. We assume the effective mass of each mode are same. (b) The real part of the eigenvalues (resonant frequencies) of the hybridization as a function of detuning gives the dispersion relation. (c) The imaginary part of hybridized eigenvalues (damping rates) exchange with each other due to coupling effect. The evolution of normalized eigenvector characterize a out-of-phase oscillation for higher frequency mode (d) and in-phase oscillation for lower frequency mode (e). All calculation is based on parameters $\omega_1/2\pi = 1$ GHz, $\lambda_1/2\pi = 9$ MHz, $\omega_2/2\pi \sim 0.5 - 1.5$ GHz, $\lambda_2/2\pi = 1$ MHz and coherent coupling strength as $\kappa/2\pi = 50$ MHz

where the first two terms are restoration force of the pendulum and the third term is the energy stored in the spring, with l gives the length of coupling length. Consider the system is in the linear regime, we use the $\sin \varphi_{1,2} = \varphi_{1,2}$ and $\cos \varphi_{1,2} = 1 - \varphi_{1,2}^2/2$ to simplify this nonlinear equation. Therefore, we have the Lagrangian of the system as:

$$\mathcal{L} = \frac{1}{2}ml_1^2\dot{\varphi}_1^2 + \frac{1}{2}ml_2^2\dot{\varphi}_2^2 - \frac{1}{2}mgl_1\varphi_1^2 - \frac{1}{2}mgl_2\varphi_2^2 - \frac{1}{2}\kappa l^2(\varphi_2 - \varphi_1)^2, \quad (2.5)$$

where the first two terms are the kinetic energy and the rest terms characterize the potential energy. To characterize the intrinsic damping induced by friction, the Rayleigh's dissipation function is defined as:

$$\mathcal{F} = \lambda_1 ml_1^2\dot{\varphi}_1^2 + \lambda_2 ml_2^2\dot{\varphi}_2^2, \quad (2.6)$$

where we have $\lambda_{1,2}$ as the intrinsic damping parameter that originates from the friction of each independent pendulum. If we assume the detuning of the system is relatively small $\Delta = \omega_1 - \omega_2 \sim 0$, the equations of motion are given by:

$$\begin{aligned}\ddot{\varphi}_1 + 2\lambda_1 \dot{\varphi}_1 + (\omega_1^2 + 2\omega_1 J_1) \varphi_1 - 2\omega_1 J_1 \varphi_2 &= 0, \\ \ddot{\varphi}_2 + 2\lambda_2 \dot{\varphi}_2 + (\omega_2^2 + 2\omega_2 J_2) \varphi_2 - 2\omega_2 J_2 \varphi_1 &= 0.\end{aligned}\tag{2.7}$$

Where the $\omega_i = \sqrt{g/l_i}$ ($i = 1, 2$) gives the resonance frequency of the i th uncoupled oscillator and $J_i = kl^2/(2\omega_i l_i^2) \ll \omega_i$ represents the coherent coupling strength due to spring. For a linear system, the solutions can be assumed as $\varphi_1 = Ae^{-i\omega t}$ and $\varphi_2 = Be^{-i\omega t}$. We substitute the solutions into Eqn.2.7, we have a matrix formulism as follow:

$$\begin{bmatrix} \omega - \tilde{\omega}_1 - J_1 & J_1 \\ J_2 & \omega - \tilde{\omega}_2 - J_2 \end{bmatrix} \begin{bmatrix} A \\ B \end{bmatrix} = \begin{bmatrix} 0 \\ 0 \end{bmatrix},\tag{2.8}$$

where we have used the approximation $\omega \approx \omega_1 \approx \omega_2$ and $\tilde{\omega}_i = \omega_i - i\lambda_i$ is the complex frequency of the uncoupled modes. The complex eigenvalues of the hybridized system are given by:

$$\tilde{\omega}_{\pm} = \frac{1}{2} \left[\tilde{\omega}_1 + \tilde{\omega}_2 + J_1 + J_2 \pm \sqrt{(\tilde{\omega}_1 - \tilde{\omega}_2 + (J_1 - J_2))^2 + 4J_1 J_2} \right].\tag{2.9}$$

Where the real part is the resonance frequency and the imaginary part characterizes the intrinsic damping rates of hybridized modes, respectively. The plot in Fig.2.1(b,c) shows the complex eigenvalue evolution with detuning, with the red color representing hybridized states that are more photon-like and blue color is for more magnon-like states. The resonance of the magnon-like states can be tuned which distinguishes the magnon-like mode from photon-like mode since the resonant frequency can be tuned by an external magnetic field. On the other hand, the original excitation is applied to photon-like mode since we directly input microwave photons into the system. The dispersion of coherent coupling preserve an avoided crossing behavior, if we regard the frequency

as energy level, such phenomena are also known as level repulsion, or avoided level crossing. The frequency gap at zero detuning corresponds to periodic oscillations of energy flow, which are also known as Rabi Oscillations, and were firstly studied in 1937 [43]. Rabi Oscillations occur in both classical systems and quantum systems that involves external driving. Furthermore, it have become the foundation of various spectroscopic techniques [44] and quantum transducers [45]. The eigenvectors can be obtained by solving Eqn.2.8 if we assume the symmetric coupling terms $J_1 = J_2 = J$, so we have:

$$\begin{bmatrix} A_+ \\ B_+ \end{bmatrix} = \begin{bmatrix} 2J \\ \tilde{\Delta} - \sqrt{\tilde{\Delta}^2 + 4J^2} \end{bmatrix}, \quad \begin{bmatrix} A_- \\ B_- \end{bmatrix} = \begin{bmatrix} 2J \\ \tilde{\Delta} + \sqrt{\tilde{\Delta}^2 + 4J^2} \end{bmatrix}. \quad (2.10)$$

The complex detunings are given by $\tilde{\Delta} = \tilde{\omega}_1 - \tilde{\omega}_2$. Examining under the special condition $\tilde{\Delta} = 0$, we identify the higher frequency mode as the out-of-phase mode $[1, -1]$ while the lower frequency mode as the in-phase mode $[1, 1]$. The calculation result of the real part of eigenvectors are shown in Fig.2.1 (d) with the higher energy mode and Fig.2.1 (e) with the lower energy mode. For the higher frequency mode, it can be interpreted by the restoration force of the spring accelerating the motion of the pendulum, which leads to a higher frequency than non-coupled modes. Foe the lower frequency normal mode, the two pendulums oscillate completely in-phase as if the spring does not exist, preserving the original frequency of its natural frequency. The cavity photons and magnons are generated from periodic motion just like the pendulums moving back and forth. The model of spring-coupled pendulums, therefore, can serve as the analog of the classical model coherent coupling in CMPs. If we take one resonance mode corresponds to a collective of cavity photons and the other represents the magnons in magnetic materials, the coherent coupling effect between these two particles would generates hybridized modes. These hybridized modes can be regarded as a kind of bosonic quasiparticles, which is named as "polaritons" with properties of both light and material. Therefore, A significant feature of polaritons is a strong dependency of the propagation speed of light through the crystal on the frequency of photon [46]. The discovery of polaritons

was first achieved by Tolpygo in 1950 [47] and Huang in 1951 [48], independently. Since then, different types of polaritons have emerged from research with various frequencies from microwave to visible light. For example, phonon polaritons result from the coupling of an infrared photon with an optical phonon [49], exciton-polaritons [50] result from coupling visible light with an exciton, surface plasmon polaritons [51] result from the coupling of surface plasmons with light, and magnon polaritons [30] result from the coupling of magnon with light.

If one mode frequency detunes from the other, we would expect that hybridized modes evolve closer to bare modes due to the decreasing of the coupling effect. From the perspective of the coupled pendulums, the coupled system would behave more like pendulum 1 or pendulum 2. From the CMP perspective, the decoupling process makes the quasi-particles more photon-like or more magnon-like. In light-matter interaction, the concept of coherence refers to the excitation of the materials (pendulum) have a well-defined phase relative to the incoming light (driving force). However, to display the avoided crossing dispersion, not only the phase relation but also the energy conservation during coupling needs to be taken into consideration.

2.1.2 Dissipative coupled pendulums

In the case that energy conservation has been violated during coupling process, an additional dissipation mechanism need to be introduced to the system. For the systems coupled with a dashpot or a damper (shown in Fig.2.2 (a)), a friction force that proportional to the velocity in the opposite direction would violet the energy conservation. So we have the Lagrangian as:

$$\mathcal{L} = \frac{1}{2}ml_1^2\dot{\varphi}_1^2 + \frac{1}{2}ml_2^2\dot{\varphi}_2^2 - \frac{1}{2}mgl_1\varphi_1^2 - \frac{1}{2}mgl_2\varphi_2^2. \quad (2.11)$$

It is very similar to the Lagrangian with the coherently coupled systems, with the potential induced by coupling vanished. The coupling effect through the velocity difference due to viscosity

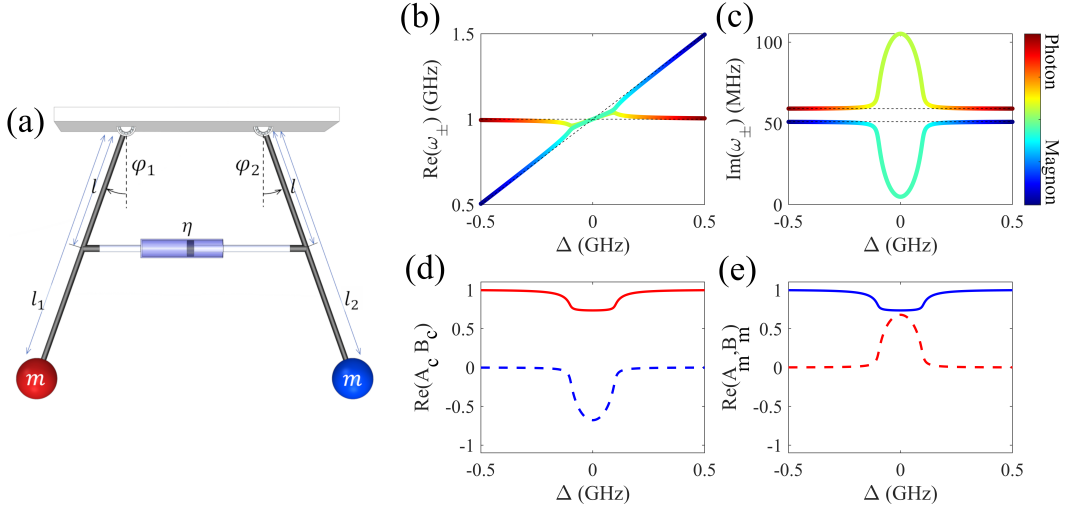


FIGURE 2.2: The dissipatively coupled pendulums system. (a) The schematic of the mechanical system connected by a dashpot. (b) The real part of the eigenvalues (resonant frequencies) of the hybridization as a function of detuning gives the dispersion relation. (c) The imaginary part of hybridized eigenvalues (damping rates) repels each other due to coupling effect. The evolution of normalized eigenvectors characterize a out-of-phase oscillation for cavity-like mode (c) and in-phase oscillation for magnon-like mode (d). All calculation is based on parameters $\omega_1/2\pi = 1$ GHz, $\lambda_1/2\pi = 9$ MHz, $\omega_2/2\pi \sim 0.5 - 1.5$ GHz, $\lambda_2/2\pi = 1$ MHz and coherent coupling strength as $\kappa/2\pi = 50$ MHz

of fluid inside the dashpot, is now defined in the Rayleigh's dissipation function:

$$\mathcal{F} = \lambda_1 m l_1^2 \dot{\varphi}_1^2 + \lambda_2 m l_2^2 \dot{\varphi}_2^2 + \eta(\dot{\varphi}_1 - \dot{\varphi}_2)^2, \quad (2.12)$$

where the η is the coupling dissipation parameter based on the velocity difference of two pendulums. The coupling term in the dissipation terms characterize the non-conservative nature of dashpot which indicates the coupling process does not conserve energy.

$$\ddot{\varphi}_1 + (2\lambda_1 + 2\Gamma_1)\dot{\varphi}_1 + \omega_1^2 \varphi_1 - 2\Gamma_1 \dot{\varphi}_2 = 0, \quad (2.13a)$$

$$\ddot{\varphi}_2 + (2\lambda_2 + 2\Gamma_2)\dot{\varphi}_2 + \omega_2^2 \varphi_2 - 2\Gamma_2 \dot{\varphi}_1 = 0, \quad (2.13b)$$

where the dissipative coupling strength is given by $\Gamma_{1,2} = \eta/(ml_{1,2}^2) \ll \omega_{1,2}$. Similarly, the complex eigenvalues are given by:

$$\tilde{\omega}_{\pm} = \frac{1}{2} \left[\tilde{\omega}_1 + \tilde{\omega}_2 + i(\Gamma_1 + \Gamma_2) \pm \sqrt{(\tilde{\omega}_1 - \tilde{\omega}_2 + i(\Gamma_1 - \Gamma_2))^2 - 4\Gamma_1\Gamma_2} \right], \quad (2.14)$$

the coupling term has a negative sign compared to the coherent coupling case. The real part of eigenvalues have been plotted in Fig.2.2 (b) in which the two colored curves attract each other near the center. The imaginary part of eigenvalues in Fig.2.2 (c) shows that one hybridized mode increase the damping by Γ while the damping of the other has decreased by Γ . The eigenvectors can be obtained using the same technique as the Eqn.2.10. In this case, we assume the coupling is symmetric $\Gamma_1 = \Gamma_2$.

$$\begin{bmatrix} x_{1+} \\ x_{2+} \end{bmatrix} = \begin{bmatrix} 2i\Gamma \\ -\tilde{\Delta} - \sqrt{\tilde{\Delta}^2 - 4\Gamma^2} \end{bmatrix}, \quad \begin{bmatrix} x_{1-} \\ x_{2-} \end{bmatrix} = \begin{bmatrix} 2i\Gamma \\ \tilde{\Delta} - \sqrt{\tilde{\Delta}^2 - 4\Gamma^2} \end{bmatrix}. \quad (2.15)$$

Since the coupling mechanism is different, using ω_1 -like mode and ω_2 -like mode instead of ω_{\pm} would help us to avoid the discontinuous. The ω_1 -like mode is given by ω_- when detuning is negative, and ω_+ when detuning becomes positive. Vice versa for the ω_2 -like mode. We have the ω_1 -like mode as the out-of-phase mode shown in Fig.2.2 (d) for real part , while the ω_2 -like mode as the in-phase mode shown in Fig.2.2 (e). It is clear that the in-phase mode (ω_2 -like mode) experience a large decrease of damping, and the out-of-phase mode (ω_1 -like mode) experience a large increase of damping. Level attraction dispersion was discovered in microwave frequency optomechanical circuits [29], and soon after, it has been found in cavity magnon polaritons [30].

The two coupled pendulums also have two different response. One is the steady state that we input a continuous wave and measures the response amplitude, the other one is the transient response in which process we input a pulse of signal and observe the system gradually return to the equilibrium points. Consider the transient response of the system, if we consider the time that coupling process took (interaction time) to be relatively short, the coupling process can be regarded

as a collision. Coherent coupling can be treated as completely elastic collision that preserves both the in-phase and out-of-phase normal modes. Therefore, coherent coupling displays a high fidelity feature in information processing. Both momentum and energy are conserved in the process. On the other hand, dissipative coupling refers to a completely inelastic collision that preserves only the in-phase mode at a long time scale since the velocity difference is zero, and the out-of-phase mode would quickly die away due to the nonzero coupling force.

2.2 Numerical methods in cavity magnonics

The electric and magnetic field distributions are critical to know the microscopic mechanism of coupling. The analytical solution of regular and electric closed structures such as rectangular, circular waveguides and cavities are easy to derive from solving Maxwell's equations. To acquire cavity photons with desired parameters, different designs of microwave resonators may be adopted, such as the planar microwave resonators which are known as microstrip resonators. However, when the structures and the boundary conditions become complicated, the analytical solutions are difficult to obtain. The numerical methods are necessary to get an insight of the designed structures.

2.2.1 Field Simulation using finite element analysis

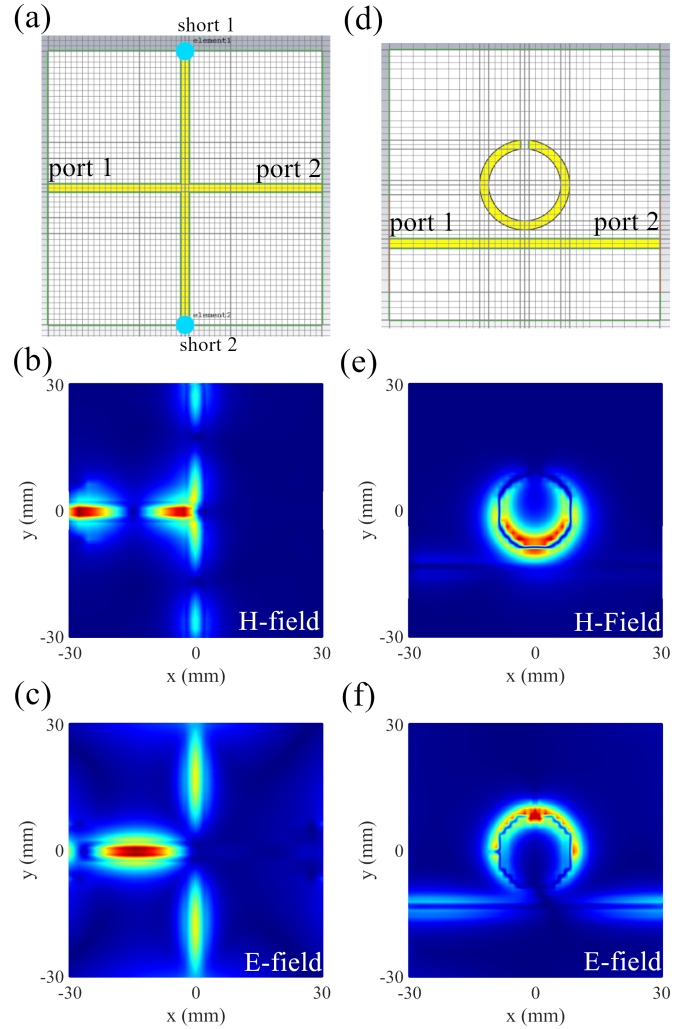
The finite element method (FEM) is a numerical technique for obtaining the approximate solutions to boundary-value problems in partial differential equations (PDEs) such as Maxwell's equations. This method origins from the structural analysis in aircraft design in the 1940s and was applied to electromagnetic analysis in 1968 [52] addressing applications to waveguide and cavity analysis. The most remarkable advantage of FEM is its capability to treat any type of geometry and material inhomogeneity without a need to alter the formulation or the programming code [52, 53]. With the development of computer technology, the FEM has been recognized as a general method widely applicable to engineering and mathematical problems.

The electromagnetic problem is primarily a problem of solving a set of Maxwell's equations with given boundary conditions. The domain discretization or meshing is the first and most important step in finite element analysis, which will affect the accuracy of the numerical results. The entire domain is subdivided into many small domains which referred to as elements. By keeping the finite element small enough, which is usually smaller than one-tenth of the wavelength, we are about to use linear or higher-order expansion to approximate the element's wave interior. We give an example of a mesh view that shows the three-dimensional domain discretization in Fig.2.3 (a) and (d). The cross cavity and split ring resonator are relatively simple planar structures adopted in this research; however, deriving the analytical solution for this problem would be extremely difficult. Once the system has been constructed and discretized, each of the elements can be regarded as an element in a matrix. The second is to select an interpolation function that provides an approximation of the unknown solution within an element. The selected interpolation function includes linear, quadratic, or higher-order polynomials that provide the unknown solution in an element. The third step is to formulate the system of equations. In this software, we solve Maxwell's equations to get the information we need. All the physical quantities and operators now can be written in matrices since we only consider the discrete system with nodes. Suppose we get the total number of N elements in the system, the partial differential equation can be constructed as follows:

$$[A][x] = [b]. \quad (2.16)$$

The matrix $[A]$ with size $N \times N$ represents the operators in the system with all known values. $[b]$ is a column matrix. It is determined based on the boundary conditions or the forced excitation. $[x]$ is the unknown parameters such as electromagnetic field we would like to solve. The final step is to solve the system of equations by using an iterative solver. The use of iterative solver is to avoid enormous storage space required by direct store $N \times N$ matrix so that we are able to solve large scale problems. Here, we use commercial computer software, CST microwave studio, to apply the powerful FEM. By setting the input microwave signal to 3.08 GHz, we can obtain the

FIGURE 2.3: Examples of finite element analysis of microstrip line structures by using CST microwave studio software. (a) The mesh view of the cross cavity with a length of 60 mm with the ports setup shown on the graph. The microwave input was exerted on port 1 and the frequency was set to 3.08 GHz to match the resonance. (b) Simulated magnetic field distribution of the cavity. (c) Simulated electric field distribution of the cavity. (d) The mesh view of a split-ring resonator excited by a microstrip transmission line. The microwave input was exerted on port 1 and the frequency was set to 1.97 GHz to match the resonance. (e) Simulated magnetic field distribution of split-ring resonator. (f) Simulated electric field distribution of split-ring resonator. All the field distribution shows the maximum absolute value on plane 1 mm above the microstrip.



electric, magnetic field distribution in Fig.2.3 (b) and (c), respectively. The split-ring resonator on a microstrip line has also been simulated, with the electric, magnetic field distribution shown in Fig.2.3 (e) and (f). Moreover, not only the field distribution but also the scattering parameters can be obtained. If we set the frequency range from 1 to 8 GHz, we can get the scattering parameters shown as Fig.2.4 (a,b) which we can compare the experimental measurements. From Fig.2.4, we can see the resonance shown in transmission and reflection in turns. These results are consistent with previous work [33].

As we can see from this example, FEM is a powerful tool for solving electromagnetic problems and getting an insight into the designed structure. This section only provides an elementary introduction of FEM which in reality would be much more complicated. Some of the most widely used FEM

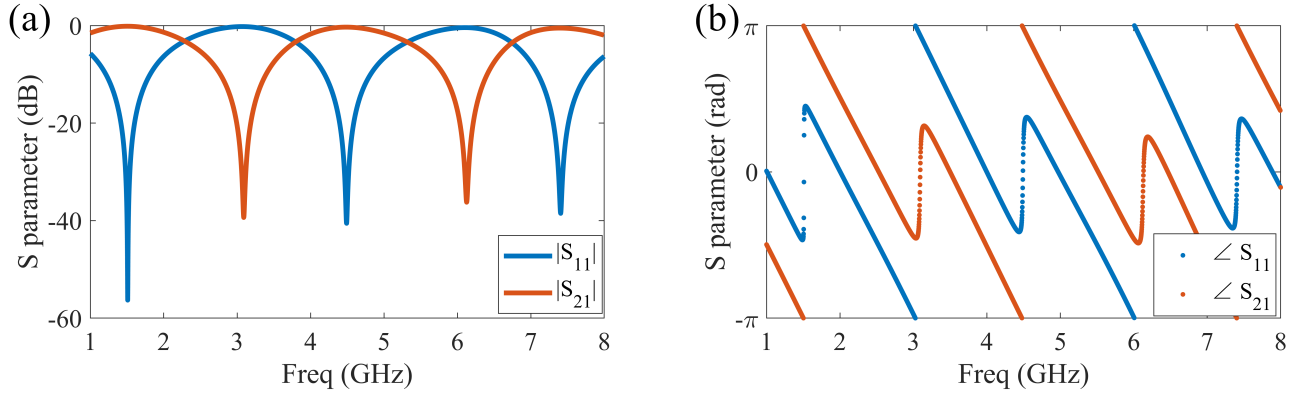


FIGURE 2.4: The simulated scattering parameters of the system shown in Fig.2.3 (a) with amplitude (a) and phase (b).

software includes CST STUDIO SUITE by Dassault Systèmes, high-frequency structure simulator (HFSS) by Ansys, and COMSOL multiphysics by COMSOL.

2.2.2 Time domain analysis using an ODE solver

The potential applications on quantum information and spintronic technologies drive the research of exchange-coupled spin ensembles which exhibit long coherence time and can be manipulated by microwave magnetic fields. The dynamics of coupled resonance systems such as cavity magnon polaritons in the frequency domain have been studied. The key properties have been elucidated by various theories, such as the dispersion anticrossing and linewidth exchange. Hybridizing the spin and photon with coherence properties makes the CMP system an excellent candidate for making quantum transducers[54]. In previous studies, the understanding of coherent and dissipative coupling in CMP systems mainly comes from frequency-domain studies. The time-domain response will provide more information and improve our understanding on CMP systems. Notably, the response around the zero-damping condition remains a mystery in dissipative coupling.

In this section, we study the dynamic of the coherent and dissipative coupling in the time domain by using numerical methods. Moreover, compare the result with publications from other researchers. The equations of motion such as Eqn.2.7, Eqn.2.13 are equalities involving a function and its derivatives known as the ordinary differential equations (ODEs). Solutions of these ODEs

in the frequency domain have been analytically studied. However, the time domain analysis could be difficult, and introducing the numerical methods into this field is necessary, especially for further studies that involve nonlinear effects. In numerical analysis, the Runge–Kutta methods [55, 56] are a family of implicit and explicit iterative methods for the approximate solutions of ODEs which have been widely adopted for numerical calculation of ODEs.

In principal, all n th-order ODEs could be rearranged in the form of first order ODEs as $\dot{x}(t) = f(x(t), x)$ with a known initial condition of the system $x(t = 0) = x_0$. The system state x is an unknown vector-valued function of time t . The idea of the Runge–Kutta methods is to get the approximate solution of the system from one specific time t_n to the next targeted time t_{n+1} with a certain time interval h (stepsize):

$$x(t_{n+1}) = x(t_n) + \int_{t_n}^{t_{n+1}} f(x(t), t) dt, \quad (2.17)$$

where $t_{n+1} - t_n = h$, and the system could be approximated using following form [57]:

$$x(t_{n+1}) = x(t_n) + \sum_{j=1}^n w_j k_j. \quad (2.18)$$

The next value $x(t_{n+1})$ is determined by the present value $x(t_n)$ plus the weighted average increment components which are based on the slope of the j th order of the interval. The increment of the j th order can be estimated as:

$$k_j = h f \left(x(t_n) + \sum_{i=1}^{j-1} \beta_{ji} k_i \right), \quad (2.19)$$

The parameter β_{ji} can be determined by the Runge–Kutta matrix [58], and the value of k_j needs to be determined by previous values k_i which contains several stages of calculation for each iteration step [59]. The weighted parameters are normalized so we have $\sum_{j=1}^n w_j = 1$ and greater weight are given to the increments near the midpoint. In practical applications, these methods require a certain order j which means the local truncation error is $\mathcal{O}(h^j)$ (the error caused by one iteration step) and the global truncation error is $\mathcal{O}(h^{j+1})$ (the cumulative error caused by many iteration steps).

One of the most popular ODE solvers is based on a six-stage, fifth-order, Runge–Kutta method that firstly introduced in the 1980s by Dormand and Prince [60]. It is so powerful that it can solve not only the linear ODEs but also effective on the nonlinear systems such as Van der Pol oscillators[61] and Duffing oscillators[62]. Numerical methods have been widely adopted in various kinds of problems such as the third integral of motion[63]. In order to analyze the coherent system the coherently coupled mechanical oscillators, the equations of motion in Eqn.2.7 can be rewritten as:

$$\begin{aligned}\dot{x}(1) &= x(2); \\ \dot{x}(2) &= -2\lambda_1 x(1) - (\omega_1^2 + 2\omega_1 J_1)x(2) + 2\omega_1 J_1 x(4); \\ \dot{x}(3) &= x(4); \\ \dot{x}(4) &= -2\lambda_2 x(3) - (\omega_2^2 + 2\omega_2 J_2)x(2) + 2\omega_2 J_2 x(2).\end{aligned}\tag{2.20}$$

The state of the system is represented by the vector \vec{x} , with $x(1)$ as the speed of oscillator 1, $x(2)$ as the position of oscillator 1, $x(3)$ as speed of oscillator 2 and $x(4)$ as position of oscillator 2. If we send a pulse of a microwave signal to the system, we would expect the cavity acquires some energy and moves to a higher energy position since the driving force is directly acting on the cavity photons. Therefore we set the initial condition as $\vec{x} = (0, 1, 0, 0)$. The calculation result for zero detuning is shown in Fig.2.5 (a) in which the red curve gives the position of photon resonator and blue curve gives the position of magnon resonator as a function of time. From Fig.2.5 (a), Rabi-oscillation has been directly displayed on the time-domain signal with a beat behavior that appears on both resonators in turns. However, the coupling strength is usually far less than the natural frequency of both resonators ($g \ll \omega_{1,2}$); we use the envelope of the oscillating signal to study the coupling energy of the oscillating signal. Fig.2.5 (b) provides the eigenfrequencies of the system. At the same time, Fig.2.5 (c) gives the amplitude evolution of independent oscillator in time-domain under various detuning. Interestingly, the envelope function and Rabi oscillations display distinctive behavior. The oscillation frequency will reach a minimum at zero detuning, and in the meantime,

the energy flow from the photon to magnon would reach to maximum. The time-domain mapping of cavity and magnon is shown in the Fig.2.5 (d) and Fig.2.5 (e), respectively. Our numerical results are consistent with other experimental works [12, 64], which proved the effectiveness of numerical methods.

Furthermore, if we perform a fast Fourier transformation on the calculated time-domain signal, we would get the frequency spectrum for photon and magnon oscillations, which is experimentally measurable. The control of Rabi oscillation by the detuning of two resonators allows us to extract the energy stored in both cavity and magnons.

For dissipative coupling, we have the equation of motion in Eqn.2.13 rewrite as:

$$\begin{aligned}\dot{x}(1) &= x(2); \\ \dot{x}(2) &= (-2\lambda_1 - 2\Gamma)x(1) - \omega_1^2 x(2) + 2\Gamma_1 x(3); \\ \dot{x}(3) &= x(4); \\ \dot{x}(4) &= (-2\lambda_2 - 2\Gamma)x(3) - \omega_2^2 x(2) + 2\Gamma_2 x(1),\end{aligned}\tag{2.21}$$

By setting the same initial condition as the coherent system, we can calculate the time-domain response of the dissipative coupled system. The calculation result for zero detuning ($\omega_1 = \omega_2$) is shown in Fig.2.6 (a) in which the oscillator 2 (in blue) displays a chasing behavior to the oscillator 2 (in red) and eventually the system settles in to a quasi-synchronized state. Fig.2.6 (b) gives the eigenvalues of the system which shows the level attraction. Fig.2.6 (c) shows the envelope of the oscillation signal of each oscillator under different detunings. As the detuning is large enough, the Rabi-like oscillation starts to appear on the magnon oscillators which indicate the system has two distinct eigenvalues. Fig.2.6 (d) and (e) shows the time-domain mapping for photon and magnon oscillator, respectively. Instead of exhibiting Rabi oscillations, the dissipative coupled oscillators show a synchronized behavior and reflected on the central bright stripe on mapping.

In conclusion, the coherently coupled system preserves the properties of conservation of both momentum and energy. The energy flow between the photon and magnon depends on the detuning

and initial state of the system. The system transforms and preserves the energy for a very long time again confirms its potential application for making high fidelity transducer in quantum information processing[65, 66]. On the other hand, the dissipatively coupled system only shows the properties of momentum conservation. The energy would be dissipated by the velocity difference between the two oscillators. Therefore, the system spontaneously eliminated the out-of-phase eigenmode and only the in-phase eigenmode could exist. The magnon is a nonlinear resonator if the excitation is strong enough. The numerical solution provides dissipative coupled resonators not only the clue in the linear regime but also nonlinear effect as well as the chaotic behavior. These results will benefit nonlinear dissipative coupling in future research.

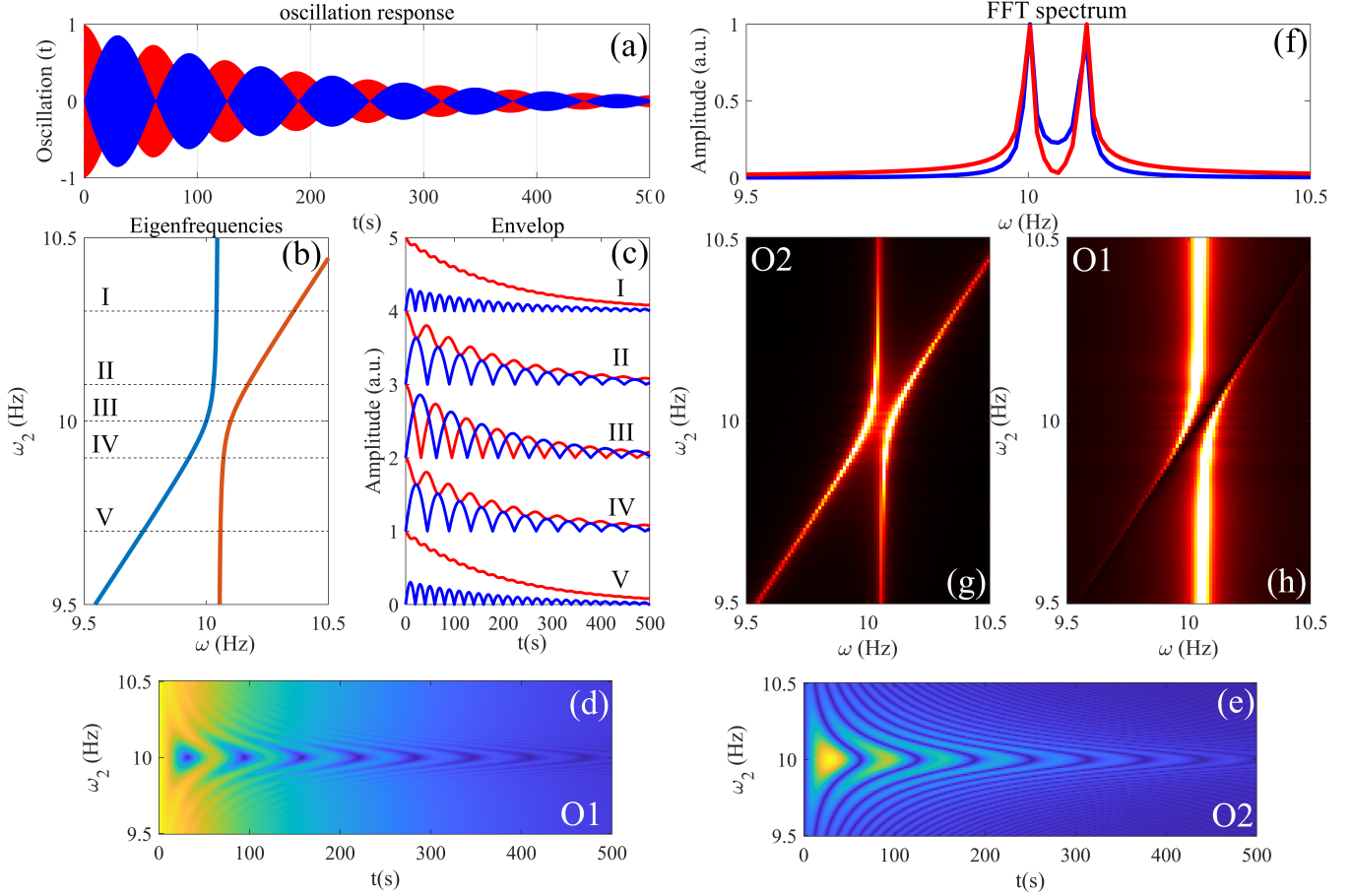


FIGURE 2.5: (a) At zero detuning, the Rabi-oscillation of system showing the photon resonator in red and magnon resonator in blue as a function of time. (b) The eigenvalues of the coherently coupled systems which preserve the anticrossing behavior. (c) Envelop as a function of time at various detunings with the cavity in red curve and magnon in blue. (d) The time-domain mapping of cavity resonator with detuning as and Y-axis and time as X-axis. The amplitude of the oscillation as the color-axis. (e) The time-domain mapping of magnon resonator. The colormap is on a linear scale. (f) The frequency spectrum acquired from the time-domain signal by using Fast Fourier Transformation. (g) Frequency spectrum mapping for oscillator 2 by FFT. (h) Frequency spectrum mapping for oscillator 1 by FFT. The parameters we used for calculation are given by $\omega_1/2\pi = 10$ Hz, $\omega_2/2\pi = 10$ Hz, $\lambda_1/2\pi = 0.01$ Hz, $\lambda_2/2\pi = 0.01$ Hz and coupling strength $J/2\pi = 0.1$ Hz.

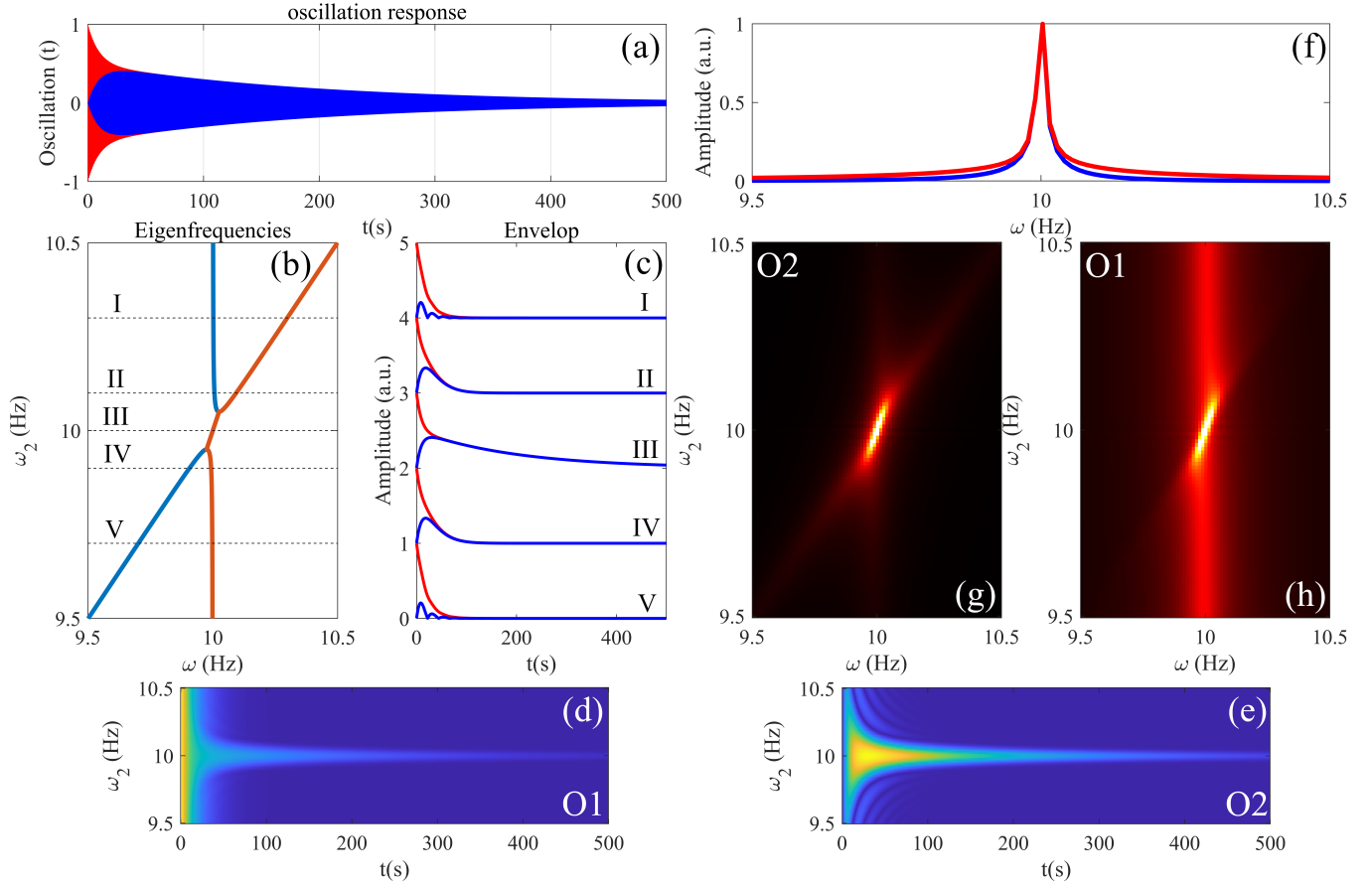


FIGURE 2.6: (a) The synchronization-like oscillation in which photon resonator in red and magnon resonator in blue as a function of time at $\Delta = 0$. (b) The eigenvalues of the dissipatively coupled systems. (c) Envelop as a function of time at various detuning with the cavity in red curve and magnon in blue. (d) The time-domain mapping of the cavity with detuning as and Y-axis and time as X-axis. The amplitude of the oscillation as the color-axis. (e) The time-domain mapping of magnon. The colormap is on a linear scale. (f) The frequency spectrum acquired from the time-domain signal by using Fast Fourier Transformation. (g) Frequency spectrum mapping for oscillator 2 by FFT. (h) Frequency spectrum mapping for oscillator 1 by FFT. The parameters we used for calculation are given by $\omega_1/2\pi = 10$ Hz, $\omega_2/2\pi = 10$ Hz, $\lambda_1/2\pi = 0.01$ Hz, $\lambda_2/2\pi = 0.01$ Hz and coupling strength $\Gamma/2\pi = 0.1$ Hz.

Chapter 3

Dissipatively coupled metamaterials for sensitive detection

3.1 Background

The prospect of constructing metamaterials with desirable properties has been inspiring intense research efforts for more than a decade [67–70]. These studies offer the freedom of assembling meta-cells with modern technology to create novel and unique features, such as negative refractive indices [71, 72], which are not available in natural materials. While the coupling interaction between meta-cells is somehow initially ignored according to the effective media model [68], it should always exist, particularly, when individual meta-cells are very close. Indeed, new phenomena, including electromagnetic cloaking [73], a plasmonic analogue of electromagnetically induced transparency [74], stereometamaterials [27] and coherent perfect absorbers [75] with *PT* phase transition [76], were introduced by the strong interaction between meta-cells.

Traditionally, the interaction between meta-cells is classified as electrical and magnetic coupling [27]. As a result of these coherent couplings, the avoided crossing behaviors are produced, which can be modeled using coupled *RLC* oscillators with mutual inductance and/or mutual capacitance [27, 77]. Besides the direct coherent interaction, each individual meta-cell should also interact with

the free space; as a result, the coherence and correlation between them result in an indirect dissipative coupling between meta-cells as that in other coupled systems [78–80]. The consequence of dissipative coupling is not only the distinguished dispersion shown as level attraction in contrast to level repulsion due to coherent coupling,[81] but also paves a way to explore new physics phenomena and construct novel microwave and optical devices by engineering the dissipation processes of the system. Research in this area covers broad fields in physics, including quantum computation and quantum-state engineering [82], super-scattering [83, 84], anti-parity-time system[85], non-Hermitian fermionic superfluidity [86] and one-way microwave transmission [36].

However, the distinct features of dissipative coupling were often dominated by a much stronger effect caused by the direct coherent coupling. Until very recently, intriguing dissipative couplings were experimentally demonstrated in a cavity magnon-photon system [81], where the coherent coupling is effectively suppressed by placing the magnetic sample (with a deep-subwavelength size) at the node of the microwave magnetic field [81]. This discovery provides insights for constructing the dissipative coupling in a metamaterial structure, which we demonstrate in this work. As a consequence of dissipative coupling being involved, we report the observation of a hybridized mode with a zero-damping rate, accomplished with a very sharp transition of microwave transmission. Our design breaks the previous limitation in microwave switching and sensing, which often suffers from the poor quality-factor (often < 100) in a planar resonator at room temperatures [87]. Furthermore, the cancellation effect between the electric coupling and magnetic coupling reveals additional freedom to tune such a zero-damping condition (ZDC) in a coupled system when the dissipative coupling is introduced.

This work is split into two main sections, which discuss the theoretical model and experimental results. In the theoretical model part, we first provide a general formula of a coupled *RLC* circuit. By side-coupled with a transmission line, we deduce the resonance frequencies of the hybridized mode and microwave transmission of the system and find the strict condition of the zero-damping rate in hybridized modes. Then we implement a coupled metamaterial structure involving dissipative coupling and experimentally demonstrate a sharp transition of microwave transmission. Finally, we

present a planar metamaterial device with capabilities of electrically controlled level attraction and linewidth narrowing.

3.2 Theoretical model

In order to provide a general view on the coupling effect between two resonant structures regardless of the particular design of the resonator, we apply an *RLC* circuit model. Here an electrical circuit consisting of a resistor (R), an inductor (L), and a capacitor (C), is connected in series or parallel, forming a damped harmonic oscillator for current with a resonance frequency [$\omega_0 \equiv 1/(LC)^{1/2}$]. In the following text, we will transform the conventional circuit description of a *RLC* resonator from a representation in terms of voltages and currents to one in terms of accumulated charges and generalized fluxes. Using the charge Q accumulated in the resonator as a generalized coordinate, the Lagrangian can be constructed as $\mathcal{L} = L(\dot{Q}^2 - \omega_0^2 Q^2)/2$ by using the kinetic energy $T = L\dot{Q}^2/2$ and electrostatic energy $V = Q^2/2C$ stored in the capacitor.

3.2.1 General formula of a coupled *RLC* circuit

We first study the two coupled *RLC* resonators in a closed system, where the resonators are isolated with free space. Based on the generalized coordinate Q , the Lagrangian of the coupled *RLC* resonators is the combination of two individual elements with the additional electric and magnetic coupling between them.

$$\mathcal{L} = \frac{L}{2}(\dot{Q}_1^2 - \omega_1^2 Q_1^2) + \frac{L}{2}(\dot{Q}_2^2 - \omega_2^2 Q_2^2) + M_H \dot{Q}_1 \dot{Q}_2 - M_E \omega_1 \omega_2 Q_1 Q_2. \quad (3.1)$$

Here the notion 1(2) represents the resonator 1(2). The mutual inductance M_H and mutual capacitance M_E are produced by the magnetic and electric interactions between two resonators, respectively. In general, the amplitude of M_H and M_E may be defined on the basis of the ratio of coupled magnetic and electric energy to the stored energy, respectively. Therefore, the sign of

M_H and M_E can be either positive or negative, determined by the enhancement or reduction of the stored energy of uncoupled resonators [88]. The direct evaluation of them requires the knowledge of the field distributions of the resonators as well as the space integrals.

The resonant frequency $\omega_i = 1/\sqrt{L_i C_i}$. The coherent coupling between metamaterials has been studied in previous works [27]. However, the energy loss during the coupling effect has not been discovered. And the Rayleigh's dissipation function is given by:

$$\mathcal{F} = \lambda_1 L \dot{Q}_1^2 + \lambda_2 L \dot{Q}_2^2 + M_R \dot{Q}_1 \dot{Q}_2. \quad (3.2)$$

Where $\lambda_{1,2}$ characterize the intrinsic damping of independent RLC resonators whose origin is from the Ohm's Law. The dissipative coupling term M_R originates from the field leakage of mutual inductance [89, 90]. However, the dissipative term is usually small compare to coherent terms κ_E and κ_H . The dissipative nature of the leakage inductance means this energy loss preserve the properties of mutual resistance [91] or resistive coupling [33]. The equation of motions are given by:

$$\begin{aligned} \ddot{Q}_1 + 2\lambda_1 \dot{Q}_1 + \omega_1 Q_1 - \kappa_H \ddot{Q}_2 - \kappa_E \omega_1 \omega_2 Q_2 - \kappa_R \dot{Q}_2 &= 0 \\ \ddot{Q}_2 + 2\lambda_2 \dot{Q}_2 + \omega_2 Q_2 - \kappa_H \ddot{Q}_1 - \kappa_E \omega_1 \omega_2 Q_1 - \kappa_R \dot{Q}_1 &= 0. \end{aligned} \quad (3.3)$$

Where $\kappa_E = M_E/L$ is the electric coupling, $\kappa_H = M_H/L$ is the magnetic coupling and $\kappa_R = M_R/L$ is the dissipative (resistive) coupling. The effect of magnetic coupling is negative relative to electric coupling according to the relative current direction [92] leading to the cancellation of total coherent coupling, in this case, the dissipative coupling dominates.

The eigenfrequencies of this coupled system can be obtained as

$$\tilde{\omega}_{\pm}^c = \frac{\omega_1 + \omega_2}{2} + i \frac{\gamma_1 + \gamma_2}{2} \pm \sqrt{\left(\frac{\omega_1 - \omega_2}{2} + i \frac{\gamma_1 - \gamma_2}{2} \right)^2 + 4(J + i\Gamma)^2}, \quad (3.4)$$

where $J = \kappa_E - \kappa_H$ is the coherent coupling strength and $\Gamma = \kappa_R$ is the dissipative coupling strength. In most of the systems studied previously, the term of the coherent coupling would be far larger

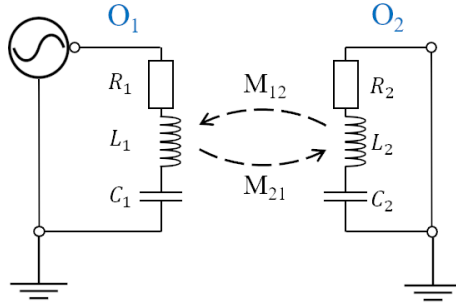


FIGURE 3.1: Equivalent RLC-circuit for coherent coupling.

than the dissipative coupling which makes the observation of level attraction extremely difficult. Therefore, the term Γ usually is a negligible quantity.

Since the M_E and M_H terms may be in opposition to each other, the net effect of the coherent coupling may be zero at a transition condition near $\omega_1 \sim \omega_2$. This observation is the key to construction of the systems dominated by dissipative coupling in a coupled metamaterial structure. In this work, we use a split-ring-resonator (SRR) based metamaterial structure, which is based on the following consideration: (1) an SRR can be excited by either a magnetic field or an electric field [93], and (2) the amplitude of M_E and M_H can be comparable in a coupled metamaterial structure composed of SRRs [27, 29].

The microscopic difference between the coupled RLC circuits and pendulums (in Chapter 2) is the coupling mechanics. The electromagnetic system is based on the mutual inductance (capacitance) instead of a physical component such as a spring or dashpot. Suppose we have the mutual inductance between resonator 1 and resonator 2 noted as $M_{12} = M_{21}$. According to the Kirchhoff's voltage law $\sum_{n=1}^n V_n = 0$ (see fig.3.1), we have:

$$\begin{aligned}\dot{Q}_1(R - i\omega L - \frac{1}{i\omega L}) - i\dot{Q}_2\omega M_{12} &= 0 \\ -i\dot{Q}_1\omega M_{21} + \dot{Q}_2(R - i\omega L - \frac{1}{i\omega L}) &= 0\end{aligned}\tag{3.5}$$

This can also be understand by Faraday's law $\int_L \vec{E} \cdot d\vec{l} = -d\Phi_B/dt$, that one resonator's induced

voltage only depends on the current on other resonator instead of the current difference. One resonator generates an effective oscillating current $I_1(2) = \dot{Q}_1(2)$ and this current will produce a magnetic flux on the other resonator according to M_{12} . From Eqn.3.5 we can know that the coupling effect depends on \dot{Q}_2 instead of $\dot{Q}_1 - \dot{Q}_2$. This difference in coupling dependence could explain why there is a frequency shift on the mechanical system but not for the polariton system. For polariton systems, the coupling term would only rely on the states of the other resonator. For mechanical systems, however, the coupling would rely on the difference between the other resonator. Specifically, the coherent coupling depends on the position of the other resonator in polaritons systems, but depends on position difference of two oscillators for mechanical systems. This is the fundamental difference between electromagnetic system and mechanic systems.

With the direct coherent coupling deduced from Eq.3.4 for the closed environment, now we discuss the indirect dissipative coupling between the two resonators in the open environment. The eigenmode of the coupled metamaterial structure in the closed environment, described in Eq. (3.4) shows the common mode-anticrossing behavior. The response eigenmodes may no longer follow the same rule if coupled with this structure via ports. Below we provide a formalism that allows us to calculate the microwave transmission/reflection as well as the dispersion of the hybridized modes in such an open system.

Figure 3.2 shows the schematic design, where the metamaterial structure described by Eq. (3.4) is side-coupled to a transmission line. The energy stored inside the resonators can decay into the ports, and at the same time, the incoming wave from the ports can inject energy into the resonators. Therefore, κ_1 and κ_2 describes the decay rates due to the coupling of the individual resonator with the ports. The existence of external damping on both resonators sustained an effective coupling effect due to the phase difference relative to traveling wave. For such an open system, the dynamic equations may be written as [36, 79, 80] :

$$\frac{d}{dt} \begin{bmatrix} Q_1 \\ Q_2 \end{bmatrix} = (i\Omega - \Lambda) \begin{bmatrix} Q_1 \\ Q_2 \end{bmatrix} + K \begin{bmatrix} s_{1+} \\ s_{2+} \end{bmatrix}, \quad (3.6)$$

where the matrices $\Omega = \begin{bmatrix} \omega_1 & J \\ J & \omega_2 \end{bmatrix}$ and $\Lambda = \begin{bmatrix} \gamma_1 + \kappa_1 & \Gamma \\ \Gamma & \gamma_2 + \kappa_2 \end{bmatrix}$ represent resonance frequencies (including the coherent coupling J between resonators) and the decay (including the dissipative coupling Γ between resonators), respectively. $\Gamma = \sqrt{\kappa_1 \kappa_2}$ represents the indirect coupling between the resonators, which is induced by the coherence and correlation between κ_1 and κ_2 [94].

The resonant mode is excited by the incoming waves s_{1+} and s_{2+} from ports 1 and 2 with the coupling matrix $K = \begin{bmatrix} \sqrt{\kappa_1} & \sqrt{\kappa_1} \\ \sqrt{\kappa_2} & \sqrt{\kappa_2} \end{bmatrix}$. The excited resonator mode coupled with the outgoing waves s_{1-} and s_{2-} at the ports with the coupling matrix K according to

$$\begin{bmatrix} s_{1-} \\ s_{2-} \end{bmatrix} = C \begin{bmatrix} s_{1+} \\ s_{2+} \end{bmatrix} + K^T \begin{bmatrix} Q_1 \\ Q_2 \end{bmatrix}, \quad (3.7)$$

where the scattering matrix C represents the interaction between incoming and outgoing waves through a direct pathway, in addition to the resonance-assisted coupling between two ports.

Because κ_2 is orders of magnitude weaker than κ_1 in our following experiments, we can neglect both the decay and excitation caused by κ_2 for simplicity. In this case, the microwave transmission $S_{21} = s_{2-}(s_{2+} = 0)/s_{1+}$ for the side-coupled system (Fig.3.2), i.e., $C = \begin{bmatrix} 0 & 1 \\ 1 & 0 \end{bmatrix}$, can be presented in the form:

$$S_{21} = 1 - \frac{\kappa_1}{i(\omega - \omega_1) + (\gamma_1 + \kappa_1) + \frac{(J + i\Gamma)^2}{i(\omega - \omega_2) + (\gamma_2 + \kappa_2)}}, \quad (3.8)$$

In this case, the resonance profile of the bare cavity ($J = \Gamma = 0$) becomes a Fano window in the continuum spectrum, or in other words, a symmetric quasi-Lorentzian anti-resonance [34, 95, 96].

3.2.2 Resonance frequency and zero-damping condition in a coupled RLC circuit

As the anti-resonance nature of the involved cavity, the resonance frequency of the hybridized modes corresponds to the minimum microwave transmission [34, 36, 81], which can be determined based

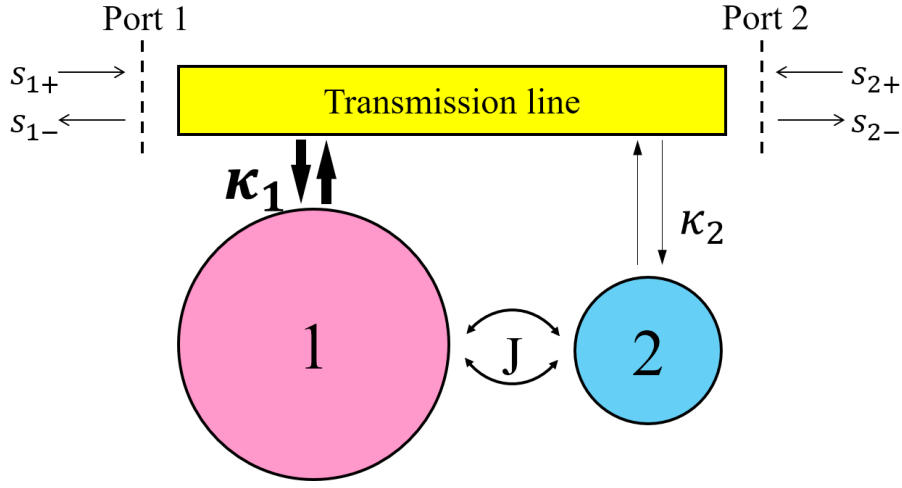


FIGURE 3.2: Schematic of two coupled resonator in a two-port system, which is side-coupled with a transmission line.

on S_{21} spectra in Eq. (3.8). Then we have

$$\tilde{\omega}_{\pm} = \frac{1}{2} \left[(\tilde{\omega}_1 + \tilde{\omega}_2) \pm \sqrt{(\tilde{\omega}_1 - \tilde{\omega}_2)^2 + 4G^2} \right], \quad (3.9)$$

where $\tilde{\omega}_1 = \omega_1 + i\gamma_1$, $\tilde{\omega}_2 = \omega_2 + i(\gamma_2 + \kappa_2)$ and the complex coupling constant $G = J + i\Gamma$.

Comparing with the eigenfrequencies $\tilde{\omega}_{\pm}^c$ described in Eq. (3.4), the dissipative coupling constant Γ is introduced for an open system. The impact of Γ is not trivial, which results in the experimental observation of level attraction with a coalescence of hybridized modes, distinctly different from level repulsion with mode anticrossing caused by coherent coupling. For illustrating the unique features caused by the dissipative coupling Γ , we plot the calculated $\tilde{\omega}_{\pm}$ in Figs. 3.3 (a-f) at three typical coupling cases: (i) $J \neq 0$ and $\Gamma = 0$, (ii) $J = 0$ and $\Gamma \neq 0$, and (iii) $J = \Gamma \neq 0$.

Ignoring the dissipative coupling by setting $\Gamma=0$, Figure 3.3(a) shows a clear avoid-crossing behavior in $\text{Re}(\omega_{\pm})$, with horizontal and diagonal dotted lines indicating the dispersion of the two uncoupled RLC oscillators respectively. This effect is well known in quantum physics and quantum chemistry, representing as a signature of the coherent interaction between two subsystems. Figure 3.3(b) illustrating another feature of coherent coupling, linewidth evolution. From Eq. (3.9) one

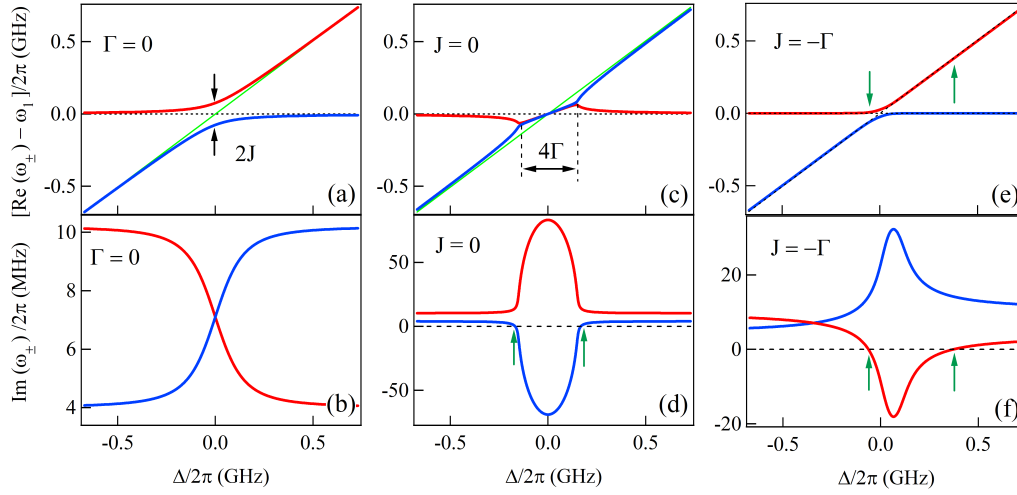


FIGURE 3.3: The real and imaginary contributions of the complex frequencies ω_{\pm} of the hybridized modes, calculated as a function of ω_2 according to Eq. (3.9) showing distinguished hybridization and linewidth evolution signatures for (a, b) $J/2\pi=0.07$ GHz and $\Gamma=0$, (c, d) $J=0$ and $\Gamma/2\pi=0.07$ GHz, and (e, f) $J/2\pi=\Gamma/2\pi=0.03$ GHz, respectively. Here we use $\omega_1/2\pi=2.5$ GHz, $\gamma_1/2\pi=0.01$ GHz and $(\gamma_2 + \kappa_2)/2\pi=0.02$ GHz. The vertical and diagonal dotted lines in (a,c,e) indicate the uncoupled dispersions for two RLC oscillators respectively. The vertical dotted lines in (d,f) correspond to zero damping rate and the arrows indicate the zero damping condition.

can find the $\text{Im}(\tilde{\omega}_+) + \text{Im}(\tilde{\omega}_-) \equiv \gamma_1 + \gamma_2 + \kappa_2$ and furthermore $\text{Im}(\omega_{\pm})$ is bounded in a range between γ_1 and $\gamma_2 + \kappa_2$.

In another extreme case at $J=0$, Equation (3.9) reveals distinguished signatures compared with the previous one. Here the dissipative coupling is characterized by level attraction and damping repulsion, as shown in Fig. 3.3(c) and 3.3(d), respectively. From a mathematical point of view, level attraction and level repulsion are equivalent to each other through frequency and damping exchange in the plane of complex eigenvalues; however, the physical meaning and consequences are very different. As additional dissipation channels are introduced, the damping rate of the hybridized mode is either enhanced or suppressed when compared with the uncoupled mode. Under appropriate conditions, the damping rate of the hybridized mode may reach zero, as clearly indicated by the arrows in Fig. 3.3(d).

Mathematically, the ZDC corresponds to $\text{Im}(\tilde{\omega}_{\pm}) \equiv 0$. Combining it with Eq. (3.9), we find

that the frequency detuning $\Delta = \omega_1 - \omega_2$ and the resonance frequency $\omega_{\pm} = \text{Re}(\tilde{\omega}_{\pm})$ at ZDCs should satisfy

$$\Delta_{\pm}^{ZDC} = \frac{(-\gamma_1 + \gamma_2 + \kappa_2)J\Gamma \pm (\gamma_1 + \gamma_2 + \kappa_2)\sqrt{[J^2 + \gamma_1(\gamma_2 + \kappa_2)][\Gamma^2 - \gamma_1(\gamma_2 + \kappa_2)]}}{\gamma_1(\gamma_2 + \kappa_2)}, \quad (3.10a)$$

$$\omega_{\pm}^{ZDC} = \omega_1 + \frac{-JG \pm \sqrt{[J^2 + \gamma_1(\gamma_2 + \kappa_2)][\Gamma^2 - \gamma_1(\gamma_2 + \kappa_2)]}}{\gamma_2 + \kappa_2}. \quad (3.10b)$$

Then substituting Eq. (3.10a) into Eq. (3.8), We have $S_{21}^{ZDC} \equiv 0$, and also find the microwave transmission varies orders of magnitude in a very narrow window near the ZDC. Such a strict feature clearly demonstrates the potential for developing microwave switching devices by introducing dissipative coupling in a coupled metamaterial structure.

Furthermore, according to Eq. (3.10a), we can summarize some basic properties of the ZDC:

- For pure coherent coupling ($\Gamma = 0$), the corresponded coherent energy exchange process does not introduce additional damping terms into the system. It hence only results in the exchange of the damping rate between two modes. As a consequence, there is no ZDC [Δ_{\pm}^{ZDC} calculated from Eq. (3.10a) is a pure imaginary number].
- For pure dissipative coupling ($J = 0$), ZDCs occur at $\Delta_{\pm}^{ZDC} = \pm(\gamma_1 + \gamma_2 + \kappa_2)\Gamma / \sqrt{\gamma_1(\gamma_2 + \kappa_2)}$, close to the bifurcation points ($\Delta_{\pm} = \pm 2\Gamma$) if the difference between γ_1 and $(\gamma_2 + \kappa_2)$ is not too large.
- If both coherent coupling and dissipative coupling are involved and $|J, \Gamma| \gg \gamma_1, \gamma_2 + \kappa_2$, $\Delta_{+}^{ZDC} \simeq 2J\Gamma / (\gamma_2 + \kappa_2)$ and $\Delta_{-}^{ZDC} \simeq -2J\Gamma / \gamma_1$ [indicated by arrows in Figs. 3.3(e) and (f)]. The sign of $J\Gamma$ determines the position of ZDC at the upper branch $\tilde{\omega}_+$ or down branch $\tilde{\omega}_-$ of the hybridized modes.

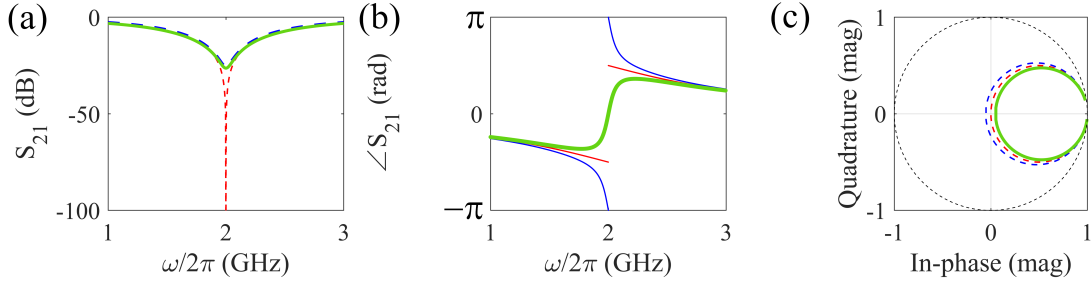


FIGURE 3.4: Calculated transmission amplitude (a) and phase (b) and The I/Q diagrams (c) for positive damping (in green curves), zero damping (in red curves) and negative damping (in blue curves). Parameters we used are $\omega_1 = 2$ GHz, $\gamma = 0, \pm 50$ MHz, and $\kappa = 0.99$ GHz.

3.2.3 Complex analysis on transmission

To analysis the difference between the coherent coupling and dissipative coupling, a study on complex transmission (S_{21}) of resonance as well as coupled resonances are critical, especially to understand the zero damping and negative damping. Starting with a bare bandstop resonator, the transmission coefficient can be derived as [95]:

$$S_{21} = 1 - \frac{\kappa}{i(\omega - \omega_1) + \kappa + \gamma}, \quad (3.11)$$

If we extract the real part and imaginary part of the transmission, we have the in-phase signal as X -axis and quadrature-phase as the Y -axis:

$$\begin{aligned} X &= \text{real}(S_{21}) = \frac{(\omega - \omega_1)^2 + \gamma(\gamma + \kappa)}{(\omega - \omega_1)^2 + (\kappa + \gamma)^2}, \\ Y &= \text{imag}(S_{21}) = \frac{\kappa(\omega - \omega_1)}{(\omega - \omega_1)^2 + (\kappa + \gamma)^2}. \end{aligned} \quad (3.12)$$

Plotting the In-phase (I) and quadrature-phase (Q) components will give us a I/Q diagram which is equivalent to a polar plot [97]. It is easy to prove that the trajectory of this bare resonator follows a circle on I/Q diagrams (shown in Fig.3.4 (c)):

$$(X - X_c)^2 + Y^2 = R^2, \quad (3.13)$$

where $X_c = 1 - \kappa/(2\kappa + 2\gamma)$ gives the center of the circle and $R = \kappa/(2\kappa + 2\gamma)$ gives the radius of the circle. For the resonator with non-zero damping ($\gamma > 0$), the complex trajectory starts from the $(1, 0)$ point and draws a circle in the first and fourth quadrant which would never enclose or cross the origin. To explore a layer further, let us design a thought experiment, once the intrinsic damping of the single resonator reaches zero, the trajectory of the I/Q diagram would cross the origin which leads to $S_{21} = 0$ at this condition. For the transmission amplitude in dB scale which is shown in Fig.3.4 (a), this zero-damping leads the transmission curve to negative infinity at resonance, and for the phase, this would have a π -phase jump at the resonance which exhibits a singularity due to the discontinuous and lack of analyticity [98] (see Fig.3.4 (b)). Furthermore, if the damping becomes negative, the I/Q curve would enclose the origin and can be observed in all four quadrants. With the increment of the magnitude of the negative damping, the complex trajectory would eventually reach the unity circle ($\gamma = -\kappa$) before we have an amplification of the signal. The amplification of the signal is not physical since we do not have an energy source.

Negative damping is strongly related to a relatively large external damping. The external damping rate is a factor characterizing how the resonator itself couples to external resistance [99], on the other hand, it dissipates energy. If we have positive intrinsic damping, we would expect a increment of total damping since the intrinsic damping dissipates energy the same way as the external damping. For negative intrinsic damping, however, it compensates a part of the external damping as if a part of the energy has been "returned". Leading the system to have an even lower total damping. If we only take transmission amplitude into consideration, we can get the absolute value of the damping rate. However, there is no way to tell the damping of the resonance is positive or negative. Therefore, the information in phase is crucial to determine the sign of the damping rate. Without looking at the phase of the transmission, it is impossible to tell if the resonance mode has negative or positive damping. Theoretically, the negative damping for a single resonance is not achievable since this requires a component with negative resistance ($R < 0$), which violates the second law of thermodynamics. However, the negative damping can be achieved in a coupled system by utilizing dissipative coupling.

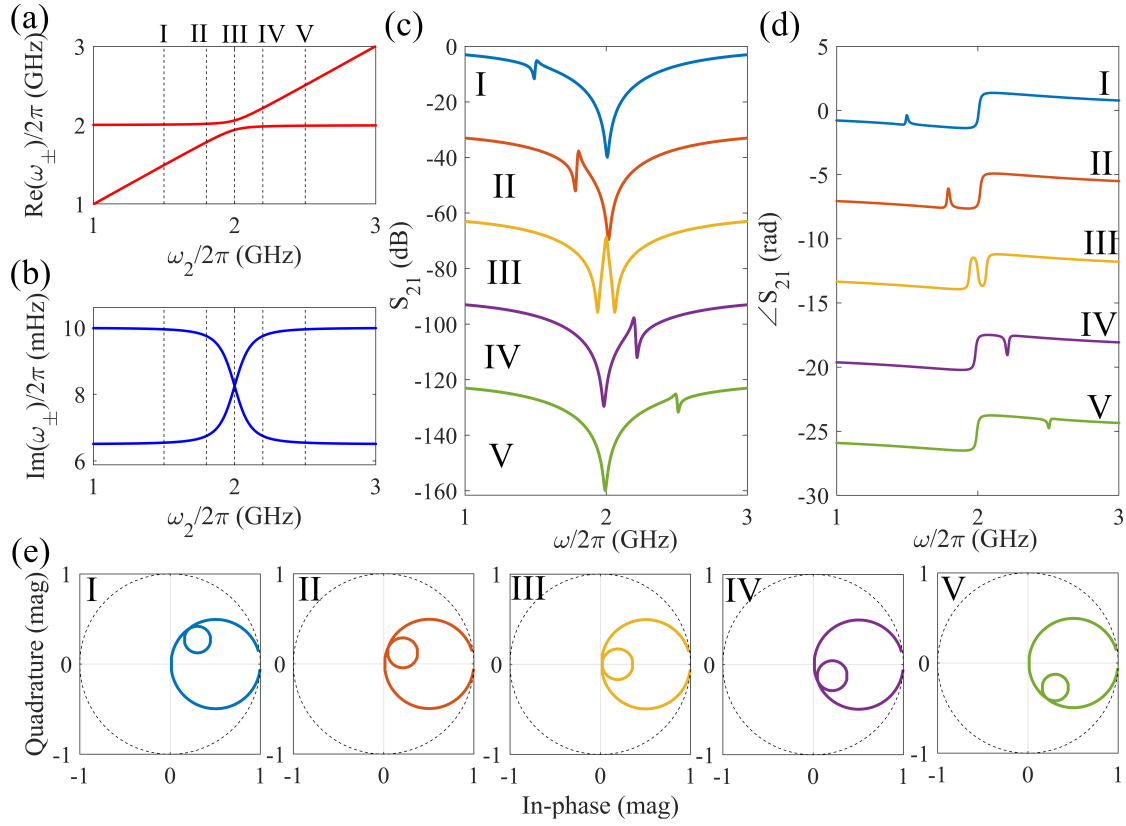


FIGURE 3.5: The I-Q analysis for coherent coupling. (a) The calculated level repulsion dispersion. (b) The calculated linewidth exchange evolution. (c) Waterfall plot of $|S_{21}|$ amplitude in dB scale as a function of detuning. (d) Waterfall plot of S_{21} phase in radian. Shifts have been applied to different spectrums for clarification. (e) The I/Q diagrams under various detunings. The parameter we used for calculation is $\omega_1 = 2$ GHz, $\kappa_1 = 0.99$ GHz, $\gamma_1 = 10$ MHz, $\omega_2 = 1 \sim$ GHz, $\kappa_2 = 0$ MHz, $\gamma_2 = 6.5$ MHz, $J = 60$ MHz and $\Gamma = 0$ MHz.

For coherent coupling (with $\Gamma = 0, J > 0$), we take the Taylor expansion on Eqn.3.8 near $\omega \approx \omega_2$.

We have:

$$S_{21} = 1 - \frac{\kappa_1}{\kappa_1 + \gamma_1} + \frac{1}{(\kappa_1 + \gamma_1)^2} \frac{J^2}{i(\omega - \omega_2) + \kappa_2 + \gamma_2}, \quad (3.14)$$

where the first two terms gives the point on the circle of oscillator 1, where the last term is the trajectory of second oscillator. Again by separating the real and imaginary components, we have

the I/Q expression as:

$$\begin{aligned} X' &= \frac{g^2(\gamma_2 + \kappa_2)}{(\omega - \omega_2)^2 + (\kappa_2 + \gamma_2)^2}, \\ Y' &= \frac{g^2(\omega - \omega_2)}{(\omega - \omega_2)^2 + (\kappa_2 + \gamma_2)^2}. \end{aligned} \quad (3.15)$$

It is easy to prove the following relation:

$$(X' - X'_c)^2 + Y'^2 = R'^2, \quad (3.16)$$

where $X'_c = 1 - [\kappa_1(\kappa_1 + \gamma_1) - J^2]/(\kappa_1 + \gamma_1)$ is the center and $R' = J^2/(\kappa_1 + \gamma_1)^2$ is the radius of the second circle. This formula indicates the coherent coupling induced a second circle on the I/Q trajectory, and the second circle is an incircle of the first large circle. The I/Q diagrams are given in Fig.3.5 (e), from which we can see as we are sweeping the ω_2 , the small circle moves counterclockwise along the large circle. In this case, this system would never reach zero or negative damping since the first oscillator already limits the region of the coupled curve.

On the other hand, for pure dissipative coupling (with $J = 0, \Gamma > 0$), the only difference is the coupling strength becomes purely imaginary so that we can derive the results similarly. The center of second circle and radius becomes $X' = 1 - [\kappa_1(\kappa_1 + \gamma_1) + \Gamma^2]/(\kappa_1 + \gamma_1)$ and $R' = -\Gamma^2/(\kappa_1 + \gamma_1)$. In this case, the second circle is no longer an incircle but an excircle of the first circle. This coupling regime breaks the limitation of coherent coupling and provides the opportunity to reach the singularity.

Since the coherent and dissipative coupling term can coexist in coupled metamaterial structures, the interference between coherent and dissipative coupling would be more common to be observed in real experiments.

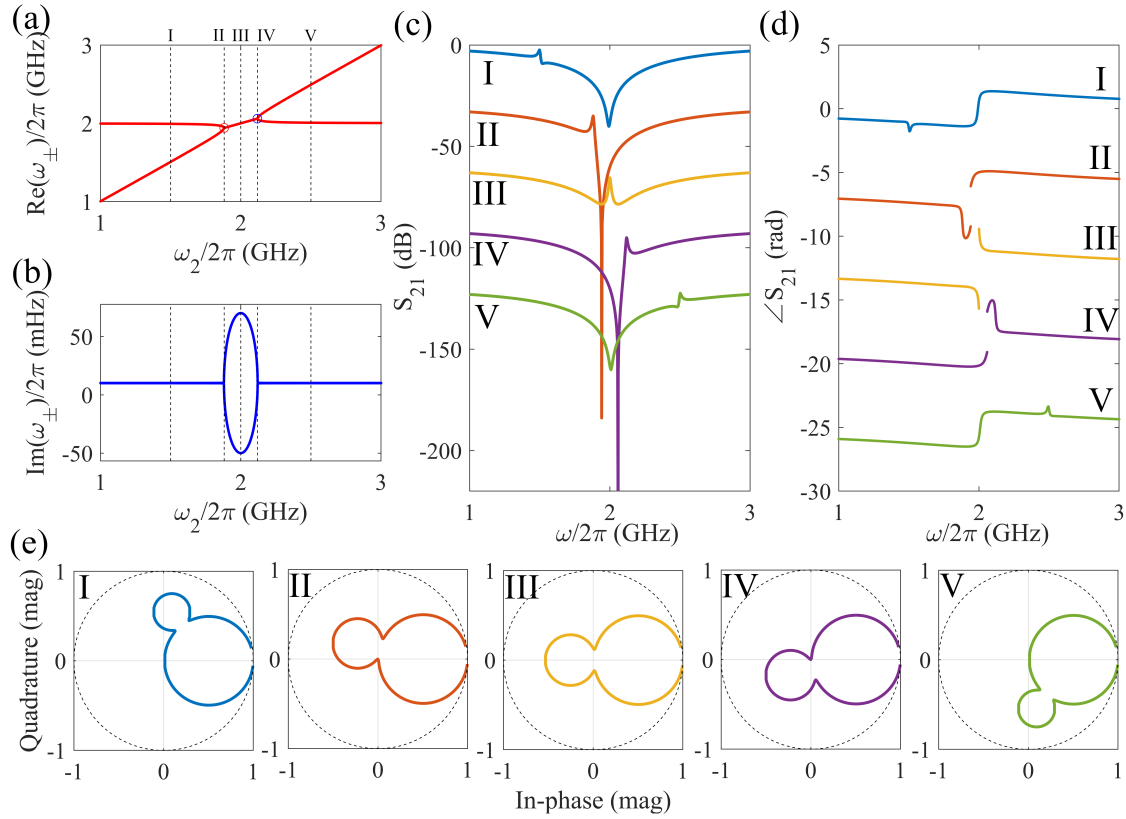


FIGURE 3.6: The I-Q analysis for dissipative coupling. (a) The calculated level repulsion dispersion. (b) The calculated linewidth exchange evolution. (c) Waterfall plot of $|S_{21}|$ amplitude in dB scale under various detunings. (d) Waterfall plot of S_{21} phase in radian. Shifts have been applied to different spectrums for clarification. (e) The I/Q diagrams under various detunings. The parameter we used for calculation is $\omega_1 = 2$ GHz, $\kappa_1 = 0.99$ GHz, $\gamma_1 = 10$ MHz, $\omega_2 = 1.3$ GHz, $\kappa_2 = 3.6$ MHz, $\gamma_2 = 6.5$ MHz, $J = 0$ MHz and $\Gamma = \sqrt{\kappa_1 \kappa_2} = 60$ MHz.

3.3 Experiment results

In this section, we present the design of the coupled metamaterial structure, where the dissipative coupling is created between a microwave cavity and an SRR. The cavity used is a Michelson-like microwave interferometer based on a microstrip cross junction[33, 100], which is fabricated with the use of two perpendicular transmission lines on a 0.813-mm-thick RO4003C substrate (with a relative permittivity of 3.38 ± 0.05). The two horizontal arms are connected to a vector network analyzer (VNA) to enable microwave-transmission measurements, while the two vertical arms are short-terminated, acting as the boundaries of the cavity. Each arm with a length of 30 mm has

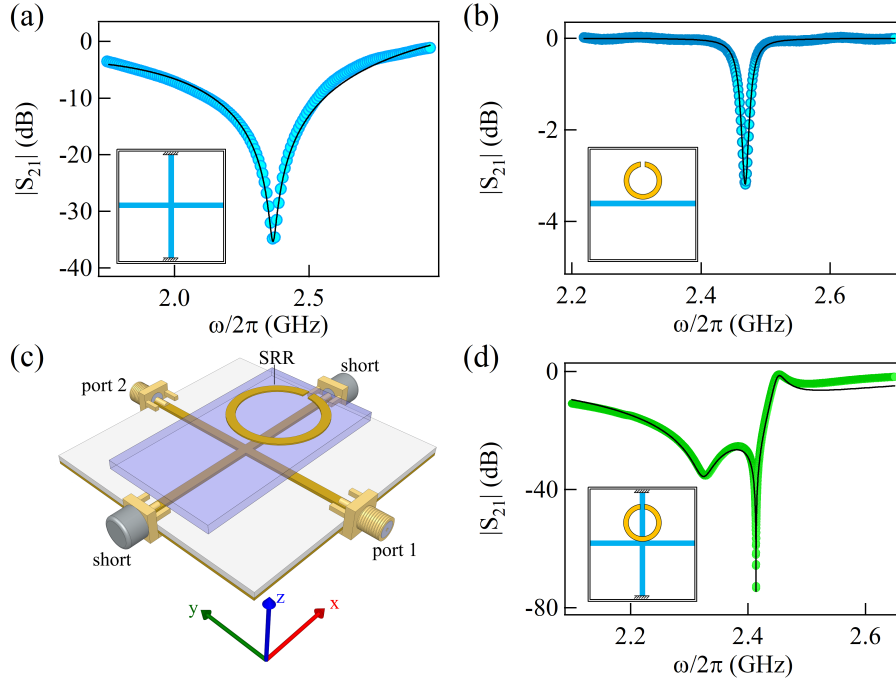


FIGURE 3.7: (a) Measured S_{21} spectrum (circles) of the bare cross-cavity and the line shape calculation (solid lines). (b) Measured S_{21} spectrum (circles) of an SRR with a radius of 8.5 mm excited through a standard 50Ω transmission line and the line shape calculation (solid lines). (c) Schematic picture of the coupled metamaterial structure, where a split-ring resonator (SRR) is strongly coupled with the cross-cavity. The arms in x direction of the cavity have been shorted to ground. (d) S_{21} spectrum of the coupled system by placing the SRR (face-up) on the top of the cavity as schematically shown in (b). Circles are the experimental data, and the solid line is the calculation using Eq. (3.8).

a width of 1.67 mm to achieve 50Ω characteristic impedance. A set of SRRs has fabricated on a 1.5-mm-thick RO5880 substrate with a relative permittivity of 2.20 ± 0.02 . The outer radius (R) of the SRR varies from 7.0 mm to 14.0 mm. The gap and the width of SRRs are fixed at 1.0 mm and 2.0 mm, respectively.

3.3.1 Ultra-narrow-band microwave invisibility

The performance of the cavity is first characterized with a VNA measurement [circles for S_{21} spectrum in Fig. 3.7(a)]. We can calculate the resonant features, with the resonance frequency ω_1 , intrinsic damping rate γ_1 and extrinsic damping rate κ_1 determined on a fit according to

$S_{21}(\omega) = 1 - \kappa_1/[i(\omega - \omega_1) + (\kappa_1 + \gamma_1)]$. The obtained parameters are $\omega_1/2\pi=2.36$ GHz, $\gamma_1/2\pi=11.5$ MHz and $\kappa_1/2\pi=990$ MHz.

To characterize the SRR performance, we placed it (face-up) in the vicinity of a standard $50\ \Omega$ transmission line. Following the same procedure of the VNA measurement, we have deduced the resonance parameter, for example, $\omega_2/2\pi=2.46$ GHz, $\gamma_2/2\pi=3.0$ MHz and $\kappa_2/2\pi=13.8$ MHz for an 8.5-mm-radius SRR. While the intrinsic damping rate γ_2 is almost a constant when moving the SRR away from the transmission line, κ_2 decreases due to a weaker coupling between the SRR and transmission line.

The demonstration of the dissipative effect is performed by directly placing an SRR (face-up) on the top of our cavity, and the schematic diagram of the experimental setup is shown in Fig. 3.7(c). Here, we align the gap of SRRs along the vertical arm of our cavity and fix the portion of SRRs opposite to the gap just on the top of the cross junction. This setup is the optimized configuration after careful simulations and tests. One signature of dissipative coupling is the appearance of the ultra-narrow-band microwave invisibility ($S_{21} \equiv 0$) as predicted in Sec. 3.2.3. This measurement is shown in Fig. 3.7(d), with a sharp dip decreasing from -1.5 dB at 2.453 GHz to -74.4 dB at 2.414 GHz; a seven-orders-of-magnitude deduction of microwave transmission in a frequency range less than 40 MHz. In the same frequency range, the microwave transmission only varies about 10 dB for either bare cavity mode or bare SSR mode. We can fit the line shape of this sharp resonance and thus an intrinsic damping rate of $\text{Im}(\tilde{\omega}_+)/2\pi=29$ kHz was obtained, corresponding to a two-orders-of-magnitude reduction in the linewidth of the uncoupled modes.

To validate our model, we use Eq.(3.8) to calculate the S_{21} spectrum in whole frequency range, with $\omega_1/2\pi=2.28$ GHz, $\kappa_2/2\pi=5.8$ MHz (corresponded to $\Gamma/2\pi=75.6$ MHz) and $J/2\pi=-6.5$ MHz determined on the basis of a fit to the experimental data. The slight red-shift of ω_1 is caused by the increment of the effective permittivity of the cavity structure when placing the SRR. Other used parameters are the same as the bare resonators. The resonant features are well reproduced by our model, plotted as the solid red line in Fig. 3.7(d). To further confirm that the dissipative coupling is indeed achieved in our design, we perform the following experiments to view the signature of a

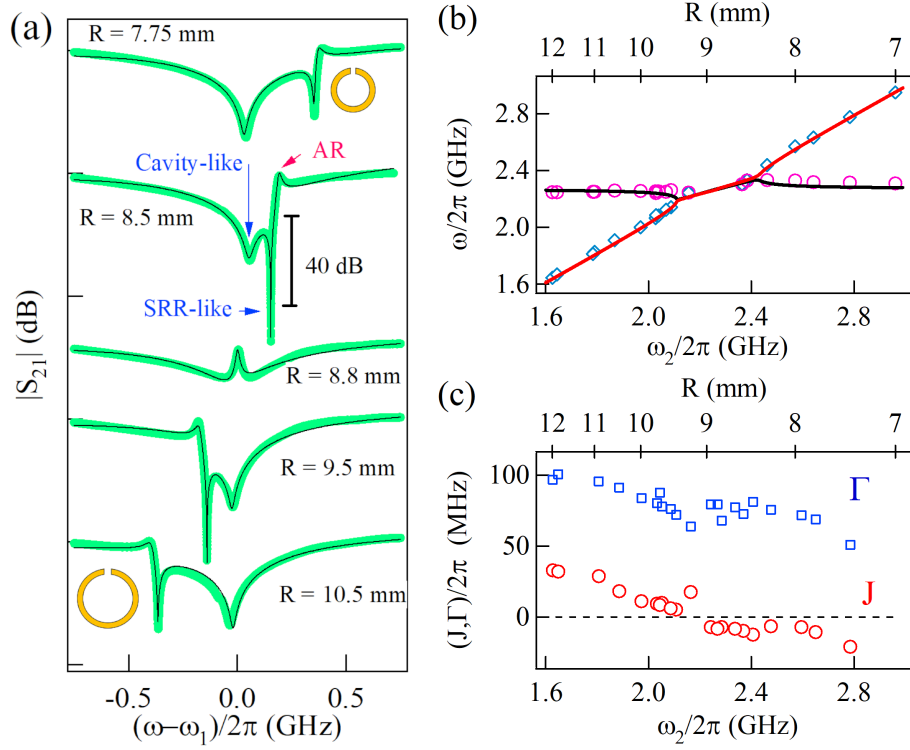


FIGURE 3.8: (a) Waterfall plot of S_{21} spectra of the coupled metamaterial structure with different SRR radius. Green circles and solid red lines represent the measured and fitted results using Eq. (3.8), respectively. (b) plots the frequencies of the hybridized modes as a function of ω_2 , where blue and purple circles represent the SRR-like and cavity-like hybrid modes. The solid line is the calculated real part of $\tilde{\omega}_\pm$ with an effective coupling constant $G/2\pi = 76i$ MHz for simplicity. (c) The deduced coupling constant J and Γ as a function of ω_2 .

dissipatively coupled metamaterial structure from other aspects.

3.3.2 Observation of level attraction

The unambiguous signature of dissipative coupling is the unique dispersion of the coupled system, which appears as level attraction in contrast to level repulsion caused by coherent coupling. In order to measure the dispersion of coupled metamaterial systems, we have fabricated a set of SRRs with different radius varying from 14.0 mm to 7.0 mm. Correspondingly, their resonant frequencies vary from 1.5 GHz to 3.0 GHz with an increment of intrinsic damping rate from 2.4 MHz to 4.3 MHz.

By coupling an individual SRR to the cross-cavity, S_{21} spectra with different frequency detuning

$(\Delta = \omega_2 - \omega_1)$ were measured, and the typical results are plotted in Fig. 3.8(a). The extracted frequencies of hybridized modes are plotted as a function of ω_2 in Fig. 3.8(b), which clearly shows the characteristic level attraction behavior. As the dispersion of the hybridized mode is governed by dissipative coupling, we can reproduce it use an effective coupling constant $G/2\pi = 76i$ MHz [solid line in Fig.3.8(b)].

A careful examination of the S_{21} spectra reveals more detailed features of dissipative coupling. For an SRR with $R = 8.80$ mm, the resonance frequency is $\omega_2/2\pi=2.27$ GHz, close to the cavity frequency $\omega_1/2\pi=2.28$ GHz; the S_{21} spectrum shows a combined resonance feature, similar to the pattern observed in coupled magnon-photon systems at a matched frequency condition.[40, 81] In addition, away from this matched condition, a small peak occurs outside of the two hybridized modes; in contrast to the peak that occurs between them in level repulsion cases. The different sequences of dips and peak in S_{21} spectra are attributed to different polarities of the transmission line shape near the SRR-like hybridized mode, which is in agreement with the theoretical and experimental works in a coupled magnon-photon system [40]. Furthermore, the linewidth of the SRR-like modes significantly shrinks, accompanied by significant suppression of microwave transmission, when it approaches the bifurcation points. This observation is similar to the case of $\Gamma = 0$ discussed in Sect. 3.2.2, but different from the experimental observation reported in a coupled magnon-photon system at $J \sim \Gamma$, where one ZDC appears in the magnon-like mode and another in photon-like mode [36].

The observed features can be well reproduced by our model [solid lines in Fig. 3.8(a)] based on Eq. (3.8), from which we obtain the complex coupling constant as a function of ω_2 [Fig. 3.8(c)]. Indeed, the dissipative coupling is the dominant mechanism in our system, with an average ratio of $|\Gamma/J| \sim 7$. Interestingly, the sign of the coherent coupling constant J changes, which can be attributed to the competition between electric coupling (M_E term) and magnetic coupling (M_H term) according to $J = (M_E\omega_1 - M_H\omega_2)/2\sqrt{L_1L_2}$. This effect further confirms the comparable amplitude between M_E and M_H in our initial design.

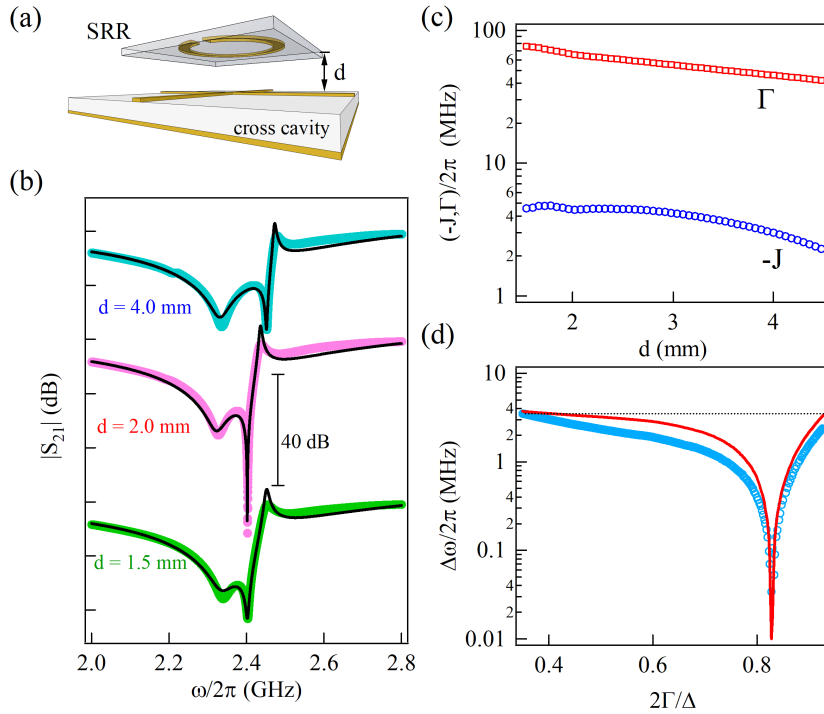


FIGURE 3.9: (a) Schematic diagram of the experimental set-up. The separation, d , between the planes of the SRR and cross-cavity was continuously tuned from 1.5 to 4.5 mm. (b) Three typical S_{21} spectra measured at $d = 1.5$, $d = 1.8$ mm and $d = 4.0$ mm. (c) The deduced coupling constant J and Γ as a function of d . (d) The deduced linewidth of the SRR-like mode as a function of the dimensionless quantity Γ/Δ . Dotted line indicates the linewidth of the uncoupled SRR.

3.3.3 Control of the Zero damping condition

To further demonstrate how dissipative coupling influences the linewidth of hybridized modes in the coupled metamaterial structure, we perform another experiment where the coupling constant G can be continuously tuned in a wide range. To do so, we use a motor-driven 3D stage with a minimum step of $5 \mu\text{m}$ to vary the separation, d , between the SRR (with a radius of 8.5 mm) and cavity, as the schematic diagram shown in Fig. 3.9(a). Figure 3.9(b) shows three typical S_{21} spectra measured at $d=1.5$ mm, 1.8 mm and 4.0 mm. It is clearly seen that the separation between the two hybridized modes increases with an increased d , which may be explained by the decrease of the dissipative coupling constant Γ . To prove it, Equation (3.8) is used to deduce the coupling constant based on the fit of the lineshape of S_{21} spectra. The extracted coupling constants J and

Γ are plotted as a function of d in Fig. 3.9(c), where the amplitude of both J and Γ reduces with the distance. While the reduction of J can be explained by the smaller field overlapping between two resonators with a larger separation, the reduction of Γ is believed due to less correlation between them in the radiative damping.

More interestingly, the linewidth of the SRR-like mode becomes extremely sharp near $d = 1.8$ mm [Fig. 3.9(b)], much narrower than that in the uncoupled SRR. We can plot the obtained linewidth (blue circles) of the SRR-like mode as a function of a dimensionless quantity, $2\Gamma/\Delta$, which relates the efficiency of how energy in a coupled system is redistributed to compensate one subsystem damping through the dissipative coupling. Two orders of magnitude reduction of the linewidth, from 3.5 MHz to 34 kHz, is observed in a very narrow range near $\Gamma/\Delta \sim 0.8$. This narrowing effect can be explained by our model [solid line in Fig. 3.9(d)] according to the calculation of $\text{Im}(\hat{\omega}_+)$ using the known parameters, clearly showing the appearance of the zero-damping rate.

3.3.4 Voltage controlled level attraction

Based on previous experiments involving a manual way to study the coupling phenomenon in meta-material structures, we now integrate active components into the coupled system and implement a planar device to achieve electric control of level attraction. Figure 3.10(a) shows the schematic diagram for this improved design, a varactor-loaded SRR with a radius of 12.0 mm. The varactor loaded in the SRR acts as a voltage-controlled capacitor, and hence, the resonance frequency of the SRR can be changed by varying the bias dc voltage. We first characterized the varactor-loaded SRR excited by a standard $50\ \Omega$ transmission line. The frequency of this SRR can be tuned between 1.8 GHz and 2.5 GHz, as shown in Fig. 3.10(b), corresponding to a bias voltage of -0.5 V and 21 V. Because of additional losses caused by the varactor, the intrinsic damping rate of this active SRR is much higher than the passive SRR, varying in a range between $\gamma_2/2\pi \sim 18$ MHz and $\gamma_2/2\pi \sim 36$ MHz and strongly dependent on the biased voltage.

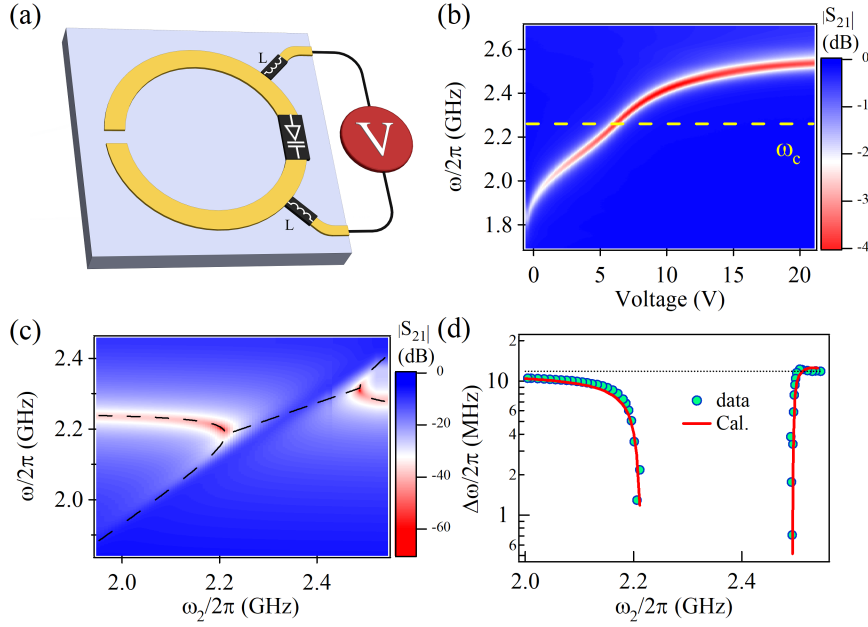


FIGURE 3.10: (a) The design of a frequency tunable SRR by integrating a varactor biased by a dc voltage. Two RF chokers were used to isolate the microwave signal. (b) The microwave transmission mapping for the tunable SRR excited by a standard $50\ \Omega$ transmission line. The white dashed line represents the frequency of the uncoupled cross-cavity mode, $\omega/2\pi = 2.25$ GHz. (c) Experimental S_{21} spectra mapping as a function of ω and ω_2 . Black dashed lines are the calculated dispersion using the complex coupling constant $G/2\pi = 69i$ MHz. (d) The linewidth of the cavity-like hybridized mode is plotted as a function of ω_2 . The solid red line indicates the calculation result.

Dotted line indicates the linewidth of the bare cavity.

Then, we combined this varactor-loaded SRR with our cross-cavity according to the same orientation of previous measurements, building a planar device. By continuously tuning the biased dc voltage, the measured S_{21} mapping [Fig. 3.10(c)] was obtained, showing level attraction between the cavity mode and SRR mode. As the dissipative coupling is the dominated coupling mechanism, for simplicity, a pure imaginary coupling constant $G/2\pi = 69i$ MHz is used to calculate the dispersion of the hybridized modes [dashed lines in Fig. 3.10(c)].

Since the varactor-loaded SRR has a higher damping rate than the cross-cavity, the linewidth-narrowing effect occurs at the cavity-like hybridized mode. Figure 3.10(d) shows the extracted linewidths of the cavity-like hybrid mode as a function of ω_2 . It is clearly seen that the linewidth dives sharply when ω_2 approaching the bifurcation points. This behavior is in agreement with

the discussion in Sec.3.3.2 for the case of $J = 0$. We can also make a quantitative comparison with our model by calculating the imaginary part of ω_{\pm} (solid red line), which well reproduces the experimental observation.

3.4 Summary

In summary, we have demonstrated level attraction due to dissipative coupling in a coupled metamaterial structure, both theory and experiment. We also predict the appearance of a zero damping rate in a coupled system involved dissipative coupling, which was unambiguously confirmed by our experiment. Such a striking effect breaks the previous limitation for implementing a sharp transmission/reflection transition, which currently supports the concepts of many switching devices in microwaves and optics. In the end, we fabricated a planar coupling device with a capability of electrically controlled level attraction and linewidth narrowing, clearly demonstrate the potential for controlling and utilize electric and magnetic interaction between different metamaterial elements in the modern microwave and optical technologies.

Chapter 4

Dissipatively coupled magnon-photon system for broadband nonreciprocal devices

4.1 Introduction

In quantum information processing, the fast readout of the long lifetime qubit requires delicate isolation and shielding between the qubit and circuit [101–104]. This remains a great challenge [11, 54, 104–107] because even a tiny amount of energy leakage would destroy the sensitive quantum state [101]. For example, even 0.1% percent of the energy (60 dB) leak into a low Q mode would completely spoil its lifetime. Given this fact, nonreciprocal devices [108] which can unidirectionally shield qubits are indispensable and in high demand. Several mechanisms have been put forward to produce the nonreciprocity with high isolation ratios, such as the Faraday rotation [109], reservoir engineering [80, 110], optomechanical interactions[111, 112], active dynamics [113] and chiral mode [114]. Very recently, a novel approach has been demonstrated [36] in cavity magnon polaritions [1, 10, 13, 16, 45, 81, 115–121] by manipulating the interference between coherent [10, 12, 16, 122–125] and dissipative [31–33, 35, 40, 81, 126–128] couplings. Unlike previous methods, infinite isolation in such a cavity magnonic device is theoretically achievable, which makes it ideally suitable for protecting sensitive quantum states.

Specifically, dissipative coupling in the cavity magnonic device allows for creating two zero

damping conditions (ZDCs) [36, 98], at which a hybridized mode with zero intrinsic damping is produced, corresponding to complete blocking of microwave transmission. Because the interference term between the coherent and dissipative couplings changes sign in the forward and backward transmission cases [36], two ZDCs in the forward transmission are staggered with those in the backward transmission in the frequency domain. As a consequence, the giant nonreciprocity occurs when the magnon mode frequency approaches these four ZDCs.

While the isolation ratio in these nonreciprocal devices can be theoretically infinity, the operating bandwidth for the giant nonreciprocity is limited by the resonance linewidth. From the practical application perspective, a nonreciprocal device that possesses both the infinite isolation and wideband operation is much more desirable than those with infinity isolation only at four single frequencies. To achieve such a goal, we propose a method to broaden the effective nonreciprocal bandwidth of a cavity magnonics device. Experimentally, a small loop antenna is integrated to control the radiative damping of the magnon mode [41]. As a result, our device's side ZDCs can be consecutively tuned in a wide frequency range, a few hundred times broader than the linewidth of the magnon mode. By means of this method, the effective bandwidth of the giant nonreciprocity at the side ZDCs is broadened up to approximately 200 MHz. Our work demonstrates a feasible technical solution to broaden the bandwidth of the giant nonreciprocal device based on cavity magnonics, which may benefit the design of practically nonreciprocal devices for future quantum technology.

4.2 Theory

4.2.1 Effective Hamiltonian of our cavity magnonic device

The schematic diagram of the interactions between a cavity photon mode (ω_c) and a magnon mode (ω_m) was shown in Figure 4.1(a). Both of them are side-coupled to an impedance-matched transmission line. κ and γ respectively represent their extrinsic dampings due to the coupling with the transmission line. Because of the correlation of these two radiative dampings, an indirect

coupling effect is produced between two modes with a strength of $i\Gamma = i\sqrt{\kappa\gamma}$. Notice that the coupling strength is imaginary, which indicates that such an indirect coupling is purely dissipative. Besides, due to the direct mode overlap, a coherent coupling effect with a J strength also exists. β and α represent the intrinsic damping rates of the cavity photon mode and the magnon mode, which have no noticeable effect on the interactions between two modes. A loop antenna is placed close to the magnon mode to introduce an additional radiation damping rate of the magnon mode (γ_L).

To model the dynamics of our cavity magnonic device that involves dissipative coupling shown in Fig. 4.1 (a), an effective Hamiltonian is constructed according to the Ref. [36]:

$$\hat{H}_e/\hbar = \tilde{\omega}_c \hat{a}^\dagger \hat{a} + \tilde{\omega}_m \hat{b}^\dagger \hat{b} + (J - ie^{i\Theta_{1(2)}}\Gamma)(\hat{a}^\dagger \hat{b} + \hat{a} \hat{b}^\dagger), \quad (4.1)$$

where \hat{a} (\hat{a}^\dagger) and \hat{b} (\hat{b}^\dagger) respectively represent the annihilation (creation) operators of the cavity photon and magnon modes. $\Theta_{1(2)}$ is 0 or π for microwave signals loaded from port 1 or 2.

In the absence of external driving sources, according to the Eq. (4.1), two coupled modes evolve in time can be derived as:

$$\frac{d}{dt} \begin{bmatrix} \hat{a} \\ \hat{b} \end{bmatrix} = -i \begin{bmatrix} \tilde{\omega}_c & J - i\Gamma e^{i\Theta_{1(2)}} \\ J - i\Gamma e^{i\Theta_{1(2)}} & \tilde{\omega}_m \end{bmatrix} \begin{bmatrix} \hat{a} \\ \hat{b} \end{bmatrix}. \quad (4.2)$$

From this dynamic equation, the dispersions of two hybridized modes can be obtained as $\tilde{\omega}_\pm = (\tilde{\omega}_c + \tilde{\omega}_m \pm \sqrt{(\tilde{\omega}_c - \tilde{\omega}_m)^2 + 4(J - i\Gamma e^{i\Theta_{1(2)}})^2})/2$. At two specific detunings (Δ_m), the hybridized mode with zero intrinsic damping rate occurs, because of the dissipative coupling effect. These two detunings are the so-called zero damping conditions, which can be obtained by setting $\text{Im}(\tilde{\omega}_\pm) = 0$:

$$\Delta_m = \frac{(\beta - \alpha')J\Gamma e^{i\Theta_{1(2)}} \pm (\alpha' + \beta)\sqrt{J^2\Gamma^2 + \alpha'\beta(J^2 - \Gamma^2 + \alpha'\beta)}}{\alpha'\beta}, \quad (4.3)$$

where $\alpha' = \alpha + \gamma + \gamma_L$ is the total damping rate of the magnon mode. From $\text{Im}(\tilde{\omega}_\pm) = 0$, the

mathematical expressions of two ZDCs can be approximated to first order Taylor series. The detailed process is given in Appendix A.2. If we have $J^2\Gamma^2 \gg \alpha'\beta(J^2 - \Gamma^2 + \alpha'\beta)$, a concise form of these two ZDCs can be obtained by using the first-order approximation of the square root term as follow:

$$\begin{aligned}\Delta_{ce} &= -\frac{2J\Gamma e^{i\Theta_{1(2)}}}{\beta} + \frac{(\alpha' + \beta)(J^2 - \Gamma^2 + \alpha'\beta)}{2J\Gamma e^{i\Theta_{1(2)}}} \\ \Delta_{si} &= \frac{2J\Gamma e^{i\Theta_{1(2)}}}{\alpha'} - \frac{(\alpha' + \beta)(J^2 - \Gamma^2 + \alpha'\beta)}{2J\Gamma e^{i\Theta_{1(2)}}},\end{aligned}\quad (4.4)$$

where $\Delta_{ce} = \omega_{m,ce} - \omega_c$ and $\Delta_{si} = \omega_{m,si} - \omega_c$ are the central and side ZDCs, since $|\Delta_{ce}| < |\Delta_{si}|$ for our device. $\omega_{m,ce}$ and $\omega_{m,si}$ are the magnon mode frequencies that allow the center and side ZDCs to occur, respectively. When the signal is respectively loaded from port 1 ($\Theta_1 = 0$) and port 2 ($\Theta_2 = \pi$), two ZDCs exist in either transmission case, i.e., there exist four ZDCs in total. When the magnon mode frequency (ω_m) approaches each of them, the input signal is completely blocked in one transmission direction but can freely propagate through the device in the other transmission direction. In another word, the giant non-reciprocity occurs. Since the central ZDCs are closer to the cavity photon mode than the side ZDCs, the giant non-reciprocity at the central ZDC inevitably has a larger insertion loss than that at the side ZDC [36]. Therefore, the giant non-reciprocity at the side ZDC has greater potential in the practical applications.

4.2.2 Transmission spectrum of dissipative magnonic device

When the microwave signal is loaded from port 1 or 2, the dynamics of our magnonic device is governed by the quantum Langevin equation [129]:

$$\frac{d}{dt} \begin{bmatrix} \hat{a} \\ \hat{b} \end{bmatrix} = -i \begin{bmatrix} \tilde{\omega}_c - i\kappa & J - i\Gamma e^{i\Theta_{1(2)}} \\ J - i\Gamma e^{i\Theta_{1(2)}} & \tilde{\omega}_m \end{bmatrix} \begin{bmatrix} \hat{a} \\ \hat{b} \end{bmatrix} + \begin{bmatrix} \sqrt{\kappa} \\ \sqrt{\gamma} \end{bmatrix} \hat{p}_{1(2)}^{in}. \quad (4.5)$$

where $\hat{p}_{1(2)}^{in}$ represents the input signal from port 1 or 2, which simultaneously drives the cavity photon mode (\hat{a}) and the magnon mode (\hat{b}). Because of $\kappa \gg \gamma$, the drive applied to the magnon

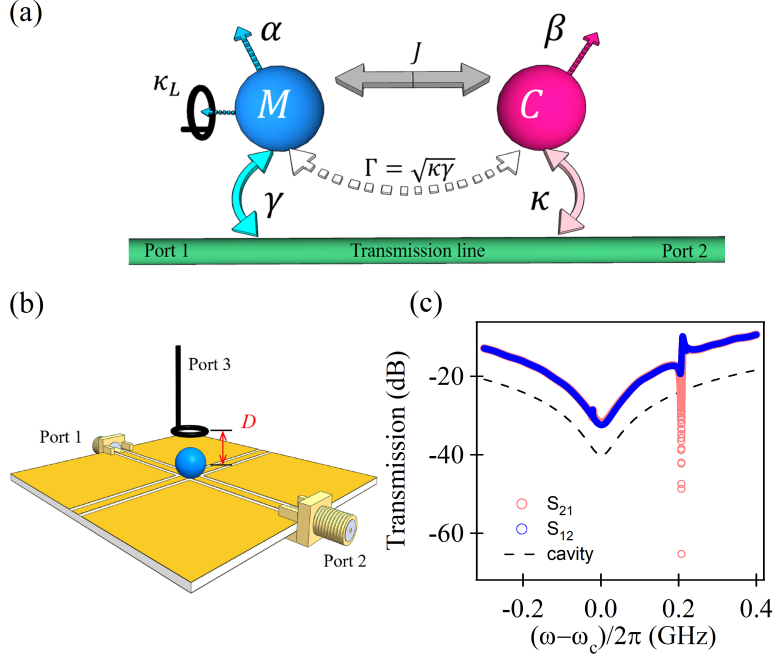


FIGURE 4.1: (a) Schematic diagram of the interactions between a magnon mode and a cavity mode. A loop antenna is placed close to the magnon mode to control its radiation damping. (b) Schematic picture of our device. A YIG sphere is placed on the intersection of the cross cavity. The separation distance *D* between it and the loop antenna is tunable. (c) Comparison of the forward and backward transmission spectra ($|S_{21}|$ and $|S_{12}|$) measured at the side ZDC. Black dashed line indicates the measured transmission spectrum of the empty cavity, which is shifted by -10 dB for the sake of clarity.

mode, i.e., $\sqrt{\gamma}\hat{p}_{1(2)}^{in}$ can be neglected. For the same reason, the input-output relation of our device can be simplified to $\hat{p}_{2(1)}^{out} = \hat{p}_{1(2)}^{in} - \sqrt{\kappa}\hat{a}$, and the transmission spectrum can be derived as $S_{21(12)} = \langle \hat{p}_{2(1)}^{out} \rangle / \langle \hat{p}_{1(2)}^{in} \rangle$. From the effective non-Hermitian Hamiltonian has been constructed (Eq.4.1), the transmission spectrum of system in the forward and backward directions can be derived as:

$$S_{21(12)} = 1 + \frac{\kappa}{i(\omega - \omega_c) - \kappa - \beta + \frac{(J - i\Gamma e^{i\Theta_{1(2)}})^2}{i(\omega - \omega_m) - \alpha'}}, \quad (4.6)$$

where $\Theta_{1(2)}$ is used to indicate the different interference behaviours between two types of coupling effects, which can respectively be 0 and π for microwave signals loaded from port 1 and port 2. α' represents the total damping rate of the magnon mode, which includes the Gilbert damping

(α) , the radiation damping into the transmission line (γ) and the radiation damping into the loop antenna (γ_L). The complex frequencies of two hybrid modes of the system can be solved as $\tilde{\omega}_{\pm} = (\tilde{\omega}_c + \tilde{\omega}_m \pm \sqrt{(\tilde{\omega}_c - \tilde{\omega}_m)^2 + 4(J - i\Gamma e^{i\Theta_{1(2)}})^2})/2$, where $\tilde{\omega}_c = \omega_c - i\beta$ and $\tilde{\omega}_m = \omega_m - i\alpha'$ are the complex frequencies of the cavity photon and magnon modes.

4.2.3 Reflection spectrum measured from the loop antenna

In our experimental set-up, the loop antenna can be viewed as an additional port of the magnon mode. The radiation damping rate (γ_L) of the magnon mode induced by the loop antenna can be characterized by measuring the reflection spectrum (S_{33}). When the magnon mode frequency is tuned away from the cavity photon mode (i.e., $|\Delta_m| \gg |J - i\Gamma e^{i\Theta_{1(2)}}|$), the influence from the cavity photon mode on the magnon mode can be neglected. Therefore, the dynamics of the magnon mode can be simply described by the Hamiltonian of $\hat{H}_m/\hbar = [\omega_m - i(\alpha + \gamma)]\hat{b}^\dagger\hat{b}$. From it, the quantum Langevin equation of the magnon mode is:

$$\frac{d\hat{b}}{dt} = -i[\omega_m - i(\alpha + \gamma)]\hat{b} - \frac{\gamma'}{2}\hat{b} + \sqrt{\gamma'}\hat{p}^{in}, \quad (4.7)$$

where the γ' is the coupling strength between the magnon mode and the external photon bath. The radiation damping rate of the magnon mode induced by the loop antenna is $\gamma_L = \gamma'/2$. Adopting the input-output relation $\hat{p}^{out} = \hat{p}^{out} - \sqrt{\gamma'}\hat{b}$, the reflection spectrum of the magnon mode is derived as:

$$S_{33} = 1 - \frac{\gamma'}{i(\omega_m - \omega) + (\alpha + \gamma + \gamma_L)}. \quad (4.8)$$

Therefore, by measuring the reflection spectrum from loop antenna, we can extract the radiation damping of the magnon.

4.2.4 The classical microwave circuit model for dissipative coupling

Since our device works in a linear dynamic regime, besides the aforementioned quantum model, the coupling effects can also be described by an equivalent LCR circuit model. The coherent coupling effect between the cavity mode and the magnon mode can be described as a mutual capacitance and a mutual inductance of two LCR resonators, which have been well studied in previous works [26, 27, 95]. Herein, we only focus on the dissipative coupling effect in cavity magnonics. As shown in Fig.4.2, the cavity mode and the magnon mode are respectively represented by two series RLC resonators. $R_c(m)$, $C_c(m)$ and $L_c(m)$ are the equivalent resistance, capacitance and inductance of the cavity (magnon) mode. Two resonators are connected to a common transmission line with a characteristic impedance of Z_0 . l is the separation of two resonators, and k is the wavevector of traveling waves in the transmission line.

The scattering properties of this circuit can be described by cascade matrices of the cavity mode, transmission line and magnon mode, i.e., M_c , M_L and M_m . The system transfer (ABCD) matrix of the whole circuit can be obtained by simply multiply these three transmission matrices [95]:

$$\begin{bmatrix} A & B \\ C & D \end{bmatrix} = M_c M_l M_m = \begin{bmatrix} 1 & 0 \\ 1/Z_c & 1 \end{bmatrix} \begin{bmatrix} \cos(kl) & -iZ_0 \sin(kl) \\ -iZ_0^{-1} \sin(kl) & \cos(kl) \end{bmatrix} \begin{bmatrix} 1 & 0 \\ 1/Z_m & 1 \end{bmatrix} \quad (4.9)$$

where $Z_{c(m)}$ is the impedance of the equivalent series resonator of the cavity (or magnon) mode, which has a form of $Z_{c(m)} = -i\frac{L_{c(m)}}{\omega}(\omega^2 - \omega_{c(m)}^2 + i2\omega\frac{R_{c(m)}}{2L_{c(m)}})$. $\omega_{c(m)} = 1/\sqrt{L_{c(m)}C_{c(m)}}$ is the mode frequency of the cavity (magnon). $R_{c(m)}/2L_{c(m)}$ represents the intrinsic damping rate of the cavity (magnon), i.e., $\beta(\alpha)$ in Eq. 4.6.

From the ABCD matrix, the transmission spectrum of the circuit can be derived as:

$$\begin{aligned} S_{21} &= \frac{2}{A + B/Z_0 + CZ_0 + D} \\ &= 1 + \frac{i\omega(-2\kappa - 2\gamma e^{ikl} \frac{(\omega^2 - \omega_1^2 + 2i\omega\beta) + 2i\omega\beta}{(\omega^2 - \omega_2^2 + 2i\omega\alpha) + 2i\omega\gamma}) + (e^{ikl} - 1)(\omega^2 - \omega_1^2 - 2i\omega\beta e^{ikl})}{(\omega^2 - \omega_1^2 + 2i\omega\beta) + 2i\omega\kappa + \frac{e^{i(2kl+\pi)} 4\omega^2 \kappa \gamma}{(\omega^2 - \omega_2^2 + 2i\omega\alpha) + 2i\omega\gamma}} \end{aligned} \quad (4.10)$$

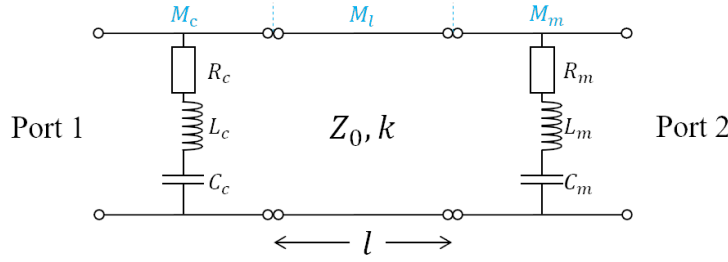


FIGURE 4.2: The schematic of classical circuit model.

where $\kappa = Z_0/4L_c$ and $\gamma = Z_0/4L_m$ are extrinsic damping rates of the cavity mode and magnon mode, respectively. Since $\kappa \gg \gamma$, we have neglected the weak drive term on the magnon-like resonator (second term on numerator on Eq.4.10). The concise form shown as Eq.4.11:

$$S_{21} \approx 1 + \frac{\kappa}{i(\omega - \omega_1) - (\beta + \kappa) + \frac{\kappa\gamma e^{i(2kl+\pi)}}{i(\omega - \omega_m) + \alpha + \gamma}} \quad (4.11)$$

Comparing it with Eq.4.6 in the quantum picture, because of the cooperative effect between these two extrinsic damping rates, an indirect coupling effect with a strength of $\sqrt{\kappa\gamma e^{i(2kl+\pi)}}$ is produced. In the experiment, the YIG sphere is placed at the intersection of the cross cavity, so that $l = 0$ and the indirect coupling strength is purely imaginary, indicating that the indirect coupling effect is dissipative.

This equivalent LCR circuit model offers a classical explanation for the indirect dissipative coupling in our cavity magnonic device. As all its ingredients (including capacitors, inductors, resistors and transmission line) are reciprocal devices, the transmission parameter of this circuit is also reciprocal. To further describe the nonreciprocity in our device, one has to modify the equivalent RLC circuit of the YIG sphere by considering both the mode profile and the magnetization precession according to the Landau-Lifshitz equation.

4.3 Experiment

Our experimental set-up is shown in Fig. 4.1 (b), which consists of three main parts: a planar cross cavity, a yttrium iron garnet (YIG) sphere and a loop antenna. The planar cross cavity is fabricated on the RO4350BTM substrate with a thickness of 0.85 mm. It is an open system and can sustain both the traveling and standing waves (cavity modes). A YIG sphere with a diameter of 1 mm is placed on the intersection of the cross to produce the coupling effects with the cross cavity. The external magnetic field produced by an electromagnet is vertically applied to saturate the magnetization of the YIG sphere and linearly controls the magnon mode frequency ω_m . To achieve a strong coupling effect, the uniform Kittel mode of the YIG sphere is chosen, which entails a significant net magnetic dipole moment [11]. Above the sphere, a loop antenna is used to introduce the additional radiation damping of the magnon mode (γ_L). The loop antenna is fixed on a motor stage and can be vertically moved in a range of 0.5 – 6.5 mm. Because the side ZDC of our device is sensitive to the damping rate of the magnon mode (α' in Eq. (4.4)), even a small perturbation from the loop antenna can result in an evident frequency shift of the side ZDC.

According to Eq. (4.4), both the central and side ZDCs show high tunability. Beside two coupling strengths (J and Γ), they can also be tuned by their changing damping rates (β and α'). By means of this property, we design an experiment to demonstrate the controllability of the side ZDC by using a loop antenna. As a consequence, the giant nonreciprocity with an effectively broad bandwidth is achieved at the side ZDCs.

Firstly, we characterized the giant nonreciprocity at the side ZDC. Fig. 4.1 (c) shows the measured results. The cavity mode occurs at $\omega_c/2\pi = 5.8$ GHz, shown as the black dashed line. From the curve fitting, its intrinsic and extrinsic damping rates are extracted as $\beta/2\pi = 32.6$ MHz and $\kappa/2\pi = 1.3$ GHz. Setting the external magnetic field at 233 mT to make the detuning equal to Δ_{si} , the side ZDC for the forward transmission (S_{21}) is satisfied. Besides the cavity-like hybrid mode near ω_c , an ultra-sharp dip (magnon-like mode) occurs at $\omega_+/2\pi = \omega_c/2\pi + 0.2$ GHz, which indicates the input signal is nearly completely blocked (red circles in Fig. 4.1 (c)). However, for the

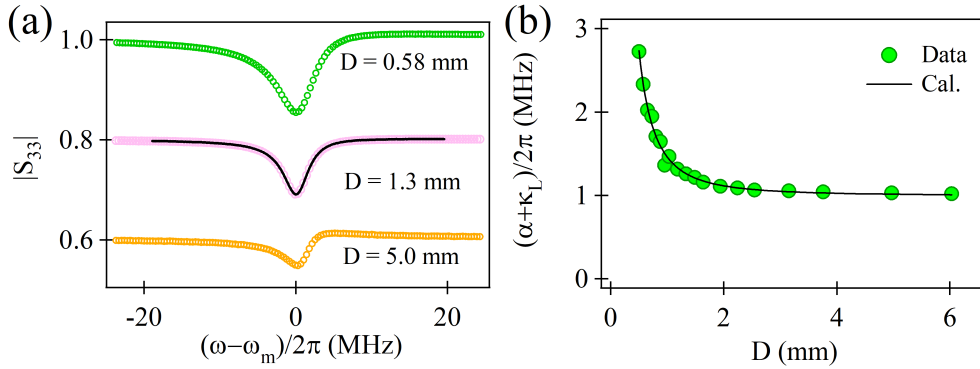


FIGURE 4.3: (a) Three reflection spectra measured from the loop antenna at the separations of 0.58, 1.3 and 5.5 mm. Reflection spectra measured at 1.3 and 5 mm have been downwards shifted by 0.2 and 0.4, respectively. The solid black line is the calculation result by using Eq. (4.8). (b) Damping rates of the magnon mode fitted from (a), which exhibits an inverse square dependence on the separation (\$D\$). The solid black line is a \$D^{-2}\$ curve to guide the eyes.

backward transmission (\$S_{12}\$) at the same magnetic field, the side ZDC is unsatisfied since the phase change of dissipative coupling term, so that a small resonant dip occurs, instead of the ultra-sharp dip. The giant non-reciprocity occurs at \$\omega = \omega_+\$, whose isolation rate (Iso. = \$20 \log_{10}(S_{21}/S_{12})\$) is more than 50 dB.

4.3.1 Locally control of the magnon damping by inducing a loop antenna

The loop antenna in our device works like a port locally coupled to the magnon mode, which offers the magnon mode an additional dissipation channel. This additional dissipation (\$\gamma_L\$) strongly depends on the separation between the loop antenna and the YIG sphere. To obtain a quantitative dependence on the separation (\$D\$), we performed another measurement to detect the reflection spectrum of the magnon mode from the loop antenna, i.e., \$S_{33}\$. Figure 4.3 (a) shows three typical reflection spectra measured at different separations. The resonant dip represents the magnon mode of the YIG sphere, which exhibits an evident dependence on the separation. By curve fitting using Eq. (4.8) the measured reflection spectra, the total damping rate, including the Gilbert damping (\$\alpha\$) and the radiation damping rate induced by the loop antenna (\$\gamma_L\$), are plotted in Fig. 4.3 (b), which exhibits an inverse square dependence on the separation (\$D\$), i.e., \$\alpha + \gamma_L \propto D^{-2}\$. Approximately, the

YIG sphere can be viewed as a point source. With the increase of the separation, the solid angle of the loop antenna relative to the YIG sphere decreases at an inverse square dependence[130], which results in the D^{-2} variation of the γ_L .

By utilizing this magnetic loop controlled magnon damping, we demonstrate a giant nonreciprocity in a wide frequency range. Figure 4.4 shows the measurement results. In the beginning, the loop antenna is placed above the YIG sphere with a separation of 0.55 mm. Forward transmission spectra (S_{21}) are measured and plotted as a function of the frequency $((\omega - \omega_c)/2\pi)$ and external magnetic field in Fig. 4.4 (a). Two sharp resonances occur at (-67.9 MHz, 222 mT) and (178 MHz, 232 mT), which correspond to the ultra-sharp modes at the central and side ZDCs, respectively. The measured dispersions of two hybrid modes in our device are plotted in the middle panel between Fig. 4.4 (a) and (b), from which two coupling strengths between the cavity mode and magnon mode are fitted as $J/2\pi = 6.5$ MHz and $\Gamma/2\pi = 29$ MHz. Since the dissipative coupling effect is more dominant than the coherent coupling, i.e., $|\Gamma| > |J|$, the dispersions of two hybrid modes exhibit as a typical level attraction. ZDCs are marked in this plane by the black solid and yellow hollow circles, respectively.

For comparison, we also measured the forward transmission spectra at the loop antenna separated from the YIG sphere with a distance of 6.1 mm (Fig. 4.4 (b)). In this case, the dispersions of two hybrid modes keep the same with the former case, which indicates the loop antenna has an ignorable effect on the coupling effects between the cavity photon mode and the magnon mode. The central ZDC of our device shows neglectable change at (-67.2 MHz, 222 mT), but the side ZDC is obviously shifted from (178 MHz, 232 mT) to (305 MHz, 237 mT). The linewidth of two hybrid modes in both cases is extracted from measured transmission spectra and plotted in Fig. 4.4 (c) and (d). Two ZDCs can be observed at the magnon-like modes. The comparison between the two cases clearly shows the influence of the loop antenna on the side ZDC. Black solid lines are calculated imaginary parts of $\tilde{\omega}_\pm$, which can well describe our experimental results.

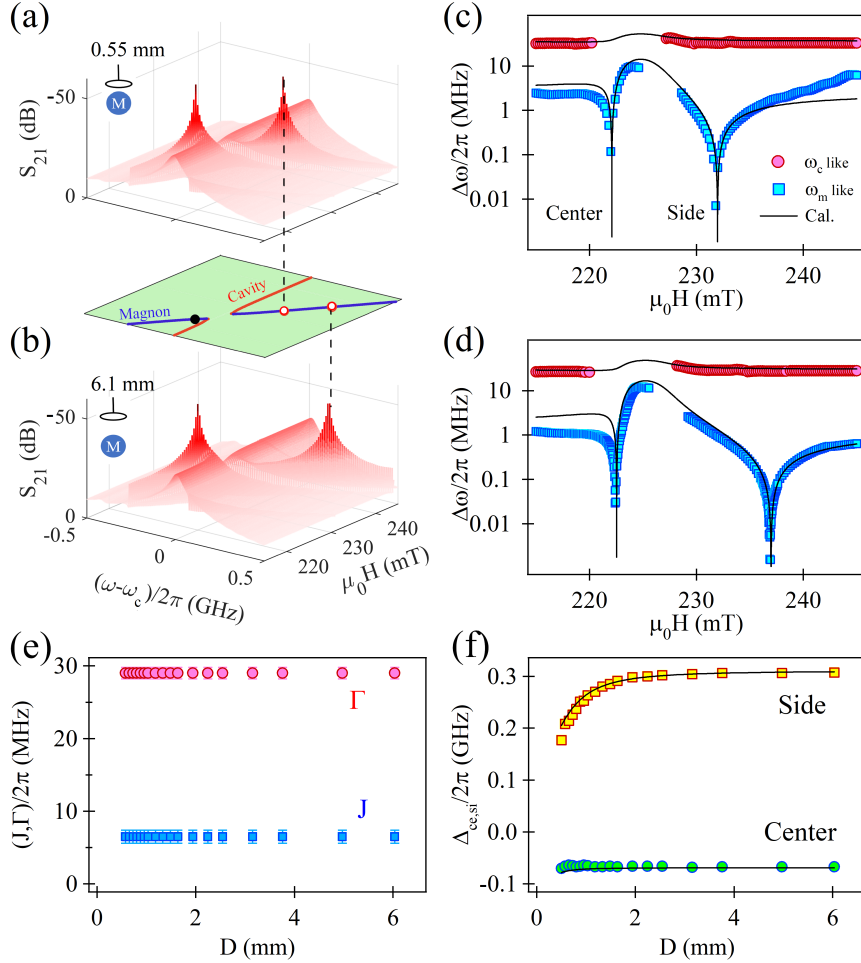


FIGURE 4.4: (a) and (b) Measured forward transmission spectra are plotted as a function of the detuning $((\omega - \omega_c)/2\pi)$ and the external magnetic field. For the sake of clarity, the z-axis of two 3-D plots has been reversed. Two sharp resonances indicate the ultra-sharp modes occur at ZDCs. Two inserts depict the separations between the loop antenna and the YIG sphere during the measurement. The middle panel shows the dispersions of two hybridized modes in our cavity magnonics device. Blue and red solid lines respectively represent the magnon- and cavity-like hybridized modes. The black circle indicates the central ZDC, which stays the same in two different measurements. Yellow hollow circles indicate the side ZDC, which can be shifted by the loop antenna. (c) and (d) Linewidths of two hybridized modes fitted from the measured transmission spectra. Blue and red dots represent the linewidths of the magnon- and cavity-like hybridized modes, respectively. Solid lines are calculated $|\text{Im}(\tilde{\omega}_\pm)|$, which are the intrinsic damping rates of two hybridized modes. (e) Coherent (J) and dissipative (Γ) coupling strengths at different separations (D) are extracted from measured dispersions of two hybridized modes, which are independent of D . (f) Two ZDCs as a function of D . Dots and black solid lines indicate the experimental data and calculation results by using Eq. (4.4).

4.3.2 Enhancement of effective bandwidth

At each separation of the loop antenna, the forward transmission spectra (S_{21}) are measured, from which coupling strengths (Γ and J) and two ZDCs ($\Delta_{ce,si}$) are extracted and plotted in Fig. 4.4 (e) and (f). Consistent with the results shown in Fig. 4.3, coupling strengths keep constant while moving the loop antenna. The central ZDC ($\Delta_{ce}/2\pi$) also stays constant, but the side ZDC ($\Delta_{si}/2\pi$) can be consecutively tuned from 150 MHz to 300 MHz. The solid black lines in Fig. 4.4 (f) are the calculated results using the Eq. (4.4) considering the dependence of γ_L , which describe the variation of two ZDCs very well. These results indicate that the loop antenna only has a significant influence on the magnon mode's damping rate, but has a neglectable effect on the cavity photon mode.

In the following experiment, we would demonstrate how to achieve an effective broadband giant-nonreciprocity in a cavity magnonic device by shifting the side ZDCs. Figure 4.5 (a) shows the measured isolation ratio of our device at $D = 0.55$ mm. Four sharp peaks in the 3-D plot indicate the giant nonreciprocity at four ZDCs. For each isolation peak, the effective bandwidth of the nonreciprocity with isolation ratio greater than 20 dB is only 2 MHz, limiting the practical use of our nonreciprocal device. As we demonstrated above, two side ZDCs can be shifted by the loop antenna in a wide range, so that the corresponding nonreciprocity at these two side ZDCs are tunable. As an example, we have chosen the side ZDC at (178 MHz, 232 mT) in Fig. 4.5 (a), and measured the frequency shift of the isolation peak [Fig. 4.5 (b)]. When increasing the separation D from 0.5 to 5.5 mm, the isolation peak is shifted to a higher frequency with an amount of 150 MHz. It indicates the giant nonreciprocity is achievable in this tunable frequency range, as long as the separation D and magnetic fields are matched. Considering the cavity mode frequency is 5.8 GHz, the effective band of the giant nonreciprocity is from 5.95 GHz to 6.15 GHz [Fig. 4.5 (c)]. Besides the side ZDC at the higher frequency than the cavity mode frequency, the side ZDC at the lower frequency (-178 MHz, 219 mT) can also produce another giant nonreciprocity band (about 150 MHz) during tuning the separation of the loop antenna (not shown in the figure).

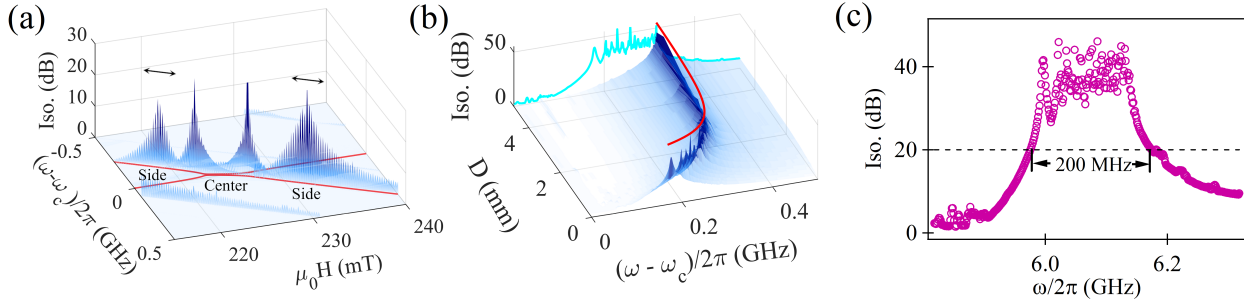


FIGURE 4.5: (a) Isolation rate (Iso.) of our device measured at $D = 0.55$ mm. Red solid lines indicate the calculated dispersions of two hybridized modes. (b) Isolation peak at the side ZDC at a higher frequency than the cavity mode frequency shifted by the loop antenna. The solid red line indicates the frequency shift of the isolation peak. Blue solid line indicates the projection of the giant nonreciprocity at the side ZDC in the x-z plane. To emphasize it, we have plotted such an effectively broadband nonreciprocity (~ 200 MHz) in (c).

4.4 Summary

In this work, we experimentally demonstrate the enhancement of the nonreciprocal bandwidth of a cavity magnonics device by locally controlling the magnon's radiation. We find that the side ZDCs of our device are more sensitive to the magnon mode's damping rate. Accordingly, a loop antenna is placed close to the YIG sphere, which works as an additional dissipation channel for the magnon mode. By changing the separation between it and the YIG sphere, the radiation from the magnon mode to the loop antenna can be consecutively controlled, so that the side ZDCs of our devices can be shifted in a wide frequency range of a few hundred times of the magnon linewidth. By means of this property, an effective broadband giant nonreciprocity has been achieved, which is approximately 200 MHz. To date, nonreciprocal devices with high isolation rate and broad bandwidth are highly demanded in the thriving quantum technologies. Our work may further these efforts by providing a feasible method to achieve the broadband giant nonreciprocity, theoretically infinite, in a cavity magnonic device.

Chapter 5

Conclusion

In conclusion, this thesis has studied dissipative coupling in metamaterials and cavity magnon polaritons and their potential applications. From the theoretical studies results, we have demonstrated the difference between the coherent and dissipative coupling in eigenspace in frequency-domain and the oscillation in time-domain. From an experimental perspective, the level attraction due to dissipative coupling is achieved in both metamaterial structures and cavity magnon polaritons by constructing an open system. Furthermore, the level attraction due to dissipative coupling is ubiquitous in an open system embedded with two coupled resonance modes, and our experimental observations confirm it. The purpose of these theories and experiments was to develop practical methods to control the level attraction due to dissipative coupling. These studies' results could help make on-chip devices for various advanced metamaterials and cavity spintronic applications.

Chapter 2 started from the Lagrangian formalism with the simplified coupled pendulum model to describe the coherent and dissipative coupling mechanics. Using the equation of motion of harmonic oscillators coupled by a spring or a damper (dashpot), we established the theoretical model for the eigenvalues and eigenvectors and got an insight on the difference between the coherent and dissipative coupling. Moreover, we introduced finite element analysis as the numerical methods to analyze the field distribution in spatial to understand the field overlapping. An ordinary differential equation solver as another powerful numerical method provides the information in the time domain according to the equation of motion. The analytical and numerical results together provide the theoretical model to understand the dissipative coupling and why it differs from the coherent

coupling.

We demonstrated the level attraction in metamaterial structures in Chapter 3. A generalized RLC circuit model has been used to explain the electric, magnetic and dissipative coupling. The cancellation of these two different coupling mechanisms makes the dissipative coupling observable. Also, the asymmetric properties induced by interference between coherent and dissipative coupling has been discussed. The zero damping conditions in the system have been proven as singularities, and the complex analysis of transmission explained why dissipative coupling could reach this singular point and produce an effective negative damping rate. Level attraction dispersion and linewidth narrowing have been experimentally demonstrated by using a series of split-ring resonators. The zero-damping-condition can be controlled by both separation distance and voltage tunable split-ring resonator. This research provides a novel approach to design the high sensitivity sensing devices and switching devices.

An effective broadband nonreciprocal device has been demonstrated in Chapter 4. A quantum model with a non-Hermitian Hamiltonian was established to explain the nonreciprocal behaviors through magnons coupling with second quantized electromagnetic fields. Alternatively, in the classical picture, the interaction through field overlapping can be modeled by using a two-port RLC circuit. Generally speaking, the key properties of dissipative coupling can be concluded as the existence of traveling waves within the system which can be classified as open systems. In this work, we use a magnetic loop as an additional port to locally control the radiation of the magnon. The control of magnon damping allows us to continuously move the side zero-damping-condition and produce an effective broadband nonreciprocal device. This experiment offers an approach to design the practical isolator by using dissipative coupling which is potentially significant in quantum information technologies.

Overall, the theoretical and experimental works in this dissertation aim to provide a deeper understanding of dissipative coupling and explore potential applications specifically for designing novel microwave components and technologies. Future works in this field could explore the physical meaning of external coupling for microwave cavities, especially its influence on negative damping

and how it prevents the system from amplifying the input signal (transmission always smaller than unity) —exploring the topological properties such as exceptional points and singularities in such systems. Ultra-high quantity microwave resonators would be achievable by utilizing the dissipative coupling even on the planar structure, which is usually believed as low quality. Low-temperature experiments with few photons and spin numbers can also be performed to study the boundary between classical and quantum mechanics. The theoretical and experimental time-domain research may reveal the mystery of the zero and negative damping from another perspective and provide more evidence and understanding for potential applications. Furthermore, the powerful numerical methods would provide more information about CMP with dissipative coupling in the nonlinear and chaotic regime, which is maybe a fascinating world currently without any footprint. Generally speaking, the rapid expansion of the concept of dissipative coupling into different fields such as low temperatures, qubits, mechanical oscillators and nonlinear regimes would bring many surprising results and offers a promising future for dissipative coupling.

Appendix A

Mathematics of dissipatively coupled system

A.1 Transmission coefficient derivation for dissipatively coupled system

The effective second quantized Hamiltonian of the system we studied is defined as according to Ref.[36]:

$$\hat{H}_e/\hbar = \tilde{\omega}_c \hat{a}^\dagger \hat{a} + \tilde{\omega}_m \hat{b}^\dagger \hat{b} + (J + ie^{i\Theta_{1(2)}}\Gamma)(\hat{a}^\dagger \hat{b} + \hat{a} \hat{b}^\dagger), \quad (\text{A.1})$$

where the first two terms characterize the cavity and magnon mode independently and the third term is the coupling term included both coherent J and dissipative coupling Γ . The complex frequencies are given by $\tilde{\omega}_c = \omega_c - i\beta$ and $\tilde{\omega}_m = \omega_m - i(\alpha + \gamma_L)$ with both natural frequencies given by real part and intrinsic damping rates by imaginary part. The equation of motion for operator \hat{a} can be calculated using Heisenberg representation:

$$\frac{d\hat{a}}{dt} = \frac{i}{\hbar} [\hat{H}_e, \hat{a}] = -i\tilde{\omega}_c \hat{a} - i(J + ie^{i\Theta_{1(2)}}\Gamma)\hat{b}, \quad (\text{A.2})$$

where we have use the bosonic operator identity $[\hat{a}, \hat{b}] = [\hat{a}, \hat{a}] = [\hat{a}, \hat{b}^\dagger] = 0$ and $[\hat{a}, \hat{a}^\dagger] = 1$. Similarly, for operator \hat{b} of the magnon mode, we have:

$$\frac{d\hat{b}}{dt} = \frac{i}{\hbar} [\hat{H}_e, \hat{b}] = -i\tilde{\omega}_m \hat{b} - i(J + ie^{i\Theta_{1(2)}}\Gamma)\hat{a}. \quad (\text{A.3})$$

The equations of motion in matrix form can be write as:

$$\frac{d}{dt} \begin{bmatrix} \hat{a} \\ \hat{b} \end{bmatrix} = -i \begin{bmatrix} \tilde{\omega}_c & J + i\Gamma e^{i\Theta_{1(2)}} \\ J + i\Gamma e^{i\Theta_{1(2)}} & \tilde{\omega}_m \end{bmatrix} \begin{bmatrix} \hat{a} \\ \hat{b} \end{bmatrix}. \quad (\text{A.4})$$

Which is the Eqn.(4.2) in the main text. We can known the eigenvalues of the system as

$\tilde{\omega}_{\pm} = (\tilde{\omega}_c + \tilde{\omega}_m \pm \sqrt{(\tilde{\omega}_c - \tilde{\omega}_m)^2 + 4(J + i\Gamma e^{i\Theta_{1(2)}})^2})/2$ by solving the matrix in Eqn.A.4. Consider the microwave signal input from port 1 or port 2, by using quantum Langevin equations, we have:

$$\frac{d}{dt} \begin{bmatrix} \hat{a} \\ \hat{b} \end{bmatrix} = -i \begin{bmatrix} \tilde{\omega}_c - i\kappa & J + i\Gamma e^{i\Theta_{1(2)}} \\ J + i\Gamma e^{i\Theta_{1(2)}} & \tilde{\omega}_m \end{bmatrix} \begin{bmatrix} \hat{a} \\ \hat{b} \end{bmatrix} + \begin{bmatrix} \sqrt{\kappa} \\ \sqrt{\gamma} \end{bmatrix} \hat{p}_{1(2)}^{in}. \quad (\text{A.5})$$

Where $\hat{p}_{1(2)}^{in}$ is the driving field result from input microwave and the $i\kappa$ enters to cavity mode term as the external damping. In this case, the total damping of the magnon mode $\tilde{\omega}_m$ is given by $\alpha' = \alpha + \gamma_L + \gamma$, where the γ is the external damping of the magnon mode. Assuming that operator has the relation $\hat{a} = a \cdot e^{-i\omega t}$, $\hat{b} = b \cdot e^{-i\omega t}$ and $\hat{p}_{1(2)}^{in} = p_{1(2)}^{in} \cdot e^{-i\omega t}$, and the equations of motion are given by:

$$i(\tilde{\omega}_c - i\kappa - \omega)a + i(J + i\Gamma e^{i\Theta_{1(2)}})b = \sqrt{\kappa}p_{1(2)}^{in} \quad (\text{A.6})$$

$$i(\tilde{\omega}_m - \omega)b + i(J + i\Gamma e^{i\Theta_{1(2)}})a = \sqrt{\gamma}p_{1(2)}^{in}. \quad (\text{A.7})$$

From Eqn.A.7 we have the expression for operator \hat{b} as following:

$$b = \frac{\sqrt{\gamma}p_{1(2)}^{in} - i(J + i\Gamma e^{i\Theta_{1(2)}})a}{i(\tilde{\omega}_m - \omega)}, \quad (\text{A.8})$$

substitute into Eqn.A.6, we have:

$$\left[i(\tilde{\omega}_c - i\kappa - \omega) - \frac{(J + i\Gamma e^{i\Theta_{1(2)}})^2}{i(\tilde{\omega}_m - \omega)} \right] a - \underline{i(J + i\Gamma e^{i\Theta_{1(2)}})\sqrt{\gamma}p_{1(2)}^{in}} = \sqrt{\kappa}p_{1(2)}^{in}, \quad (\text{A.9})$$

where we have assumed that $\kappa \gg \gamma$ and also $|J + ie^{i\Theta_{1(2)}}\Gamma| \ll \sqrt{\kappa}$, the second term in Eqn. A.9 would vanish. Therefore, we have the amplitude solutions as:

$$\begin{aligned} a &= \frac{\sqrt{\kappa} \cdot p_{1(2)}^{in}}{i(\tilde{\omega}_c - i\kappa - \omega) + \frac{(J + i\Gamma e^{i\Theta_{1(2)}})^2}{i(\tilde{\omega}_m - \omega)}}, \\ b &= \frac{i(J + i\Gamma e^{i\Theta_{1(2)}})\sqrt{\kappa} \cdot p_{1(2)}^{in}}{-(\tilde{\omega}_c - i\kappa - \omega)(\tilde{\omega}_m - \omega) + (J + i\Gamma e^{i\Theta_{1(2)}})^2}. \end{aligned} \quad (\text{A.10})$$

By using the input-output relation $\hat{p}_{2(1)}^{out} = \hat{p}_{1(2)}^{in} - \sqrt{\kappa}\hat{a}$, we have the transmission coefficient as:

$$S_{21(12)} = \frac{\hat{p}_{2(1)}^{out}}{\hat{p}_{1(2)}^{in}} = 1 - \frac{\sqrt{\kappa}\hat{a}}{\hat{p}_{1(2)}^{in}} = 1 - \frac{\kappa}{i(\omega_c - \omega) + \kappa + \beta + \frac{(J + i\Gamma e^{i\Theta_{1(2)}})^2}{i(\omega_m - \omega) + \alpha'}}. \quad (\text{A.11})$$

A.2 Zero damping conditions (ZDCs) and its simplification

The complex eigenvalues of the coupled system can be written as following, with real part represents its resonance frequency and imaginary part represents the damping rate:

$$\tilde{\omega}_{\pm} = \left(2\omega_c - \Delta - i(\beta + \alpha') \pm \sqrt{(\Delta + i(\beta - \alpha'))^2 + 4(J + i\Gamma e^{i\Theta_{1(2)}})^2} \right) / 2. \quad (\text{A.12})$$

where detuning of magnon mode from cavity mode frequency is given by $\Delta = \omega_c - \omega_m$. The zero damping condition can be obtained by setting $\text{Im}(\tilde{\omega})_{\pm} = 0$. Therefore, we have:

$$2\omega_c - \Delta - i(\beta + \alpha') \pm \sqrt{(\Delta + i(\beta - \alpha'))^2 + 4(J + i\Gamma e^{i\Theta_{1(2)}})^2} = \mathcal{R}, \quad (\text{A.13})$$

where \mathcal{R} is a unknown real number that balance the equation. So we have:

$$2\omega_c - \Delta - i(\beta + \alpha') - \mathcal{R} = \pm \sqrt{(\Delta + i(\beta - \alpha'))^2 + 4(J + i\Gamma e^{i\Theta_{1(2)}})^2}. \quad (\text{A.14})$$

take the square of both side, and take $e^{i\Theta} = 1$ for simplicity:

$$\begin{aligned} (2\omega_c - \Delta)^2 - 2i(2\omega_c - \Delta)(\beta + \alpha') - (\beta + \alpha')^2 + \mathcal{R}^2 - 4\mathcal{R}\omega_c + 2\mathcal{R}\Delta + 2\mathcal{R}i(\beta + \alpha'), \\ = (\Delta^2 - 2i\Delta(\beta - \alpha') - (\beta - \alpha')^2 + 4J^2 + 8iJ\Gamma - 4\Gamma^2). \end{aligned} \quad (\text{A.15})$$

Separate the imaginary and real part of Eqn.A.15 into two different equations, we get:

$$-2i(2\omega - \Delta)(\beta + \alpha') + 2\mathcal{R}i(\beta + \alpha') = -2\Delta i(\beta - \alpha') + 8iJ\Gamma. \quad (\text{A.16})$$

The value of \mathcal{R} can be solved by using Eqn.A.16, we have:

$$\mathcal{R}^2 + \mathcal{R}(2\Delta - 4\omega_c) + 4\omega_c^2 - 4\omega_c\Delta - 4(J^2 - \Gamma^2) - 4\beta\alpha' = 0. \quad (\text{A.17})$$

The solution of \mathcal{R} is easy to obtain:

$$\mathcal{R} = 2\omega_c - \Delta \pm \sqrt{\Delta^2 + 4(J^2 + \Gamma^2) + 2\beta\alpha'}. \quad (\text{A.18})$$

Substitute the Eqn.A.18 into Eqn.A.16, we have:

$$\pm 2(\beta + \alpha')\sqrt{\Delta^2 + 4(J^2 + \Gamma^2) + 2\beta\alpha'} = -2\Delta(\beta - \alpha') + 8J\Gamma. \quad (\text{A.19})$$

Again, take the square on both side of Eqn.A.19 and rearrange, we have:

$$\alpha'\beta\Delta^2 + 2\Delta(\beta - \alpha')J\Gamma + (\alpha' + \beta)^2(J^2 - \Gamma^2 + \alpha'\beta) - 4J^2\Gamma^2 = 0. \quad (\text{A.20})$$

The solutions for Δ are given by:

$$\Delta^\pm = \frac{-(\beta - \alpha')J\Gamma \pm (\beta + \alpha')\sqrt{J^2\Gamma^2 - \alpha'\beta(J^2 - \Gamma^2 + \alpha'\beta)}}{\alpha'\beta}. \quad (\text{A.21})$$

These ZDC solutions are both valid for ω_- and ω_+ . If we take the Taylor expansion to the first order on the square root term of Eqn.A.21, we have:

$$\sqrt{J^2\Gamma^2 - \alpha'\beta(J^2 - \Gamma^2 + \alpha'\beta)} = J\Gamma \left(1 - \frac{\alpha'\beta(J^2 - \Gamma^2 + \alpha'\beta)}{2J^2\Gamma^2} \right). \quad (\text{A.22})$$

Therefore, the ZDC in Eqn.A.21 can be simplified to the first order as:

$$\begin{aligned} \Delta^\pm &= \frac{-(\beta - \alpha')J\Gamma \pm (\beta + \alpha')J\Gamma \left(1 - \frac{\alpha'\beta(J^2 - \Gamma^2 + \alpha'\beta)}{2J^2\Gamma^2} \right)}{\alpha'\beta}, \\ \Delta^+ &= \frac{2J\Gamma e^{i\Theta_{1(2)}}}{\beta} - \frac{(\alpha' + \beta)(J^2 - \Gamma^2 + \alpha'\beta)}{2J\Gamma e^{i\Theta_{1(2)}}}, \\ \Delta^- &= -\frac{2J\Gamma e^{i\Theta_{1(2)}}}{\alpha'} + \frac{(\alpha' + \beta)(J^2 - \Gamma^2 + \alpha'\beta)}{2J\Gamma e^{i\Theta_{1(2)}}}. \end{aligned} \quad (\text{A.23})$$

We have put the term $e^{i\Theta_{1(2)}}$ back for the terms with Γ . In previous work[36], the zeroth order of approximation has been made in the case of $|J| \approx |\Gamma|$. The first order approximation can be applied to more generalized cases such as $|\Gamma| > |J|$. The term Δ^+ is closer to the cavity mode frequency, therefore we named it as center ZDC (Δ_{ce}) while the term Δ^- is close to the magnon mode frequency and this is called side ZDC (Δ_{si}).

Appendix B

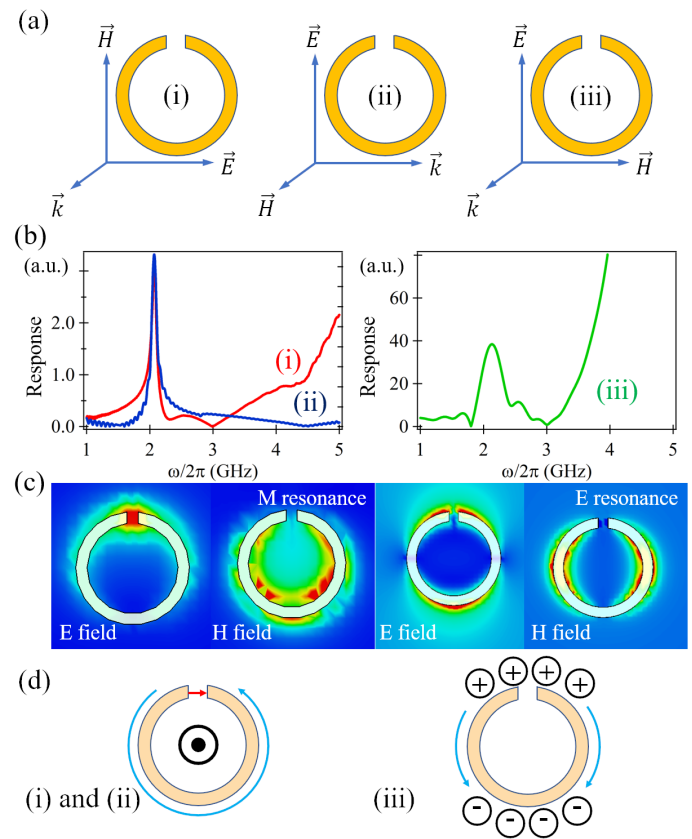
Numerical results on microwave resonators

With the development of printing circuit board technology, a design to convey and process the microwave-frequency signals known as microstrip line has been input forward in 1952 [131]. Microstrip lines, in principle, are equivalent to parallel-wire systems by using a conductor and a ground plane separated by a dielectric substrate. Compare to traditional microwave structures such as the waveguides and coaxial structures. The microstrip lines are lighter, cheaper, more compact and easier to fabricate. Nowadays, with the manufacturing capabilities have improved over time, other types of planar microwave transmission line have been designed such as coplanar waveguide and conductor-backed coplanar waveguide. Microstrip lines are perfect for the microwave circuit prototype design in the low power regime. As the design of the microstrip resonators, the characteristic impedance is critical which is firmly relates to the dielectric properties of the substrate and the structure. The characteristic impedance can be obtained either from the empirical formulas or finite element analysis.

B.1 Excitations of split-ring resonators

There are different ways to excite an SRR in both magnetic and electric resonance. In this section, we are about to explore the method of exciting an SRR with a plane wave. The simulation set up was shown in Fig.B.1 (a). In (i) we have the electric field of the plane wave parallel to the gap-bearing sides of SRR which directly act on the capacitor produced by the gap and this is known as electric

FIGURE B.1: (a) Three different way to excite a SRR with electric coupling (i) and magnetic coupling (ii) to magnetic resonance and electric coupling (iii) to electric resonance by different setup of plane wave. (b) The response of the SRR as a function of frequency of excitation signal. (c) Maximum electric and magnetic field distribution of the magnetic and electric resonance. (d) Analog of the magnetic resonance with a magnetic dipole and electric resonance with electric dipole. The light blue arrows represent the induced current and the black arrow penetrate the paper represent the magnetic field.



coupling; in (ii) we have magnetic field penetrate the surface of SRR which produce an oscillation magnetic flux through the split-ring; In (iii) the microwave electric field act perpendicular to the SRR gap and in-plane. Response of (i) and (ii) were given in Fig.B.1 (b)-left and both of these set up excites the magnetic resonance of SRR. Response of (iii) were given in Fig.B.1 (b)-right with a relative broader linewidth. The field distribution at resonance for (i) and (ii) are identical and shown in Fig.B.1 (c)-left, while that for (iii) are given in Fig.B.1 (c)-right. Not only the quality factor but also the field distribution characterized the difference between magnetic and electric resonance. Here we use a magnetic dipole (Fig.B.1 (d)-left) and electric dipole (Fig.B.1 (d)-right) to illustrate.

The electric and magnetic coupling can be explained by the overlapping of field [12], therefore, there is fundamental importance in understanding the refraction properties of SRPs in the low-frequency region of the EM spectrum. In the work in chapter 3, both electric and magnetic

coupling exist within the system and the interplay of both generates a fascinating world of dissipative coupling.

Bibliography

- ¹Ö. O. Soykal and M. Flatté, “Strong field interactions between a nanomagnet and a photonic cavity”, *Physical review letters* **104**, 077202 (2010).
- ²D. D. Awschalom, D. Loss, and N. Samarth, *Semiconductor spintronics and quantum computation* (Springer Science & Business Media, 2013).
- ³V. Cerletti, W. Coish, O. Gywat, and D. Loss, “Recipes for spin-based quantum computing”, *Nanotechnology* **16**, R27 (2005).
- ⁴I. Žutić, J. Fabian, and S. D. Sarma, “Spintronics: fundamentals and applications”, *Reviews of modern physics* **76**, 323 (2004).
- ⁵J. Linder and J. W. Robinson, “Superconducting spintronics”, *Nature Physics* **11**, 307–315 (2015).
- ⁶W. Han, R. K. Kawakami, M. Gmitra, and J. Fabian, “Graphene spintronics”, *Nature nanotechnology* **9**, 794 (2014).
- ⁷C.-M. Hu, “Dawn of cavity spintronics”, arXiv preprint arXiv:1508.01966 (2015).
- ⁸L. Bai, M. Harder, P. Hyde, Z. Zhang, C.-M. Hu, Y. Chen, and J. Q. Xiao, “Cavity mediated manipulation of distant spin currents using a cavity-magnon-polariton”, *Physical review letters* **118**, 217201 (2017).
- ⁹L. Bai, M Harder, Y. Chen, X Fan, J. Xiao, and C.-M. Hu, “Spin pumping in electrodynamically coupled magnon-photon systems”, *Physical Review Letters* **114**, 227201 (2015).
- ¹⁰H. Huebl, C. W. Zollitsch, J. Lotze, F. Hocke, M. Greifenstein, A. Marx, R. Gross, and S. T. Goennenwein, “High cooperativity in coupled microwave resonator ferrimagnetic insulator hybrids”, *Physical Review Letters* **111**, 127003 (2013).
- ¹¹Y. Tabuchi, S. Ishino, T. Ishikawa, R. Yamazaki, K. Usami, and Y. Nakamura, “Hybridizing ferromagnetic magnons and microwave photons in the quantum limit”, *Physical Review Letters* **113**, 083603 (2014).
- ¹²X. Zhang, C.-L. Zou, L. Jiang, and H. X. Tang, “Strongly coupled magnons and cavity microwave photons”, *Physical review letters* **113**, 156401 (2014).
- ¹³X. Zhang, C.-L. Zou, N. Zhu, F. Marquardt, L. Jiang, and H. X. Tang, “Magnon dark modes and gradient memory”, *Nature communications* **6**, 1–7 (2015).
- ¹⁴B. Yao, Y. Gui, J. Rao, S Kaur, X. Chen, W Lu, Y Xiao, H Guo, K.-P. Marzlin, and C.-M. Hu, “Cooperative polariton dynamics in feedback-coupled cavities”, *Nature communications* **8**, 1–6 (2017).
- ¹⁵A. Turukhin, V. Sudarshanam, M. Shahriar, J. Musser, B. Ham, and P. Hemmer, “Observation of ultraslow and stored light pulses in a solid”, *Physical Review Letters* **88**, 023602 (2001).

- ¹⁶D. Zhang, X.-Q. Luo, Y.-P. Wang, T.-F. Li, and J. You, “Observation of the exceptional point in cavity magnon-polaritons”, *Nature communications* **8**, 1–6 (2017).
- ¹⁷B. Yao, Y. Gui, M Worden, T Hegmann, M Xing, X. Chen, W Lu, Y Wroczynskyj, J van Lierop, and C.-M. Hu, “Quantifying the complex permittivity and permeability of magnetic nanoparticles”, *Applied Physics Letters* **106**, 142406 (2015).
- ¹⁸J. Rao, S Kaur, B. Yao, E. Edwards, Y. Zhao, X. Fan, D. Xue, T. Silva, Y. Gui, and C.-M. Hu, “Analogue of dynamic hall effect in cavity magnon polariton system and coherently controlled logic device”, *Nature communications* **10**, 1–7 (2019).
- ¹⁹X. Liu, L. P. Katehi, W. J. Chappell, and D. Peroulis, “High- q tunable microwave cavity resonators and filters using soi-based rf mems tuners”, *Journal of Microelectromechanical Systems* **19**, 774–784 (2010).
- ²⁰G. S. Agarwal, “Vacuum-field rabi oscillations of atoms in a cavity”, *JOSA B* **2**, 480–485 (1985).
- ²¹C.-M. Hu, B. Yao, S Kaur, Y. Gui, and W Lu, “Magnon polariton and pseudo-magnon-polariton”, in 2015 40th international conference on infrared, millimeter, and terahertz waves (irmmw-thz) (IEEE, 2015), pp. 1–3.
- ²²P. Gay-Balmaz and O. J. Martin, “Electromagnetic resonances in individual and coupled split-ring resonators”, *Journal of applied physics* **92**, 2929–2936 (2002).
- ²³N Katsarakis, T. Koschny, M Kafesaki, E. Economou, and C. Soukoulis, “Electric coupling to the magnetic resonance of split ring resonators”, *Applied physics letters* **84**, 2943–2945 (2004).
- ²⁴T.-J. Yen, W. Padilla, N. Fang, D. Vier, D. Smith, J. Pendry, D. Basov, and X. Zhang, “Terahertz magnetic response from artificial materials”, *Science* **303**, 1494–1496 (2004).
- ²⁵B. Yao, Y. Gui, X. Chen, W Lu, and C.-M. Hu, “Experimental realization of negative refraction using one metasurface”, *Applied Physics Letters* **106**, 121903 (2015).
- ²⁶S. Kaur, B. Yao, Y.-S. Gui, and C.-M. Hu, “On-chip artificial magnon-polariton device for voltage control of electromagnetically induced transparency”, *Journal of Physics D: Applied Physics* **49**, 475103 (2016).
- ²⁷N. Liu, H. Liu, S. Zhu, and H. Giessen, “Stereometamaterials”, *Nature Photonics* **3**, 157 (2009).
- ²⁸J. Perkins, A. Mascarenhas, Y. Zhang, J. Geisz, D. Friedman, J. Olson, and S. R. Kurtz, “Nitrogen-activated transitions, level repulsion, and band gap reduction in gaas 1- x n x with x < 0.03”, *Physical review letters* **82**, 3312 (1999).
- ²⁹N. Bernier, L. Tóth, A. Feofanov, and T. Kippenberg, “Level attraction in a microwave optomechanical circuit”, *Physical Review A* **98**, 023841 (2018).
- ³⁰M. Harder and C.-M. Hu, “Cavity spintronics: an early review of recent progress in the study of magnon-photon level repulsion”, in *Solid state physics*, Vol. 69 (Elsevier, 2018), pp. 47–121.
- ³¹B. Bhoi, B. Kim, S.-H. Jang, J. Kim, J. Yang, Y.-J. Cho, and S.-K. Kim, “Abnormal anticrossing effect in photon-magnon coupling”, *Physical Review B* **99**, 134426 (2019).
- ³²W. Yu, J. Wang, H. Yuan, J. Xiao, et al., “Prediction of attractive level crossing via a dissipative mode”, *Physical Review Letters* **123**, 227201 (2019).

- ³³Y Yang, J. Rao, Y. Gui, B. Yao, W Lu, and C.-M. Hu, “Control of the magnon-photon level attraction in a planar cavity”, *Physical Review Applied* **11**, 054023 (2019).
- ³⁴J. Rao, C. Yu, Y. Zhao, Y. Gui, X. Fan, D. Xue, and C. Hu, “Level attraction and level repulsion of magnon coupled with a cavity anti-resonance”, *New Journal of Physics* **21**, 065001 (2019).
- ³⁵P.-C. Xu, J. Rao, Y. Gui, X. Jin, and C.-M. Hu, “Cavity-mediated dissipative coupling of distant magnetic moments: theory and experiment”, *Physical Review B* **100**, 094415 (2019).
- ³⁶Y.-P. Wang, J. W. Rao, Y. Yang, P.-C. Xu, Y. S. Gui, B. M. Yao, J. Q. You, and C.-M. Hu, “Nonreciprocity and unidirectional invisibility in cavity magnonics”, *Phys. Rev. Lett.* **123**, 127202 (2019).
- ³⁷J. Zhao, Y. Liu, L. Wu, C.-K. Duan, Y.-x. Liu, and J. Du, “Observation of anti-p t-symmetry phase transition in the magnon-cavity-magnon coupled system”, *Physical Review Applied* **13**, 014053 (2020).
- ³⁸M.-A. Miri and A. Alù, “Exceptional points in optics and photonics”, *Science* **363**, 10 . 1126 / science.aar7709 (2019).
- ³⁹B. Yao, T. Yu, X. Zhang, W. Lu, Y. Gui, C.-M. Hu, and Y. M. Blanter, “Microscopic mechanism of level attraction from coherence-dissipation competition”, arXiv preprint arXiv:1906.12142 (2019).
- ⁴⁰J. Rao, Y. Wang, Y Yang, T Yu, Y. Gui, X. Fan, D. Xue, and C.-M. Hu, “Travelling photons mediated interactions between a magnon mode and a cavity photon mode”, arXiv preprint arXiv:1912.05478 (2019).
- ⁴¹J. Rao, S Kaur, X. Fan, D. Xue, B. Yao, Y. Gui, and C.-M. Hu, “Characterization of the non-resonant radiation damping in coupled cavity photon magnon system”, *Applied Physics Letters* **110**, 262404 (2017).
- ⁴²J. Strutt and L. Rayleigh, “Some general theorems relating to vibrations”, *Proceedings of the London Mathematical Society* **1**, 357–368 (1871).
- ⁴³I. I. Rabi, “Space quantization in a gyrating magnetic field”, *Physical Review* **51**, 652 (1937).
- ⁴⁴J. Zhou, P. Huang, Q. Zhang, Z. Wang, T. Tan, X. Xu, F. Shi, X. Rong, S Ashhab, and J. Du, “Observation of time-domain rabi oscillations in the landau-zener regime with a single electronic spin”, *Physical review letters* **112**, 010503 (2014).
- ⁴⁵A. Niskanen, K Harrabi, F Yoshihara, Y Nakamura, S Lloyd, and J. S. Tsai, “Quantum coherent tunable coupling of superconducting qubits”, *Science* **316**, 723–726 (2007).
- ⁴⁶A Amo, D Sanvitto, F. Laussy, D Ballarini, E Del Valle, M. Martin, A Lemaitre, J Bloch, D. Krizhanovskii, M. Skolnick, et al., “Collective fluid dynamics of a polariton condensate in a semiconductor microcavity”, *Nature* **457**, 291–295 (2009).
- ⁴⁷K. Tolpygo, “Physical properties of a rock salt lattice made up of deformable ions”, *Ukr. J. Phys* **53**, 93–102 (2008).
- ⁴⁸K. Huang, “On the interaction between the radiation field and ionic crystals”, *Proceedings of the Royal Society of London. Series A. Mathematical and Physical Sciences* **208**, 352–365 (1951).
- ⁴⁹K. C. Huang, P. Bienstman, J. D. Joannopoulos, K. A. Nelson, and S. Fan, “Phonon-polariton excitations in photonic crystals”, *Physical Review B* **68**, 075209 (2003).

- ⁵⁰H. Deng, H. Haug, and Y. Yamamoto, “Exciton-polariton bose-einstein condensation”, *Reviews of Modern Physics* **82**, 1489 (2010).
- ⁵¹P. Berini and I. De Leon, “Surface plasmon–polariton amplifiers and lasers”, *Nature Photonics* **6**, 16 (2012).
- ⁵²J.-M. Jin, *The finite element method in electromagnetics* (John Wiley & Sons, 2015).
- ⁵³J. Coggon, “Electromagnetic and electrical modeling by the finite element method”, *Geophysics* **36**, 132–155 (1971).
- ⁵⁴Y. Tabuchi, S. Ishino, A. Noguchi, T. Ishikawa, R. Yamazaki, K. Usami, and Y. Nakamura, “Coherent coupling between a ferromagnetic magnon and a superconducting qubit”, *Science* **349**, 405–408 (2015).
- ⁵⁵W. Kutta, “Beitrag zur nacherungsweisen integration totaler differentialgleichungen”, *Z. Math. Phys.* **46**, 435–453 (1901).
- ⁵⁶C. Runge, “Über die numerische auflösung von differentialgleichungen”, *Mathematische Annalen* **46**, 167–178 (1895).
- ⁵⁷J. Dormand and P. Prince, “Practical runge–kutta processes”, *SIAM Journal on Scientific and Statistical Computing* **10**, 977–989 (1989).
- ⁵⁸A. Iserles and S. Nørsett, “On the theory of parallel runge—kutta methods”, *IMA Journal of numerical Analysis* **10**, 463–488 (1990).
- ⁵⁹G. E. Forsythe, M. A. Malcolm, and C. B. Moler, *Computer methods for mathematical computations*, Vol. 259 (Prentice-Hall Englewood Cliffs, NJ, 1977).
- ⁶⁰J. R. Dormand and P. J. Prince, “A family of embedded runge-kutta formulae”, *Journal of computational and applied mathematics* **6**, 19–26 (1980).
- ⁶¹D. Storti and R. Rand, “Dynamics of two strongly coupled van der pol oscillators”, *International Journal of Non-Linear Mechanics* **17**, 143–152 (1982).
- ⁶²I. Kovacic and M. J. Brennan, *The duffing equation: nonlinear oscillators and their behaviour* (John Wiley & Sons, 2011).
- ⁶³M. Hénon and C. Heiles, “The applicability of the third integral of motion: some numerical experiments”, *The Astronomical Journal* **69**, 73 (1964).
- ⁶⁴C. Match, M. Harder, L. Bai, P. Hyde, and C.-M. Hu, “Transient response of the cavity magnon-polariton”, *Physical Review B* **99**, 134445 (2019).
- ⁶⁵J. J. Pla, K. Y. Tan, J. P. Dehollain, W. H. Lim, J. J. Morton, F. A. Zwanenburg, D. N. Jamieson, A. S. Dzurak, and A. Morello, “High-fidelity readout and control of a nuclear spin qubit in silicon”, *Nature* **496**, 334–338 (2013).
- ⁶⁶J. M. Martinis, S Nam, J Aumentado, and C Urbina, “Rabi oscillations in a large josephson-junction qubit”, *Physical review letters* **89**, 117901 (2002).
- ⁶⁷G. V. Eleftheriades and K. G. Balmain, *Negative-refraction metamaterials: fundamental principles and applications* (John Wiley & Sons, 2005).
- ⁶⁸T. J. Cui, D. R. Smith, and R. Liu, *Metamaterials* (Springer, 2010).

- ⁶⁹M. Lapine, I. V. Shadrivov, and Y. S. Kivshar, “Colloquium: nonlinear metamaterials”, *Reviews of Modern Physics* **86**, 1093 (2014).
- ⁷⁰Y Ra’Di, C. Simovski, and S. Tretyakov, “Thin perfect absorbers for electromagnetic waves: theory, design, and realizations”, *Physical Review Applied* **3**, 037001 (2015).
- ⁷¹V. Veselago, “Electrodynamics of substances with simultaneously negative electrical and magnetic permeabilities”, *Soviet Physics Uspekhi* **10**, 504–509 (1968).
- ⁷²R. A. Shelby, D. R. Smith, and S. Schultz, “Experimental verification of a negative index of refraction”, *science* **292**, 77–79 (2001).
- ⁷³D. Schurig, J. J. Mock, B. Justice, S. A. Cummer, J. B. Pendry, A. F. Starr, and D. R. Smith, “Metamaterial electromagnetic cloak at microwave frequencies”, *Science* **314**, 977–980 (2006).
- ⁷⁴N. Liu, L. Langguth, T. Weiss, J. Kästel, M. Fleischhauer, T. Pfau, and H. Giessen, “Plasmonic analogue of electromagnetically induced transparency at the drude damping limit”, *Nature materials* **8**, 758–762 (2009).
- ⁷⁵N. I. Landy, S. Sajuyigbe, J. J. Mock, D. R. Smith, and W. J. Padilla, “Perfect metamaterial absorber”, *Physical review letters* **100**, 207402 (2008).
- ⁷⁶Y. Sun, W. Tan, H.-q. Li, J. Li, and H. Chen, “Experimental demonstration of a coherent perfect absorber with pt phase transition”, *Physical review letters* **112**, 143903 (2014).
- ⁷⁷M. Baraclough, I. R. Hooper, and W. L. Barnes, “Investigation of the coupling between tunable split-ring resonators”, *Physical Review B* **98**, 085146 (2018).
- ⁷⁸M. B. Plenio and P. L. Knight, “The quantum-jump approach to dissipative dynamics in quantum optics”, *Reviews of Modern Physics* **70**, 101 (1998).
- ⁷⁹W. Suh, Z. Wang, and S. Fan, “Temporal coupled-mode theory and the presence of non-orthogonal modes in lossless multimode cavities”, *IEEE Journal of Quantum Electronics* **40**, 1511–1518 (2004).
- ⁸⁰A. Metelmann and A. A. Clerk, “Nonreciprocal photon transmission and amplification via reservoir engineering”, *Phys. Rev. X* **5**, 021025 (2015).
- ⁸¹M. Harder, Y. Yang, B. M. Yao, C. H. Yu, J. W. Rao, Y. S. Gui, R. L. Stamps, and C.-M. Hu, “Level attraction due to dissipative magnon-photon coupling”, *Phys. Rev. Lett.* **121**, 137203 (2018).
- ⁸²F. Verstraete, M. M. Wolf, and J. I. Cirac, “Quantum computation and quantum-state engineering driven by dissipation”, *Nature physics* **5**, 633–636 (2009).
- ⁸³L. Verslegers, Z. Yu, Z. Ruan, P. B. Catrysse, and S. Fan, “From electromagnetically induced transparency to superscattering with a single structure: a coupled-mode theory for doubly resonant structures”, *Physical review letters* **108**, 083902 (2012).
- ⁸⁴C. Qian, X. Lin, Y. Yang, X. Xiong, H. Wang, E. Li, I. Kaminer, B. Zhang, and H. Chen, “Experimental observation of superscattering”, *Physical review letters* **122**, 063901 (2019).
- ⁸⁵P. Peng, W. Cao, C. Shen, W. Qu, J. Wen, L. Jiang, and Y. Xiao, “Anti-parity-time symmetry with flying atoms”, *Nature Physics* **12**, 1139–1145 (2016).

- ⁸⁶K. Yamamoto, M. Nakagawa, K. Adachi, K. Takasan, M. Ueda, and N. Kawakami, “Theory of non-hermitian fermionic superfluidity with a complex-valued interaction”, *Physical review letters* **123**, 123601 (2019).
- ⁸⁷R. N. Simons, *Coplanar waveguide circuits, components, and systems*, Vol. 165 (John Wiley & Sons, 2004).
- ⁸⁸J.-S. Hong, “Couplings of asynchronously tuned coupled microwave resonators”, *IEE Proceedings-Microwaves, Antennas and Propagation* **147**, 354–358 (2000).
- ⁸⁹R. W. Erickson and D. Maksimovic, *Fundamentals of power electronics* (Springer Science & Business Media, 2007).
- ⁹⁰W. G. Hurley and D. J. Wilcox, “Calculation of leakage inductance in transformer windings”, *IEEE Transactions on Power Electronics* **9**, 121–126 (1994).
- ⁹¹A. B. Pippard, *The physics of vibration* (Cambridge University Press, 2007).
- ⁹²S. Wang, F. C. Lee, and J. D. Van Wyk, “Inductor winding capacitance cancellation using mutual capacitance concept for noise reduction application”, *IEEE transactions on electromagnetic compatibility* **48**, 311–318 (2006).
- ⁹³F. Capolino, *Theory and phenomena of metamaterials* (CRC press, 2009).
- ⁹⁴K. Fang, J. Luo, A. Metelmann, M. H. Matheny, F. Marquardt, A. A. Clerk, and O. Painter, “Generalized non-reciprocity in an optomechanical circuit via synthetic magnetism and reservoir engineering”, *Nature Physics* **13**, 465–471 (2017).
- ⁹⁵D. M. Pozar, *Microwave engineering* (John Wiley & Sons, 2009).
- ⁹⁶M. F. Limonov, M. V. Rybin, A. N. Poddubny, and Y. S. Kivshar, “Fano resonances in photonics”, *Nature Photonics* **11**, 543–554 (2017).
- ⁹⁷X. Zhang, A. Galda, X. Han, D. Jin, and V. M. Vinokur, “Broadband nonreciprocity enabled by strong coupling of magnons and microwave photons”, *Phys. Rev. Applied* **13**, 044039 (2020).
- ⁹⁸B. Luk'yanchuk, N. I. Zheludev, S. A. Maier, N. J. Halas, P. Nordlander, H. Giessen, and C. T. Chong, “The fano resonance in plasmonic nanostructures and metamaterials”, *Nature materials* **9**, 707–715 (2010).
- ⁹⁹A. Khanna and Y Garault, “Determination of loaded, unloaded, and external quality factors of a dielectric resonator coupled to a microstrip line”, *IEEE Transactions on Microwave Theory and Techniques* **31**, 261–264 (1983).
- ¹⁰⁰E. R. Edwards, A. B. Kos, M. Weiler, and T. J. Silva, “A microwave interferometer of the michelson-type to improve the dynamic range of broadband ferromagnetic resonance measurements”, *IEEE Magnetics Letters* **8**, 1–4 (2016).
- ¹⁰¹M. H. Devoret and R. J. Schoelkopf, “Superconducting circuits for quantum information: an outlook”, *Science* **339**, 1169–1174 (2013).
- ¹⁰²P. Lodahl, S. Mahmoodian, S. Stobbe, A. Rauschenbeutel, P. Schneeweiss, J. Volz, H. Pichler, and P. Zoller, “Chiral quantum optics”, *Nature* **541**, 473–480 (2017).
- ¹⁰³J Gorman, D. Hasko, and D. Williams, “Charge-qubit operation of an isolated double quantum dot”, *Physical review letters* **95**, 090502 (2005).

- ¹⁰⁴G. M. Palma, K.-A. Suominen, and A. Ekert, “Quantum computers and dissipation”, Proceedings of the Royal Society of London. Series A: Mathematical, Physical and Engineering Sciences **452**, 567–584 (1996).
- ¹⁰⁵Z. Zhou, S.-I. Chu, and S. Han, “Quantum computing with superconducting devices: a three-level squid qubit”, Physical Review B **66**, 054527 (2002).
- ¹⁰⁶M. A. Nielsen and I. Chuang, *Quantum computation and quantum information*, 2002.
- ¹⁰⁷D. Lachance-Quirion, Y. Tabuchi, S. Ishino, A. Noguchi, T. Ishikawa, R. Yamazaki, and Y. Nakamura, “Resolving quanta of collective spin excitations in a millimeter-sized ferromagnet”, Science advances **3**, e1603150 (2017).
- ¹⁰⁸C. Caloz, A. Alù, S. Tretyakov, D. Sounas, K. Achouri, and Z.-L. Deck-Léger, “Electromagnetic nonreciprocity”, Physical Review Applied **10**, 047001 (2018).
- ¹⁰⁹C. L. Hogan, “The ferromagnetic faraday effect at microwave frequencies and its applications”, Rev. Mod. Phys. **25**, 253–262 (1953).
- ¹¹⁰A. Metelmann and A. A. Clerk, “Nonreciprocal quantum interactions and devices via autonomous feedforward”, Phys. Rev. A **95**, 013837 (2017).
- ¹¹¹Z. Shen, Y.-L. Zhang, Y. Chen, C.-L. Zou, Y.-F. Xiao, X.-B. Zou, F.-W. Sun, G.-C. Guo, and C.-H. Dong, “Experimental realization of optomechanically induced non-reciprocity”, Nature Photonics **10**, 657–661 (2016).
- ¹¹²F. Ruesink, M.-A. Miri, A. Alu, and E. Verhagen, “Nonreciprocity and magnetic-free isolation based on optomechanical interactions”, Nature communications **7**, 1–8 (2016).
- ¹¹³A. Kamal, J. Clarke, and M. Devoret, “Noiseless non-reciprocity in a parametric active device”, Nature Physics **7**, 311–315 (2011).
- ¹¹⁴X. Zhang, A. Galda, X. Han, D. Jin, and V. Vinokur, “Strong coupling-enabled broadband non-reciprocity”, arXiv preprint arXiv:1910.14117 (2019).
- ¹¹⁵G. Flower, J. Bourhill, M. Goryachev, and M. E. Tobar, “Broadening frequency range of a ferromagnetic axion haloscope with strongly coupled cavity–magnon polaritons”, Physics of the Dark Universe **25**, 100306 (2019).
- ¹¹⁶Y. Cao, P. Yan, H. Huebl, S. T. B. Goennenwein, and G. E. W. Bauer, “Exchange magnon-polaritons in microwave cavities”, Phys. Rev. B **91**, 094423 (2015).
- ¹¹⁷B. Z. Rameshti, Y. Cao, and G. E. Bauer, “Magnetic spheres in microwave cavities”, Physical Review B **91**, 214430 (2015).
- ¹¹⁸X. Zhang, C.-L. Zou, L. Jiang, and H. X. Tang, “Cavity magnomechanics”, Science advances **2**, e1501286 (2016).
- ¹¹⁹Y.-P. Wang, G.-Q. Zhang, D. Zhang, T.-F. Li, C.-M. Hu, and J. You, “Bistability of cavity magnon polaritons”, Physical review letters **120**, 057202 (2018).
- ¹²⁰J. Li, S.-Y. Zhu, and G. Agarwal, “Magnon-photon-phonon entanglement in cavity magnomechanics”, Physical review letters **121**, 203601 (2018).
- ¹²¹D. Lachance-Quirion, Y. Tabuchi, A. Gloppe, K. Usami, and Y. Nakamura, “Hybrid quantum systems based on magnonics”, Applied Physics Express **12**, 070101 (2019).

- ¹²²M. Goryachev, W. G. Farr, D. L. Creedon, Y. Fan, M. Kostylev, and M. E. Tobar, “High-cooperativity cavity qed with magnons at microwave frequencies”, *Physical Review Applied* **2**, 054002 (2014).
- ¹²³N. Kostylev, M. Goryachev, and M. E. Tobar, “Superstrong coupling of a microwave cavity to yttrium iron garnet magnons”, *Applied Physics Letters* **108**, 062402 (2016).
- ¹²⁴J. Bourhill, N. Kostylev, M. Goryachev, D. Creedon, and M. Tobar, “Ultrahigh cooperativity interactions between magnons and resonant photons in a yig sphere”, *Physical Review B* **93**, 144420 (2016).
- ¹²⁵N. Lambert, J. Haigh, S Langenfeld, A. Doherty, and A. Ferguson, “Cavity-mediated coherent coupling of magnetic moments”, *Physical Review A* **93**, 021803 (2016).
- ¹²⁶I. Boventer, M. Kläui, R. Macêdo, and M. Weides, “Steering between level repulsion and attraction: broad tunability of two-port driven cavity magnon-polaritons”, *New Journal of Physics* **21**, 125001 (2019).
- ¹²⁷I. Proskurin, R. Macêdo, and R. L. Stamps, “Microscopic origin of level attraction for a coupled magnon-photon system in a microwave cavity”, *New Journal of Physics* **21**, 095003 (2019).
- ¹²⁸V. L. Grigoryan, K. Shen, and K. Xia, “Synchronized spin-photon coupling in a microwave cavity”, *Physical Review B* **98**, 024406 (2018).
- ¹²⁹G. W. Ford, J. T. Lewis, and R. O’connell, “Quantum langevin equation”, *Physical Review A* **37**, 4419 (1988).
- ¹³⁰R. C. Dorf, *The electrical engineering handbook-six volume set* (CRC press, 2018).
- ¹³¹D. D. Grieg and H. F. Engelmann, “Microstrip-a new transmission technique for the klilomega-cycle range”, *Proceedings of the IRE* **40**, 1644–1650 (1952).